
THE UNIVERSITY *of* EDINBURGH

# Computational Study of Radiation Damage and Impurity Effects in Iron Based Alloys


*Graham Galloway*

A thesis submitted in fulfilment of the requirements
for the degree of Doctor of Philosophy
to the
University of Edinburgh

October 25, 2014

# Abstract

Molecular dynamics techniques are used to explore metals at an atomic level. The focus of the studies is the effects of irradiation on a metallic system. Ion surface bombardment effects, bulk cascades and interaction with voids and bubbles in bulk are studied.

In the first section a study of a copper $\langle 110 \rangle$ surface being bombarded by low energy argon ions is conducted. Molecular dynamics simulations were used to study the surface impact crater formation and the damage caused in the surrounding area. Another group had previously performed experimental measurements on the same system. The simulation data is compared to experiment, in order to validate the molecular dynamics technique. Additionally, information about the formation of the craters at time scales inaccessible to experiment can be gained.

In the next section bulk radiation induced cascades in BCC iron are considered. Cascades of energy 1 keV, 2 keV, and 5 keV are initiated in the bulk of the material and the damage yields studied. Cascades are also studied in proximity to voids and helium bubbles in the bulk. The damage formation processes and damage yields in these cascades is analysed. A mechanism that allowed voids to be ballistically moved by the cascade was observed. To further explore this an object kinetic Monte Carlo model was written to simulate the effects of this motion on the diffusion of the voids.

The final section is a study of transition metals as alloying elements in BCC iron. This system is of interest as it would be a model for various steels used in construction and shielding. A set of potentials describing iron with low concentrations of transition metals has previously been developed by a different

group. These potentials were implemented in the molecular dynamics code. The equilibrium properties of various alloys are explored by implementing a Metropolis algorithm to minimise the Gibbs free energy of the system. Various binary and tertiary alloys are analysed and compared with experimental values in the literature. The attraction of the elements to voids present in the system is also studied.

# Declaration

Except where otherwise stated, the research undertaken in this thesis was the unaided work of the author. Where the work was done in collaboration with others, a significant contribution was made by the author.

*G. Galloway*

October 25, 2014

# Acknowledgements

I would like to acknowledge valuable contributions from my supervisor Prof. G. J. Ackland, as well as useful discussions with my co-workers. I would also like to acknowledge EPSRC and the CM-DTC for funding and support.

# Contents

# Chapter 1

# Introduction

This thesis discusses some of the effects of radiation damage on metals. Metals used as shielding for fusion reactors undergo 14 MeV neutron bombardment at high temperature. The flux of radiation can affect the material properties by causing swelling and hardening[1]. These effects are linked to nano-scale changes in the irradiated material, which are due to the atomic displacement cascades that neutron bombardment induces. When close to the surface, cascades can form craters and surface diffusing defects. In the bulk, point defects such as interstitials and vacancies are formed.

These defects can undergo complicated interactions over time such as clustering behaviour, attraction to defect sinks or coupling to certain atomic types in the metal. Radiation induced swelling arises from void formation in the material[2]: vacancies cluster together forming voids while the excess interstitials diffuse to surfaces. Radiation bombardment can also cause transmutation of elements producing helium in the lattice[3, 4]. For materials near to fusion sources implantation of helium is also an issue[5]. The helium diffuses rapidly to grain boundaries[6] or interacts with the voids forming bubbles[7], which can have effects on the materials properties. Pinning interactions of the voids[8] and bubbles[9] with dislocations in the material leads to hardening.

The fluxes of defects can also be involved in radiation induced segregation[10, 11]. There are fluxes of defects towards absorbing sinks in the system. If a defect has an affinity for a certain type of atom it can induce concentration changes in the

alloy by dragging the atoms with them, leading to segregation of alloying elements to defect sinks[12]. The changes in local concentration of the alloy can affect its properties and induce precipitation behaviour. These precipitates have pinning effects on dislocations[13], hardening the material.

To explore such phenomena at a nano-scale, computational models can be used. To fully model the material, the atomic nuclei along with all of their electrons and interactions between them must be modelled in a fully quantum mechanical way. Density functional theory (DFT) attempts to model the electron density using a set of wave-functions. This method has been successfully used to model several aspects of radiation damage[14], although the technique is too expensive to consider larger scale phenomena, or long term dynamics.

In light of this, several approximations are developed that aim to capture the essential physics while reducing the computational cost. In molecular dynamics (MD) simulations only the atomic nuclei are directly simulated. The effects of the electrons are approximated through the use of empirical potentials. These models attempt to account for the coulomb effects and band energies of the electrons in metallic substances, using a functional form fitted to experimental or DFT data[15, 16]. Other potentials include properties such as magnetism[17], which can be significant for certain alloys. MD allows greater number of atoms and simulations lengths than DFT, allowing phenomena to be explored that are not accessible to DFT and sometimes not accessible to experiment.

MD is still computationally expensive. While it gives a detailed atomic view of the phenomena, larger length and time scales are often required for comparison to experiments, or predictions about the lifetime of a material. Various coarse-graining methods exist, that can allow some non-critical information to be lost, while retaining the important physics for the relevant length and time scales involved. Once such type of model is kinetic Monte Carlo (KMC). It can be implemented in such a way as to ignore on lattice atoms and their vibrations, leaving only the defects to evolve. The effects of the lattice vibrations is included probabilistically, in the transition rates of the defects from one state to another. This allows greatly increased length and time scales to be explored.

This thesis explores some of the effects of radiation damage using MD and KMC techniques. Surface damage and the subsequent diffusion of the defects produced

is studied using MD. The interaction of radiation cascades with voids and bubbles is also explored. The evolution of the damage formed and interaction processes, for both the surface and bulk damage, is explored using Monte Carlo methods. The properties of mixed alloys are considered, as well as their segregation properties in the presence of voids, and the effects of radiation cascades on their composition.

## 1.1 Structure of Thesis

Chapter 2 gives details of a varient of the verlet algorithm that was developed. The method allows two diffrent time steps to be used in the system, which is of particular use when the kinetic energy of the system is not evenly distributed in the simulation cell.

Chapter 3 studies surface bombardment of copper with argon ions. The results are compared directly to data from another groups experiment in order to validate the simulations.

Chapter 4 describes the interactions of voids and bubbles in iron with radiation induced cascades. These are explored through both molecular dynamics (MD) and object kinetic Monte Carlo (OKMC) simulations.

Chapter 5 explores the properties of a potential set for iron-based transition-metal alloys. The properties of some binary alloys under irradiation simulations are studied. The effects of slowly varying the composition of tertiary alloys is also analysed.

Finally, chapter 6 summarises the conclusions of the thesis.

# Chapter 2

# Spatially Varying Time Step

## 2.1 Verlet Algorithm

The Verlet algorithm is a widely used dynamics integrator in molecular dynamics (MD) simulations. The algorithm updates each particle in the system discretising the motion into temporal steps of size $\Delta t$. The positions are updated assuming that there is a constant acceleration over the time step:

$$\vec{x}(t + \Delta t) = \vec{x}(t) + \vec{v}(t)\Delta t + \frac{1}{2}\vec{a}(t)\Delta t^2$$

The change in velocity is taken as the average of the acceleration during the time step:

$$\vec{v}(t + \Delta t) = \vec{v}(t) + \frac{\vec{a}(t) + \vec{a}(t + \Delta t)}{2}\Delta t$$

From these equations the basic velocity Verlet algorithm can be stated as:

1) $\vec{v}(t + \frac{1}{2}\Delta t) = \vec{v}(t) + \frac{1}{2}\vec{a}(t)\Delta t$

2) $\vec{x}(t + \Delta t) = \vec{x}(t) + \vec{v}(t + \frac{1}{2}\Delta t)\Delta t$

3) Calculate $\vec{a}(t + \Delta t)$ using $\vec{x}(t + \Delta t)$

$$4)\ \vec{v}(t+\Delta t) = \vec{v}(t+\tfrac{1}{2}\Delta t) + \tfrac{1}{2}\vec{a}(t+\Delta t)\Delta t$$

The Verlet algorithm is time reversible, which leads to the cancellation of all odd powers of error for the integration. This makes the local error in the Verlet algorithm one order of magnitude higher than may be expected. An expression for the position based on two previous positions can be derived by taking the Taylor expansions of x around t, for two points equidistant in time from point t:

$$\vec{x}(t+\Delta t) = \vec{x}(t) + \vec{v}(t)\Delta t + \frac{\vec{a}(t)\Delta t^2}{2} + \frac{\vec{a}'(t)\Delta t^3}{6} + \mathcal{O}(4)$$

$$\vec{x}(t-\Delta t) = \vec{x}(t) - \vec{v}(t)\Delta t + \frac{\vec{a}(t)\Delta t^2}{2} - \frac{\vec{a}'(t)\Delta t^3}{6} + \mathcal{O}(4)$$

Summing these terms gives an expression for the position at $t+\Delta t$ that is fourth order in error:

$$\vec{x}(t+\Delta t) = 2\vec{x}(t) - \vec{x}(t-\Delta t) + 2\vec{a}(t)\Delta t^2 + \mathcal{O}(4)$$

This shows that including linear changes in acceleration in the position update equation would not improve the algorithm, meaning the position update is locally fourth order in error.

## 2.2 Varying Time Step

The time step used for the Verlet algorithm is an important quantity for tuning the efficiency of the simulation. Too large a step gives inaccuracies in the trajectories and violates energy conservation, too small a step leads to unnecessary calculations. During cascades the velocities of particles are initially very high until the cascades' energy dissipates. This means that the optimal time step at the start of the simulation is very different from that at the end of the simulation.

The criteria for accuracy during simulation is that the curvature of the accel-

eration over a time step is negligible, that is $\frac{d^4x}{dt^4}$ is small. This is because the algorithm explicitly accounts for acceleration, and linear changes in acceleration are eliminated due to the time reversibility of the algorithm. Strictly, this criteria could be achieved by calculating the gradient for every particle at every iteration of the integrator. The maximum gradient found would then be used to define a maximum distance that could safely be moved along that trajectory. From this distance and the particles velocity a time step could then be calculated.

However, such a procedure would be computationally expensive to implement. Instead, a simpler approach can be taken by picking a distance that will satisfy the maximum curvature of acceleration and using it in all situations. This circumvents the need to calculate gradients for all particles. For a given particle a time can be calculated from the particle's velocity and the maximum allowed distance.

Since consecutive checks of the allowed time step will yield similar answers, it is only necessary to perform this procedure every few hundred steps, which further reduces the computational overhead. If only the velocity is taken into account, the fastest particles in the system tend to have widely fluctuating velocities, as elastic collisions convert kinetic energy to potential energy and back. To smooth this effect, and so damp fluctuations in the time step, the particle's energy was studied instead of its velocity. The energy was taken as the kinetic energy plus any potential energy above the average, $E = KE + PE - \langle PE \rangle$

By assuming that all the energy is kinetic a maximum velocity can be calculated:

$$v = \sqrt{2E/m}$$

Where $E$ is the energy, including potential energy, and $m$ is the mass of the particle that has this energy. Computing this for all particles will yield the maximum velocity in the system. The velocity is converted to a time by picking a maximum distance that may be moved per iteration. In this case one thousandth of the atomic cell was used:

$$t = \frac{a_0}{1000}\sqrt{\frac{m}{2E}} \tag{2.1}$$

This value of t is the proposed time step. During simulations the time step is calculated every 100 steps and updated with the following rules: that it is not less than the current time step, and that it is no more than 10% greater. If it is greater than 10% the time step is increased by 10% only. These rules reduce fluctuations in the time step and allow it to smoothly go towards the system's equilibrium value. This process is repeated until the time step reaches the equilibrium value for the system, which is typically set at 1 fs, after which the standard Verlet algorithm is used.

## 2.3 Spatially Varying Time Step

During cascades the energy starts off localised around the primary knock-on atom (pka) and then spreads through the lattice. With the varying time step method, the motion of all atoms is integrated using the small time step needed for the fastest atoms. This is clearly inefficient as the atoms far from the cascade could be integrated at a much larger time step.

This inefficiency can be removed with an algorithm that allows different time steps in different regions of the system. One problem introduced by such an algorithm is dealing with the interactions at and across the boundary between time regions. The other issue is extrapolating the positions in the longer time step region, so that these atoms can still be moved on the shorter time step cycles. An algorithm that addresses these issues is explained below.

The algorithm splits the system into two parts. One which contains the high energy atoms, and another low energy region. The algorithm allows only two regions in its current form, although it could be extended to allow more. The regions will be referred to as the "hot" and "cold" regions, where the hot region encompasses the cascade. The time steps associated with the regions will be referred to as the hot time step, $t_H$, and the cold time step, $t_C$. Between these regions is a buffer region that accounts for the force interactions that cross regions. As the cascade progresses, spreading its energy through the system, the hot region

is adapted to contain the cascade.

The time step of the system is set to that of the hot region, and a full force calculation always occurs for the hot region. A full force calculation is only performed in the cold region every $R = t_H/t_C$ steps. In between these full updates, the forces acting on the atoms are extrapolated from past data, requiring the cold regions time step to be an integer multiple of the hot time step.

## 2.4 Detecting Energetic Regions

The method used to detect and adapt the hot energetic region of the system is detailed below. The total energy for each atom is calculated (potential + kinetic energy). If the energy is above a certain threshold it is considered to be in the hot region. The threshold energy is set based on the value of the cold time step. Due to the nature of the algorithm the cold time step can not be arbitrarily larger than the hot time step. In practise the maximum ratio between them is limited to about 22:1 (explained later in ch. 2.7).

This gives a natural way to pick the energy thresholding: a hot time step is chosen to satisfy the most energetic atoms in the system. The cold time step is calculated by multiplying the hot time step by the ratio of the time steps, $t_H R$. For a given cold time step the highest energy atoms that can be accommodated in this region can be found be rearranging eq. 2.1. The equation can be solved for $E_C$, the cold energy threshold using $m_m$, the minimum mass in the system:

$$E_C = \frac{m_m}{2}\left(\frac{a_0}{1000 t_C}\right)^2$$

The assignment of regions is only done every 500 to 1000 cycles. Due to this, atoms near to a hot atom are also considered to be in the hot region. This prevents an energetic atom from moving, or passing substantial energy, out of the region. Since the variable time step algorithm ensures that an atom will not move much more than one lattice spacing in this time, a threshold distance of 7 angstroms was sufficient to account for the motion and ranged interaction of the hot atoms.

## 2.5 Cross-Region Buffering

After the hot region has been detected a buffer region is placed surrounding it. Any atom in the cold region, that is within interaction distance of an atom in the hot region, is included in a buffer region. The interaction distance is a property of the exact potential used. For screened metallic potentials this distance is typically only two or three times the lattice parameters.

To calculate forces in the the buffer region, some extrapolated forces are used as well as some current force data. All interactions between a hot atom and buffer atoms are calculated every cycle. Interactions between buffer atoms or between buffer atoms and cold atoms are only calculated every $t_C$; extrapolated forces are used in-between updates. This accounts for the motion of atoms in the hot region changing the forces in the buffer region. Since hot atoms feel all atoms around themselves the buffer atoms must be receptive to force from hot atoms to conserve Newton's third law.

It does not account for the secondary effects of these changes altering the forces between buffer atoms. This effect is expected to be small as the boundary of the hot region is placed so that there is already a buffer of nearly cold atoms at the edge of the hot region. The double buffering of padding the hot region, as well as maintaining a buffer region, is necessary for the stability of the algorithm. It is not overly computationally expensive, as forces internal to the outer buffer are not calculated every time step.

## 2.6 Force Extrapolation Method

The algorithm requires that every particle in the system moves on every update cycle. If atoms were only moved on their full update cycles (i.e. every $t_H$ and $t_C$ respectively) violations of Newton's third law, and energy conservation, would arise near to boundaries. Since the correct forces are only known every $t_C$ in the cold region, but required every $t_H$, they must be extrapolated from past data.

Various extrapolation methods were considered. Linear extrapolation from two

previous data points was found to be insufficient. A method of parabolic fits using three previous points was adopted. Using the most recent points ($t - t_H, t - 2t_H, t - 3t_H$) did not sufficiently conserve the trajectories of the particles. This is because the previous points may all be estimated points for ratios of time steps larger than 3. The parabolic method develops a growing instability in such cases as the next estimate increases the error made in the previous step.

For stability it was required that at least two full calculation points were used. Letting $R = t_C/t_H$ be the ratio of time steps in the system and n = (1,R-1) be the step number between full updates on the $R^{th}$ cycles. On the $n^{th}$ step the points $t - nt_H, t - t_C - nt_H$ and $t - t_C - 2nt_H$ are used for the estimate, as shown in fig. 2.1. Explicitly, these are the last two full updates of the cold region as well as the extrapolated point that is n steps before the first full update. The same two $t_C$ reference points are used for R steps, along with an estimated point that moves backwards in time by $t_H$ every time the current point to be estimated moves forward by $t_H$. After R cycles of this a full update of the cold region is performed, giving a new data point for future extrapolations.

Such an extrapolation is symmetric in terms of the time spacing of the points and the type of points used. The time reversibility of the extrapolation turned out to be an important criteria for stability as it should obey the symmetries of the Verlet algorithm.

Solving for a parabolic fit to three points with the temporal separation given above (using method of simultaneous equations), it can be shown that the force at time t, which is n steps after the last full update, is given by:

$$F(t) = c_1 F(t - nt_H) + c_2 F(t - nt_H - t_C) + c_3 F(t - 2nt_H - t_c) \tag{2.2}$$

$$c_1 = a(r + 1)$$

$$c_2 = -c_1$$

$$c_3 = (r + 1)(ar - 1)$$

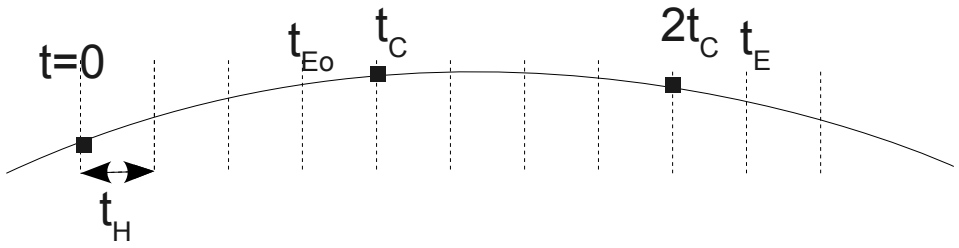


*Figure 2.1*: *Diagram of the force estimation procedure used in the spatially varying Verlet algorithm. The curved line is the correct force. Dots represent correct measurements of the force every $t_C$. The vertical lines represent points that must be extrapolated and are $t_H$ apart, with $R = t_C/t_H = 4$. The force at time $t_E$ is estimated using points $2t_C$, $t_C$ and the estimated point $t_{Eo}$.*

$$r = \frac{R}{n} \qquad a = \frac{(r+2)}{(r^2+r)}$$

$$R = \frac{t_C}{t_H} \qquad n \in \mathbb{Z}, \quad 1 \leq n < R$$

## 2.7 Efficiency of Algorithm

A limiting factor in the efficiency of the algorithm is that the parabolic extrapolation requires several cycles to be run fully at $t_H$ to gain data to extrapolate from. In its current form this requires $2Rt_H$ full force calculation time steps to be run before a reliable extrapolation can begin. This is enough data to get two points $t_C$ apart as well as several points before the first $t_C$ point to extrapolate symmetrically from. During normal operation a full calculation is only required every R steps, so larger R increases the efficiency of the algorithm. However, it also increases the set up time, and this set up must be done every time the regions are updated, typically every 1000 steps. This means there is an optimum value for R. The runtime can be expressed as:

$$t_K = (2R + \frac{K}{R})t_L + (K - 2R - \frac{K}{R})t_S$$

$$t_L = xt_S$$

Where $t_K$ is the runtime to complete K cycles, K is the update period of the regions. $t_L$ is the time taken for a full force update, $t_S$ is the time taken for a partial update, and x is the ratio between these.

Minimising $t_K$ w.r.t. R and locating the minima, we find the optimal ratio between the hot and cold time steps for a given update period, K:

$$R = \sqrt{\frac{K}{2}}$$

Note that this number does not depend on x. For the typical update period of K=1000 this gives R=22 as the optimal value.

The time to run K steps at optimal ratio then becomes:

$$\frac{t_K}{t_L} = (2\sqrt{2K})(1 - \frac{1}{x}) + \frac{K}{x}$$

To determine how much faster this is compared to running every step at $t_L$ (i.e. always full force update) we must estimate a value for x. $t_L$ is the full force calculation time and scales as the number of force pairs in the system:

$$t_L = t_f N z$$

Where N is the number of atoms in the system and z is the number of interacting neighbours per atom. $t_f$ is the time to calculate the force between two atoms. $t_L$ has a fixed value for a given system size, $t_S$ will change as the cascade evolves and so the larger x is the more time is saved. $t_S$ depends on the number of bonds fully calculated in the hot region, as well as the partial calculations in the buffer region.

$$t_S = zN_H t_f + (N - N_H)t_p$$

Where $N_H$ is the number of atoms in the hot region. $t_p$ is the cost of extrapolating the force using eq. 2.2 for a given atom. These values are stored after summing the contributions from all relevant neighbours and so there is no z in this term. $t_p$ is expected to be much less than $zt_f$ but is still included as $(N - N_H)$ may be large.

$$x = \frac{t_L}{t_S} = \frac{t_f N z}{zN_H t_f + (N - N_H)t_p}$$

This approximates to $x \simeq N/N_H$ if the parabolic fit is negligible compared to the force calculations.

The theoretical speed-up of the force algorithm is then:

$$\frac{t_{Kfull}}{t_K} = \frac{K}{(2\sqrt{2K})(1 - \frac{1}{x}) + \frac{K}{x}} = \frac{1}{\sqrt{\frac{8}{K}}\left(1 - \frac{N_H}{N}\right) + \frac{N_H}{N}}$$

Where $t_{Kfull}$ is the runtime for K steps of the full force update algorithm. In the limit where only a small fraction of the system is in the hot region $N_H/N$ goes to 0 and the speed up factor goes to 11 times. This sets an upper bound on the efficiency of the algorithm. The factor limiting the maximum efficiency under these assumptions is the initialisation time, constraining R to be 22.

In real applications $N_H/N$ will not be vanishingly small and the efficiency gain will be less. However, the largest speed-up will be gained at the start of the cascade when the smallest time step must be used, this is a useful time to be able to accelerate the simulation's progress. Some gains will be made throughout the cascade: fig. 2.2 shows the theoretical speed-up against the fraction of the system involved in the cascade. Speed-up is seen even for large fractions of the system in the hot region.

The actual run time of the simulations also includes time spent in other areas of the code. Although the speed-up is only on the force calculation this is a major fraction of the run time.

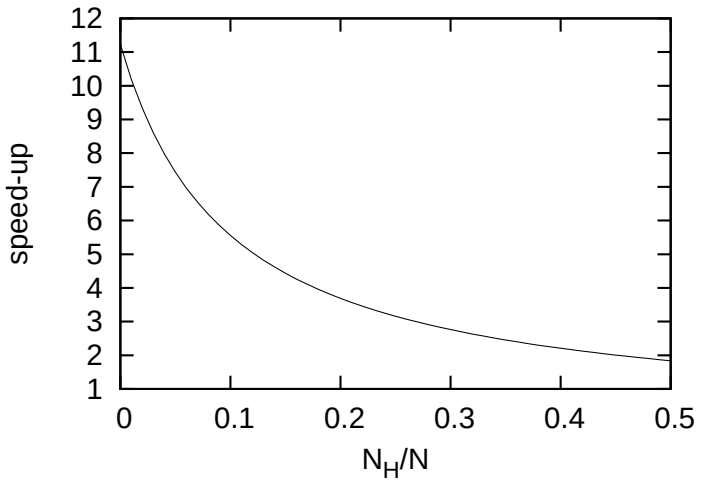


*Figure 2.2*: *Speed-up of the force calculation using the region based model compared to the standard model vs. the fraction of the system in the hot region. Most speed-up is gained for low fractions, although even relatively large cascades experience improved run times.*

## 2.8 Performance Measurments

Performance tests on a system of 250 000 atoms show that the ratio of $t_L$ to $t_S$ depends on the fraction of the system in the hot region as well as the number of cores used. The dependence on number of cores stems from the runtime for $t_S$ steps being so short that the serial fraction of the code quickly becomes important (approaching the limit of Amdahl's Law). Although the algorithm is fully parallel, the serial fractions in other parts of the code give the appearance of poor scalability. This effect would be less noticeable for larger systems. $t_L$ scales properly with number of cores as the serial fraction is negligible (at least for low numbers of cores). For a single core with no atoms in the hot region x = 15, while for 4 cores x = 9. For very large systems x should remain at 15 with increasing cores, as the serial fraction of the short time step will be negligible.

The initial cascade phase of a 20 keV pka in a box of 250 000 atoms was simulated using 4 cores. Fig. 2.3 shows the wall-clock time elapsed for simulations using traditional and modified algorithms. The system sees a three-fold decrease in run time over the first 40 000 steps of the simulation. After this the energy diffusion starts to limit the effectiveness of the modified algorithm. For clarity a graph of

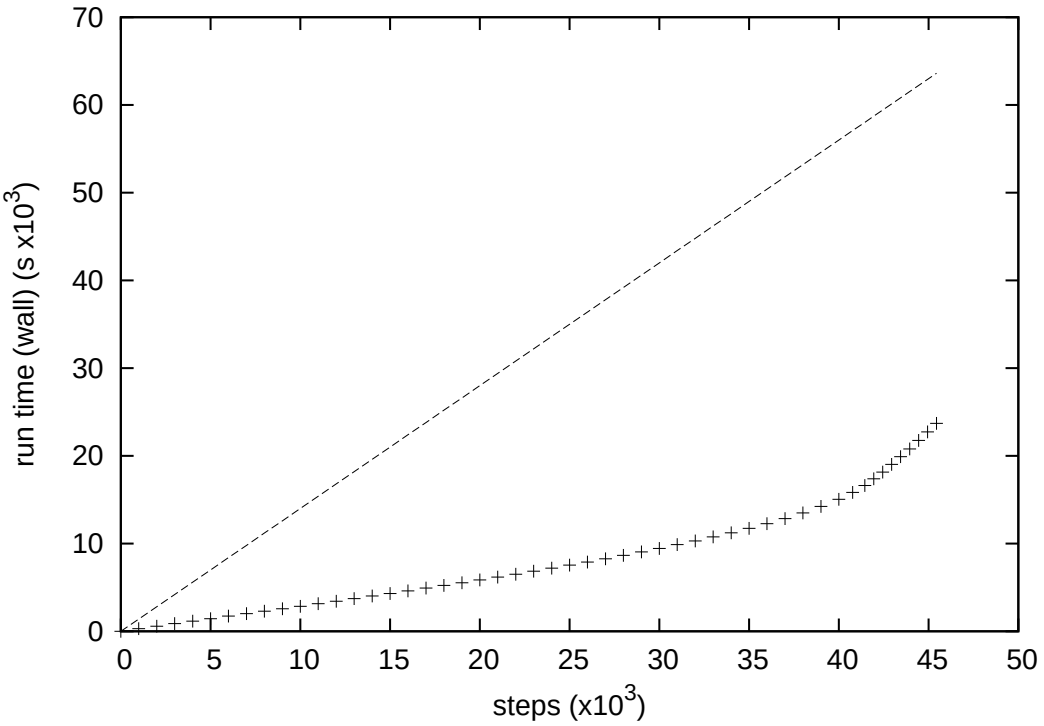


*Figure 2.3*: *Graph showing the wall-clock time time elapsed versus number of simulation steps. The system is a 20 keV cascade in iron using Finnis-Sinclair type potentials. The line shows the run time for a system with variable time stepping, but the same time step in all parts of the box. The algorithm is approximately 4 times faster over the first 35 thousand steps. After this a significant fraction of the system is in the hot region and the speed-up starts to diminish. Some speed-up is however gained over the whole course of the cascade.*

speed-up is provided, where speed-up is the ratio of run times of the traditional variable time step algorithm to the modified algorithm (see fig. 2.4). The initial speed up is 5-fold in terms of wall-clock time elapsed.

The speed-up for the algorithm vs. the fraction of the system involved in the cascade is shown in fig. 2.5. The value is well below the theoretical maximum for two main reasons: the theoretical model does not include the time taken for force extrapolations. The time includes all parts of the code, not just the force calculation. Additionally, the time spent outside the force calculation will be equal for both algorithms so will reduce the speedup. A speed-up of greater than 3 times is still seen for up to a 20% of the system in the hot region: enough to contain a fairly large cascade.

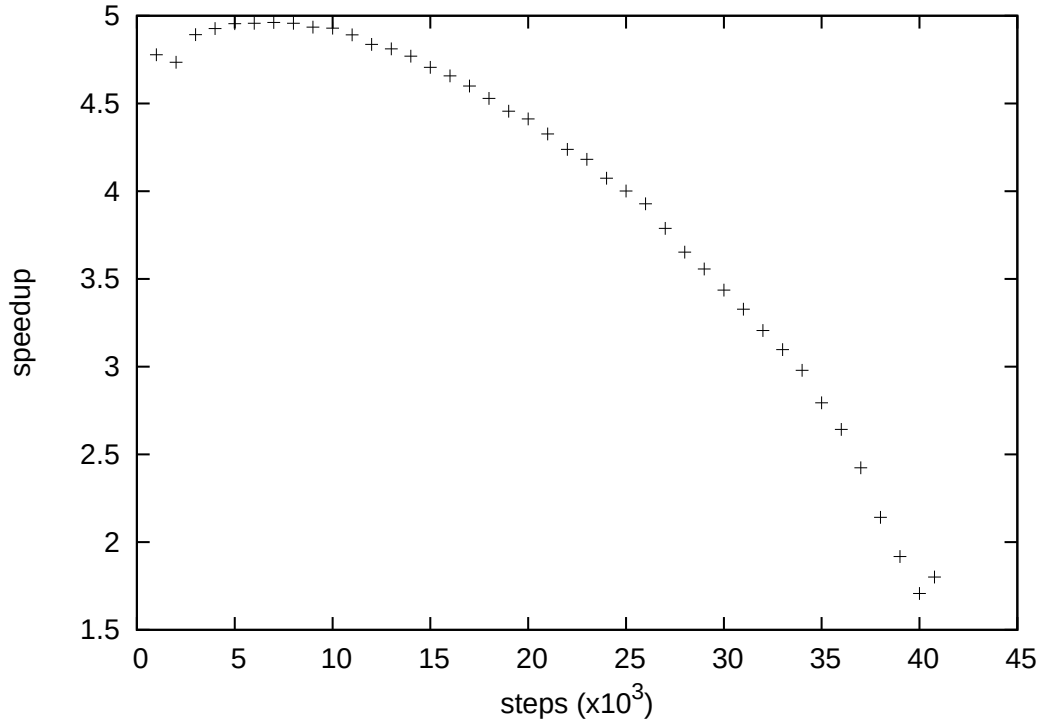


*Figure 2.4*: *Graph showing the traditional run time (no spatial time stepping) divided by the run time of the current algorithm. The system is a 20 keV cascade in iron using Finnis-Sinclair type potentials. Significant speed-up is seen particularly in the early parts of the cascade process. The speed-up falls as the energy diffuses, increasing the size of the hot region.*

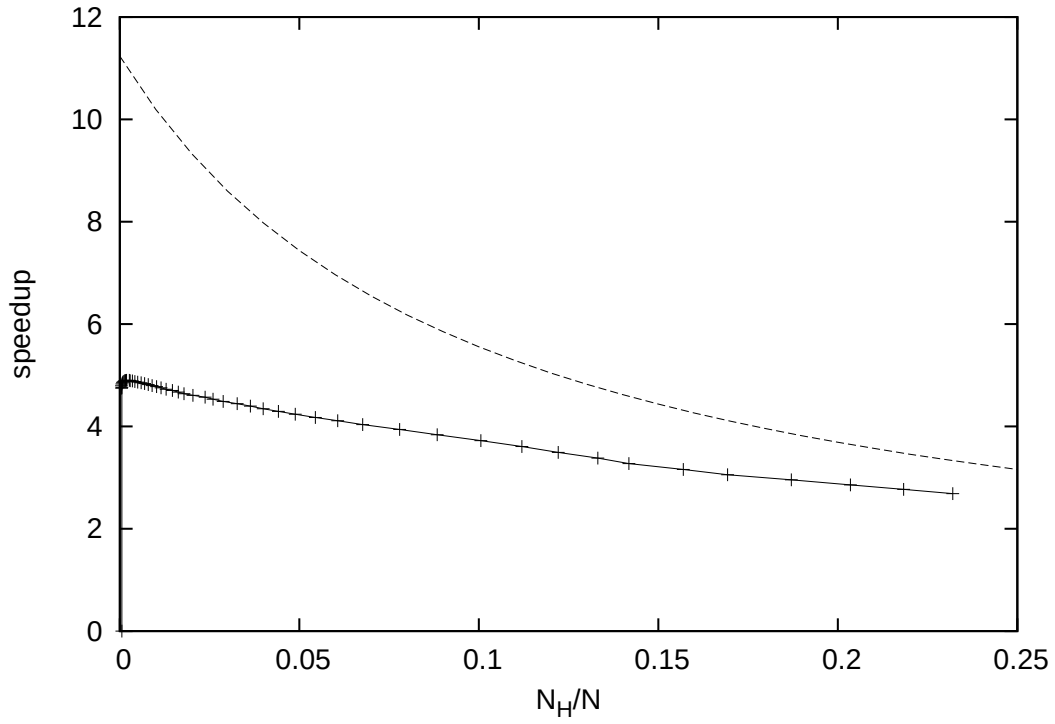


*Figure 2.5*: *Speed-up against fraction of system in hot region for a 20 keV cascade in iron using Finnis-Sinclair type potentials. The dotted line shows the theoretical speed-up which negates time spent in serial parts of the code as well as the cost of extrapolation. The lines tend to converge at higher values.*

## 2.9 Example Cascade

Fig. 2.6 shows a 20 keV cascade being simulated using the more efficient algorithm. Fig. 2.6.a) and b) show only atoms included in the hot region.

Image a) shows the initial stage of the cascade where the pka deposits substantial energy to several lattice atoms in a short amount of time. A time step of 0.003 fs is needed due to the high velocities involved. Already the energy has been distributed such that the highest energy atom in the system has 3.4 keV of energy. Only 1.4% of the sample is in the hot region, allowing significant speed-up.

Image b) shows the peak volume of the cascade. By this stage 14% of the sample is in the hot region and the energy has become dispersed between many atoms. The maximum energy in the system has dropped to 5 eV.

Image c) shows the system after most of the damage has annealed. By this stage there is no large energy imbalance in the system and the spatial time stepping is not needed.

Image d) shows a final defect yield for the system.

Another simulation is calculated for a 50 keV cascade in a box of half a million atoms on four processor cores. Fig. 2.7 shows the progress of the cascade, only the atoms in the hot region are included in the images. As the cascade evolves it can be seen that the hot region becomes several sub-regions, this poses no problem to the algorithm as it does not require a continuous region. These regions join up as the energy spreads through the system. In the last image shown, fig. 2.7 d), the cascade still only covers 5% of the box, allowing the algorithm to function efficiently. Table 2.1 shows the state of the cascade at the points when the four images were captured.

*Table 2.1: Statistics of cascade shown in fig.2.7*

| image | $E_{max}$ (keV) | $t_H$ (fs) | $N_H$/N (%) |
|---|---|---|---|
| a | 45.5 | 0.0007 | 0.05 |
| b | 35.4 | 0.0008 | 0.12 |
| c | 19.7 | 0.001 | 0.5 |
| d | 1.2 | 0.005 | 4.9 |

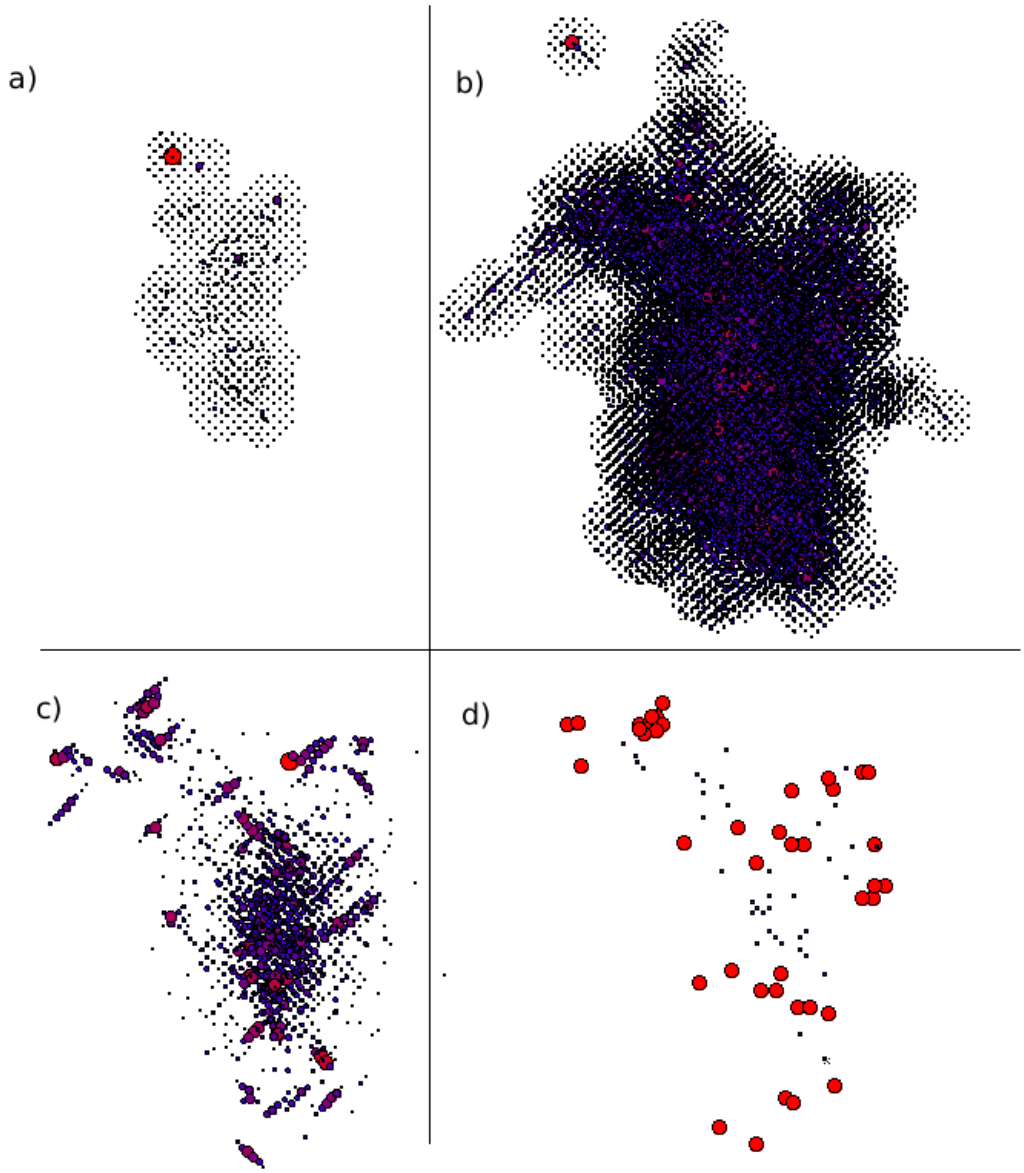


*Figure 2.6*: *Progress of a 20 keV cascade, in iron using Finnis-Sinclair type potentials, with the spatial time step algorithm. a) shows the initial stage of the cascade b) shows the peak volume of the cascade. In both these images only atoms in the hot region are displayed. c) shows the recovery of the lattice, here the whole box is being simulated at the same time step, atoms above a certain energy are shown. d) shows the defects detected in the final configuration. Large dots are vacancies, small dots are interstitials.*

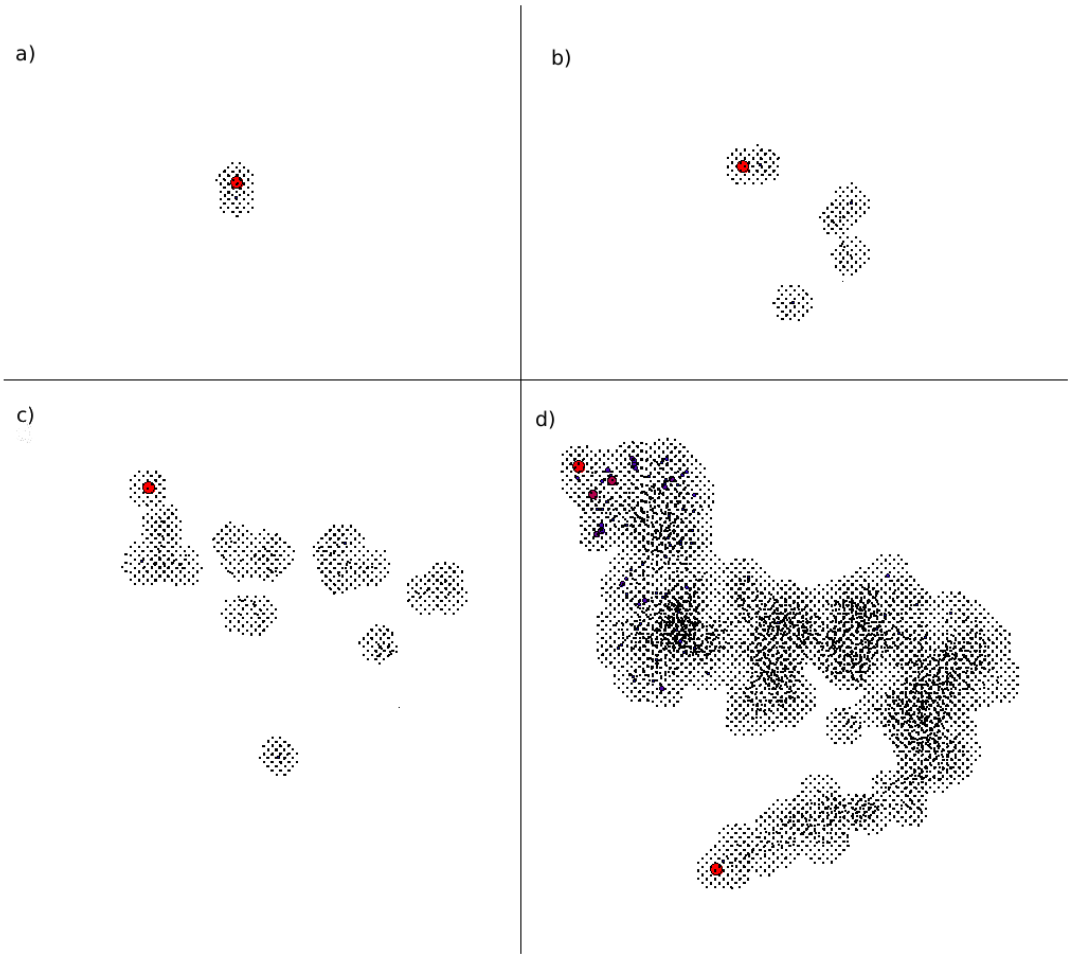


*Figure 2.7: A 50 keV cascade in iron using Finnis-Sinclair type potentials, run with the spatial time stepping algorithm, is shown at 4 stages. The high energy region around the cascade is automatically detected and shown as black dots in the image. The cold region is omitted for clarity. Images are taken after simulation time of: a) 2 fs b) 20 fs c) 51 fs d) 98 fs. They show the progress of the early part of the cascade. The pka initially deposits energy at several discrete sites. The sub-cascades triggered from this eventually overlap.*

## 2.10 Possible Improvements

As already mentioned, the limiting factor to the efficiency of the algorithm is the constraint placed on $R = t_C/t_H$ by the initialisation cost of the extrapolation procedure. Whenever the regions are updated, 2R full cycles must be calculated to allow the parabolic extrapolation steps to be executed. This overhead could be reduced by starting off with a low value of R just after the region update. Using points extrapolated from small R, the ratio could then be increased to larger R. This method could be repeated to allow large values of R to be reached without the overhead of having to run 2R + K/R cycles.

To use such an iterative method we must first carefully define the stability criteria we will use to remain consistent with the current algorithm. Let the time values of the extrapolation points be a,b,and c with c being the most recent point. The stability criteria used for the extrapolation are as follows: two full calculation points must be used as point b and c, and that the distance between b and c must be greater than the distance between c and the estimated value.

Let $F_n$ be the step number on which we perform the $n^{th}$ full force calculation. For example if we only perform a full force calculation every second cycle then $F_4 = 8$. Requiring that two of the points are fully calculated points, is the same as requiring that the $n^{th}$ term in the sequence is produced using two previous terms from the same sequence. To satisfy the stated stability criteria, we can use for point $F_n$, $c = F_{n-1}$ , $2b <= c$ , and $a > 0$.

The sequence of increases that obeys these criteria is given (after a few terms) by $F_n = F_{n-1} + F_{n-3}$. This series is similar to the Fibonacci sequence and the value of the ratio of consecutive terms tends to 1.46. Each iteration of this algorithm only requires one additional full force calculation but increases R by a factor of 1.46. This essentially removes the constraints on R: it is always beneficial to increase R, at least from the point of view of balancing initialisation time against run time. It takes 18 iterations of this algorithm to reach 1000 time steps, the typical value of K. This is substantially less then the number of full calculations used in the previous method K/R+2R = 89.

Although this method removes the balance between set up cost and running cost that constrained R previously, R should still not be set arbitrarily large for other

considerations. The larger R is, the lower the energy threshold for being in the cold region becomes, increasing the ratio $N_H/N$ which strongly effects the run time.

## 2.11 Conclusion

In conclusion, a reliable algorithm for accelerating cascade simulations has been developed. It significantly reduces the simulation run time by only using small time-steps near to the high energy cascade region. Under typical conditions it is 3 times faster than traditional Verlet integration.

# Chapter 3

# Ion Bombardment of Copper Surfaces

## 3.1 Introduction

In this chapter, simulation results of ion bombardment of a copper (110) surface are compared to scanning tunnelling microscopy (STM) experimental results (performed by Lane et al.[18]). Validating theoretical models by comparison to experiment is critical in gaining confidence in the model. Often the models used can simulate on time and length scales not typically available to experiment, such as angstroms and femtosecond scales. Comparing the long term results of such simulations to experiment, can not only validate the final result but also give additional insight and confidence in the short-scale mechanisms.

The comparison in this chapter is two-fold in purpose. The foremost goal is to reproduce the yield and distribution of surface damage observed in experiment in order to increase confidence in the simulation techniques used. Secondly, the mechanisms of damage formation on length scales not accessible to experiment can be studied, especially since the experimental technique is only sensitive to surface damage, where as simulations can be fully three dimensional. Assuming the final distributions match well, there can be some confidence in the mechanisms observed, even although they are not accessible to experiment (assuming the model to be physically based as is the case with the methods used).

In order to access experimental time scales a multi-scale approach was necessary. The experimental results are on equivalent distance scales to the simulations (angstroms) but the time scales are disparate. The initial bombardment is simulated using molecular dynamics (MD), which gives the initial yield of surface defects. MD typically models on up to the nanosecond scale, while experiment results were on the second scale as there was a delay between bombardment and measurement of the sample. To resolve this issue, the MD data was used as input into a kinetic Monte Carlo (KMC) model. This allows defects to diffuse and cluster on the second time scale, giving a distribution that can be directly compared to experiment.

Questions to be answered about the experimental data include: How the damage is formed, if there is any sub-surface damage, and to explain the slight excess of adatoms (surface interstitials) as compared to surface vacancies.

## 3.2 Literature Review

Ion bombardment is a common technique in experimental physics, as well as in manufacturing techniques such as field ion beam (FIB) milling, ion etching and ion implantation techniques. It allows materials to be modified in ways not easily achievable by other methods[19]. Additionally, undesired exposure to ion sources can damage the surface, and a clear understanding of this process is required to find damage reduction mechanisms. There has been much work, both experimentally and theoretically, in understanding the processes that occur when a surface is ion bombarded.

Numerous experimental studies of ion bombardment, across a broad range of materials, exhibit crater like impact sites. Cratering behaviour has been observed by STM in Xe ion impact of Pt(111) surfaces, with formation of a centralised crater surrounded by a ridge of adatoms[20], with adatom yield far in excess of binary collision model predictions. Ion impacts have also been studied experimentally in complex materials such as InGaAs thin films on GaAs substrates by atomic force microscopy (AFM)[21]. For each ion impact they observe the formation of a single crater with an adatom-rich periphery.

Ion bombardment of Si with a thin $SiO_2$ layer has been observed by STM[22]. This study observed crater formation at the interface between the silicon and its oxide layer, showing that the damage mechanisms can also be applied to internal surfaces. Ti surfaces have been studied experimentally by scanning electron microscopy (SEM), revealing crater formation[23] . SEM measurements of bombarded refractory metal alloys, reveal craters with multi-ring structures surrounding them[24]. These studies exhibit the wealth of materials that exhibit this behaviour as well as the range of experimental methods that can be used to analyse these defect formations.

There is an equally broad range of simulation work modelling the experimental phenomena. The accuracy of the technique and potentials used is of critical importance in reproducing experimental effects both qualitatively and quantitatively. Crater formation has been studied by MD with Lennard-Jones potentials[25]. Lennard-Jones potentials are considered to be an oversimplified description of a material: they are not material specific, they have low stacking fault energies and the vacancy formation energy tends to be too high[26]. However, if the correct behaviour can be exemplified by these simple potentials, it shows more complex approaches to be unnecessary. They study oblique impacts of a surface by ions and record the trend with varying impact angle. The trend is found to match predictions of a thermal spike model[27] although the quantitative yield can not be compared as the potential was not tuned to a specific material.

Averback et al.[28] studied damage formation mechanisms for a 10 keV Au ion bombarding an Au surface using empirical potentials. Their molecular dynamics simulations reveal the formation of adatoms above a disordered vacancy-rich region of the bulk. A model is proposed to explain the results in terms of viscous flow of a melt region. They assume energy is deposited evenly over a cylindrical track around the ion path in the solid. Heat diffusing radially outwards from this track melts a cylindrical segment of the material. The change in density, due to the melting, exerts an outward pressure on the surrounding lattice (assuming the liquid phase is greater in volume than the crystalline phase: this is not the case in substances such as Si and Ge[29]). The elasticity of the surrounding crystalline lattice contains the melt region on all sides apart from the open surface, therefore the liquid can viscously flow to the surface in order to alleviate the

pressure. They note that defects produced by this method exceed the amount that may be expected from the Kinchin-Pease equation. This is due to the damage being flow based, and not linked to threshold displacements which is assumed in Kinchin-Pease equation. This model should be relevant in materials with low melt temperatures such as Cu, Au, and GaAs.

This model is further developed by Ghaly et al.[30]. They note that as the melt region recrystallises, the vacancies are pushed back into the liquid phase as they have higher free energy in the lattice than in the liquid. This will result in the vacancies being clustered into a smaller region near the centre of the melt zone. Three possible mechanisms for cascade surface damage are identified in the study: linear cascade ejection events, viscous flow of the melt region, and micro-explosions. Micro-explosions refers to subsurface cascades that ballistically rupture the surface layers, forcing atoms from the surface layer to be sputtered or become adatoms.

All three effects may be seen in a given material, although the frequency and importance of each effect may differ depending on the bombardment type and material properties. The main factors determining the type of damage are the cohesive properties of the lattice as well as the energy density deposited by the ion at the surface. Disperse energy densities led to linear cascade events displacing surface atoms ballistically. At higher energy densities the damage formation is attributed to the viscous flow mechanism. The flow mechanism tended to produce a lot of damage in the form of one continuous cluster of adatoms. The vacancies left behind in the bulk could collapse into a dislocation loop. For high energy densities close to the surface, the micro-explosion mechanism could produce deep craters in the substance.

The above model is applied to a Pt system to directly compare results with STM data from another study[31]. They find qualitative similarity between the studies. Quantitatively, the adatom yield is overestimated by a factor of 2, after taking into account possible diffusive recombination events the adatom yield is still overestimated by 60%. It is suggested that this is due to the lack of phonon-electron coupling which gives too long a cooling period.

## 3.3 Method

The effects of argon ion bombardment on a (110) copper surface is investigated by Molecular Dynamics simulations. 250 000 copper atoms were set up in FCC configuration with a (110) surface in the z axis. The system was thermostated to 144 K and allowed to equilibrate for 10 ps.

The copper atoms were described by a Finnis-Sinclair potential, fitted to the properties of copper[32], which has previously been used for surface[33] and radiation[34] studies. It was considered if the argon potential should account for the ionic nature of the particle. Studies of Auger neutralisation effects show high neutralisation rates of incident ions. In particular a study of $He^+$ shallow angle bombardment of Ag shows a very high neutralisation rate, even though the contact time will be relatively small[35]. This suggests that high angle (close to perpendicular) impacts with greater penetration and contact time will rapidly neutralise the ion. Due to this the argon was described using only a pairwise potential as it has a closed outer shell. The same pair potential was used for Ar-Cu as for Cu-Cu, as argon has the same electronic core as copper. The correct atomic number is used for the ZBL[36] core repulsion term.

To initiate the bombardment event an argon atom was placed a few lattice spacings above the free surface. This atom was given 0.5 keV of kinetic energy towards the surface within a tolerance of 5°. The system is evolved by a variable time step Verlet algorithm explained in ch. 2.2. This allows the initial impact, resulting cascade and final defects after the thermal peak has dissipated to be studied.

This set up was chosen due to its similarity to the experimental study performed[18], which will allow comparison of the simulation results directly with experiment. Defects and clusters in the system were analysed by the method explained in ch. 3.4

Constant volume periodic boundary conditions were used along the x and y axis, with a free surface on the z axis. The choice of boundary conditions for the simulation cell must be made carefully. Open surfaces in the system lead to non-bulk like behaviours in certain regions and so are undesirable in directions that should appear continuous. The sample may also expand or contract accordingly.

Periodic conditions represent the bulk well but give rise to image interactions. These interactions can be minimised by picking large system dimensions at the expense of computation time. In practice a balance between system dimension and image interaction is chosen to keep interaction to a minimum.

The main interaction in the cascade systems is through wave propagation out from the cascade. Considering waves at the speed of sound in the medium an image-interaction time can be gained. For a typical system the interaction time is around 1 ps and so still during the lifetime of the cascade. These waves tend to be low energy compared to the cascade region and so their effects are not expected to modify the results significantly.

## 3.4 Defect Analysis

A Java program was written to analyse the defects in a crystalline system. The main scope of the program is to detect vacancies and interstitials and their distribution. Extra functionality was added to the program to allow it to also track the displacement of atoms.

Two methods were considered for detecting defects in the system. The simplest involves the comparison of the final configuration with a perfect lattice, normally the quenched input configuration. The number of atoms in the Wigner-Seitz volume around each initial lattice site is counted. If this number is 0 there is a vacancy, 1 for a normal site and greater than one for interstitials. This method can yield inaccuracies in position if the final system has drifted from the initial position (i.e. the centre of mass has changed). This is normally easy to adjust for by aligning the centre of masses of both systems, and checking that on-lattice atoms align in the initial and final systems.

The second method involves automatically detecting the lattice from the final configuration file. The nearest neighbours of an atom are detected, and the vectors to each calculated. This is repeated for several atoms in a region, and the vectors checked for consistency. If the vectors are consistent they can be used to step out a lattice over the system. This lattice may then be used for comparison with the final configuration to find defects as before. The advantage

of this method is that it allows for skews, stretches and thermal expansion of the lattice that may have developed during the simulation. It would also be possible to use the method to analyse a system composed of multiple grains by fitting a lattice to each region (this use is not explored currently).

For the present simulations the simpler comparison method was found to be sufficient, so was used for this study. The second lattice fitting method was also implemented in the code and gave similar results to the simpler method. After detecting the defects, close interstitial-vacancy pairs were eliminated: opposing defects in neighbouring cells were assumed to either be caused by thermal fluctuations or to have a short lifetime and so were eliminated.

For efficiency the atoms are split into a link-cell based arrangement. The system is split into spatial cells using a three dimensional grid that has spacing related to the interaction radii and typically includes several neighbour cells. Atoms with coordinates inside a cell are listed as a member of that cell. Now instead of searching the whole system for neighbours of an atom, it is sufficient to search a $3^3$ block of cells, centred on the atom's current cell. This means that neighbour searches no longer scale with the size of the system, rather with the fixed volume of the $3^3$ cells.

Additional code was added to track changes in the lattice configuration. Of interest were the displacement vectors for atoms that have changed site. This is simple to calculate given the initial and final configurations. Atoms that have changed their nearest neighbours are also tracked. This separates out correlated motion of whole regions from ballistic or diffusive re-ordering events. Such atoms can be detected by comparing the initial and final neighbour lists of a given atom.

After the point defects are detected, clusters of like defects are identified. Defects at up to second nearest neighbour distance to each other were considered to be clustered. The code produces the size and frequency distribution of the clusters of each type (vacancy or interstitial). For the presence of a secondary element, such as helium, the clustering properties are also detected, as well as the properties of combined clusters, i.e. helium-vacancy clustering.

Although the algorithm was designed to analyse cascade debris, the code is general

enough to study other phenomena. Slip plains and dislocation motion can be detected using the code that detects changes of neighbour. This code eliminates correlated motion and so only highlights the atoms either side of the slip. The lattice fitting part of the code could be used for detecting the position, orientation and extent of regions in a polycrystalline substance.

### 3.4.1 Thermostating

Thermostating in cascade simulations must be done with care. Without a thermostat the system will be heated to a final temperature greater than the initial equilibration temperature by the energy of the pka. This is due to the finite size of the samples used and the lack of electronic heat transport. In real materials long range phonons and electronic excitations quickly dissipate heat away from energetic regions.

For a large enough system, with low electronic heat transport, this heating can be considered acceptable as the temperature change decreases with system size, being vibrationally transferred to the rest of the sample. However, for a copper system the thermal conductivity is quite high when compared to materials such as iron; 80 and 401 W/(m.K) for iron and copper at room temperature respectively. In this case it was decided that the effects of energy transport out of the cascade region by electrons and phonons would be significant.

The Nosé-Hoover thermostat was used[37]. Nosé-Hoover applies thermostating through a frictional drag on the particles. For out-of-equilibrium radiation damage in metals this approach is better than, for example, a Langevin thermostat which applies random external forces. Particles with energies above 5 eV were excluded from the thermostating. The thermostating was only updated every 1 fs, so that the time step chosen would not affect the thermostating values. The argon atom is not included in the thermostat. It is neutral and so does not strongly couple to electronic transfer.

Energy is transferred from the argon atom to the copper lattice through ballistic collisions driven by core electronic repulsion. The copper atoms surrounding the ion track become highly excited, leaving their lattice sites and causing further collisions. These collisions are not thermostated: the Nosé-Hoover algorithm

is designed for lattice vibrations and so would too strongly penalise ballistic motion.

Once the energy spreads enough for the ballistic phase to end, the excess kinetic energy translates into increased vibrational properties of the atoms. At this stage the atoms are included in the thermostating. Thermostating was initiated when all particles in the system have less than 5 eV of kinetic energy. This value is well below the atomic threshold displacement energies in copper of $E_d$[110]=18 eV to $E_d$[111]=29 eV[38] ensuring the system is in the vibrational regime.

The thermostat was scaled to reflect the thermal conductance of the substance. Fourier's law of heat conduction can be stated as:

$$q = KA\Delta T/x$$

Where q is the heat transfer rate, K is the thermal conductivity, $\Delta T$ is the temperature difference across the sample, A is the heat transfer area, and x is the thickness of the material. For a cubic block of material A/x=x. The excess energy in the system is:

$$E = \frac{3}{2}Nk\Delta T$$

Therefore, the characteristic time for heat transfer in the system is:

$$t = \frac{E}{q} = \frac{3Nk}{2Kx}$$

This gives a characteristic time of 0.16 ps for heat to flow out of the system. This is used to set the softness of the Nosé-Hoover thermostat.

### 3.4.2 Barrier Calculation

Energy barriers for adatom motion on the (110) surface were calculated in order to explore the surface energetics and diffusion paths. An adatom at a stable point on a (110) surface sees a rectangular lattice of atoms surrounding itself

with stable adatom sites being the centre of the rectangles. The environment is asymmetric with easier motion along channels than across them, where $[1\bar{1}0]$ is along the channels and [001] is across the channels (fig. 3.1).

The energetic barriers to interstitial site hopping were calculated by comparing relaxed energies in the system. The fully relaxed energy, with the interstitial at a minima and no constraints, was taken as a reference point. The nudged elastic band method[39] was then implemented in the code to find the peak of the energy barrier. This technique moves the adatom along a line adjoining two stable interstitial sites, subject to constraints; the component of the interstitials motion parallel to the path is constrained to stop it relaxing back to the minima, while the components of motion perpendicular to the path are free to relax. The surrounding lattice is also allowed to relax but not to translate. The energy barrier at 0 K can be taken as the difference between the peak energy found along the path and the fully relaxed state. This yielded a 0.33 eV energy barrier for along channel hopping and 1.17 eV for across channel hopping.

The barriers were verified by a secondary method using dynamic simulations. High temperature MD was simulated and the hopping rates of isolated adatoms were recorded. From the jump rate and the oscillation period, the probability of a successful jump can be calculated. By rearranging the Arrhenius equation the energy barrier can be found:

$$E = -kTln|\frac{\tau_{osc}}{2\tau_{int}}| \tag{3.1}$$

Where $\tau_{osc}$ is the oscillation period of the interstitial, and $\tau_{int}$ is the jump frequency. This yields a value of 0.304(12) eV for the along channel hopping, which is close to the static barrier calculation. The two methods seem in good enough agreement to show the validity of the approaches. The dynamic barrier would be expected to be slightly lower: the barrier height varies with thermal fluctuations and the average will be weighted to the lower values as they allow a much greater number of hops.

The dynamic method also showed an interesting mechanism for diffusing across channel which may have been missed if only the static calculations were performed. An interstitial may cross to another channel by replacing one of the

corner atoms surrounding it, resulting in a diagonal move as shown in fig. 3.1. The barrier for this is estimated to be 0.42 eV, as calculated using the dynamic method and eq. 3.1. This is significantly lower than the direct cross channel hopping barrier.

Additional energetics were calculated by the nudged elastic band method to explore clustering behaviour. Energetics were calculated for the dissociation of a single adatom from a surface cluster. The results are summarised in fig. 3.2. Interstitials in adjacent surface channels have little effect on the motion in an adjacent channel: as can be seen in the top right panel of fig. 3.2, the barrier to diffusion along channel is only increased by 0.05 eV when an interstitial is present in the next channel. The top left panel shows that interstitials in the same channel have stronger binding, almost doubling the along channel diffusion barrier. Averaged over the configurations, the presence of a neighbouring adatom in the same channel increases the diffusion barrier by 0.32 eV along channel and 0.12 eV across channel.

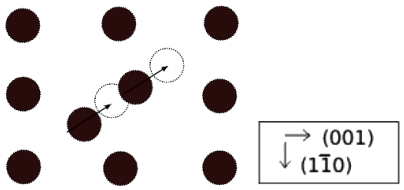


*Figure 3.1*: *Diagram of replacement mechanism, which allows cross-channel diffusion on a (110) copper surface. An adatom displaces a surface lattice atom, taking its place and forming a new adatom.*

## 3.5 Results

90 cascade simulations were performed varying the angle to the surface of the argon's trajectory within 5° and varying the point on the surface that the argon ion is aimed at. This study looks at: the final yield of defects, the clustering of defects, the path of the argon atom, and the formation process of the damage.

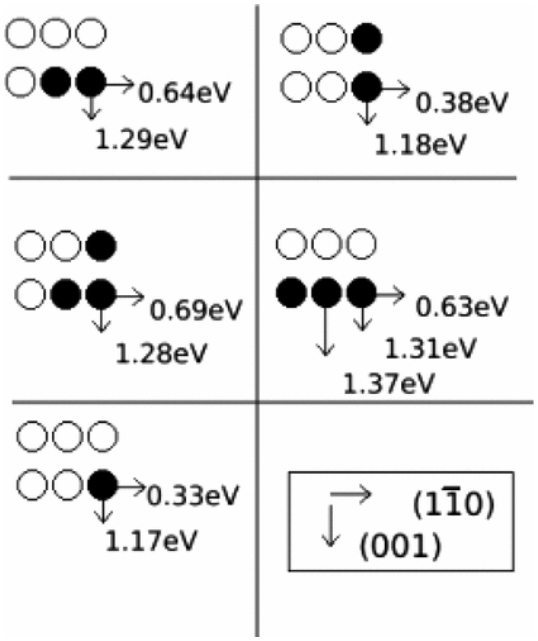


*Figure 3.2*: *Shows the surface diffusion barriers from static calculation for adatoms and small clusters on a (110) copper surface. [1 $\bar{1}$ 0] is along the surface channels, [001] is across the channels. The barriers given are for the movement of a single adatom along the direction shown (not the whole cluster) until the saddle point is reached; the adatom is free to relax away or toward the surface.*

### 3.5.1 Damage Formation

The yield and distribution of defects resulting from various cascades, as well as the formation process of the damage, is analysed. The number of lattice defects was tracked during a cascade. The defects were detected by the method explained in ch. 3.4. This number includes unstable pairs caused by melting and collisions. In this regime the definition of a defect is ambiguous and is used only as a means of tracking cascade progress. However, the defect count after the cascade has settled is a meaningful measure of damage. A typical graph of the defect yield during a cascade is shown in fig. 3.3. The thermal peak occurs at around 1 ps and the damage is mostly settled (at least on the ps scale) by 2-3 ps. Runs were continued for another 5 ps during which at most one defect pair recombined, showing the stability of the configuration on the pico-second scale.

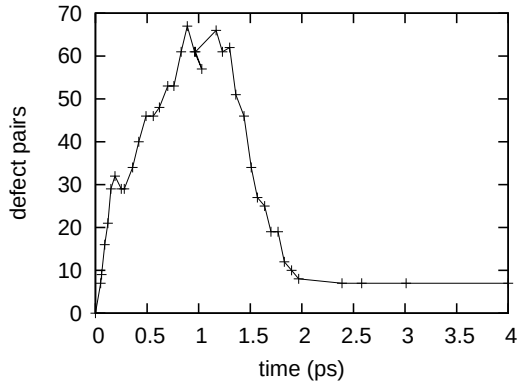


*Figure 3.3*: *Graph of the time evolution of the number of defect pairs in the system for a 0.5 keV Argon atom bombarding a copper surface. Peak damage is after 1 ps, with recovery by 2 ps.*

The yield and distribution of the final cascade damage was analysed. Fig. 3.7 shows the typical final distribution for a near surface cascade. Analysing the full data set reveals that 11.9(10) Frenkel pairs were formed per cascade, of which 10.3(8) produce adatoms. The other atoms evaporating or (rarely) forming subsurface interstitials. 72(3)% of the vacancies formed were in the single crater, the others were predominantly subsurface. The Ar atom was ejected from the system 41(6)% of the time.

A strong correlation was found between the penetration depth of the pka and the damage formed by the cascade, as shown in fig. 3.4. The deeper the pka

penetrates, the less damage there seems to be (including bulk damage). Deeper collisions are caused by channelling between lattice planes, while shallow collisions tend to be caused by a more direct impact with a surface atom. The channelled collisions undergo several collisions with atoms along the channel's sides, which spreads the energy over a larger volume. A lower energy density will lead to fewer defects. Additionally, the energy is deposited further from the surface, reducing the cascade-surface interaction.

During a cascade, atoms tend to be pushed outwards from the impact site, before being pushed back towards their original site by the surrounding lattice. Near the surface this recoil is not present, as there are no atoms to push the displaced atoms back onto their sites, and so surfaces tend to allow easier interstitial formation. Therefore, shallower cascades will be expected to produce more surface damage as long as the displacement wave moving out from the cascade reaches the surface.

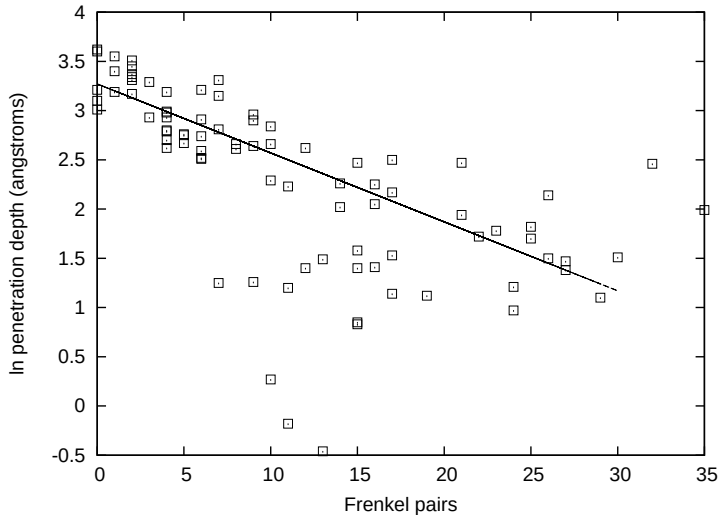


*Figure 3.4*: *Number of Frenkel pairs (NF) produced vs. ln of the penetration depth (d), defined as the lowest point reached by the Ar ion below the average position of the surface layer, for 0.5 keV bombardment of a (110) copper surface. The anomalous very low values of d correspond to bouncing off the surface and are excluded from the fit line. d=23.3(2)exp[0.074(5)NF].*

### 3.5.2 Impact Craters

The crater formation process is analysed in this section. To study the flow of atoms during the cascade, first nearest neighbours were calculated for each atom both before and after the cascade. This information was used to identify atoms that have switched at least two new nearest neighbours during the cascade process. A plot of the displacement trajectories for such atoms is shown in fig. 3.5.

There is more order to the diagram than might be expected if the cascade were thought of as locally melting the region. Atoms move towards the surface by a series of replacement collision chains. This draws matter from the bottom of the crater, where the atoms displaced downwards by the pka are exerting most pressure, up along the sides of the crater. Adatoms are formed fairly early on in the simulations, due to replacement collision chains terminating on the surface. The thermal spike phase is not strongly influential in the formation process.

### 3.5.3 Stress Waves

To further the study of the interactions during the cascades the atomic stress was calculated and tracked during the simulations. Atom stress can be defined by[40]:

$$\sigma_i^{\alpha\beta} = \frac{1}{\Omega_i}\left(\frac{1}{2}\sum_j f_{ij}^{\alpha} r_{ij}^{\beta} - M_i v_i^{\alpha} v_i^{\beta}\right)$$

Where $f_{ij}$, is the force on atom i due to atom j and $r_{ij}$ is the vector joining sites i and j. $\Omega_i$ is the atomic volume and the sum is over all neighbours of i. $M_i$ is the mass of atom i and $v_i$ its velocity. The far right term is linked to the kinetic energy of the atoms.

By calculating the atomic stresses during the cascade, stress waves can be identified in the system. These waves seem to be a mechanism for dissipating the cascade energy rapidly through the lattice without mass transport. They tend to follow close-packed planes and are prevalent parallel to the surface layer. The

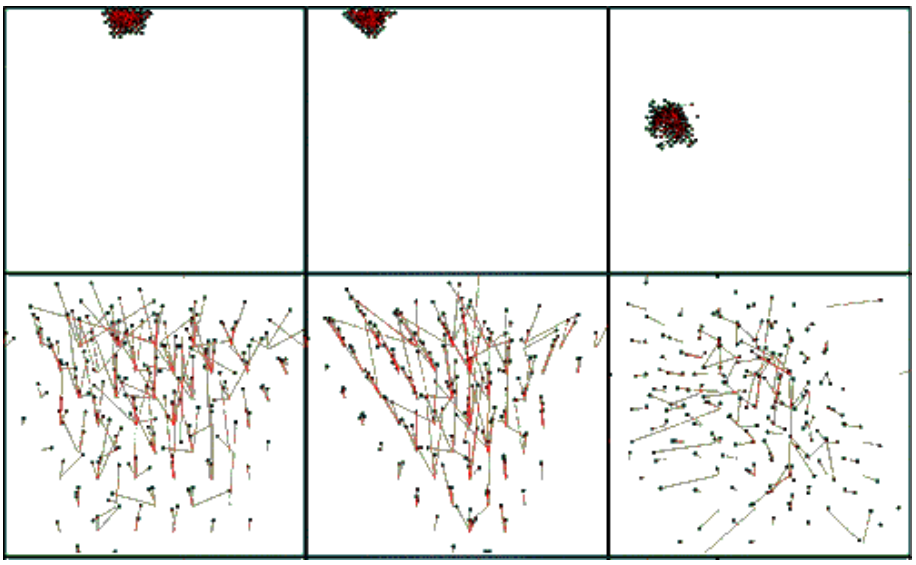

*Figure 3.5*: *The relationship between initial and final positions of atoms after a typical surface cascade. The system was a 0.5 keV Ar bombardment of a (110) copper surface. Black squares indicate atoms which have at least two near neighbours different from the initial state. Red lines link the initial position of atoms to their final position. The top 3 images are the x, y, and z projections for the whole system, showing the displacement trajectories of the atoms. The lower images are magnified views of the crater. They show a systematic structure to the displacements rather than the disordered pattern one might expect from localized melting. Correlated motion of matter can be seen moving along the sides of the crater towards the surface.*

wave propagation is shown in fig. 3.6. The wavefront propagates at 23 x $10^3$ $ms^{-1}$, well into the hypersonic regime (speed of sound in copper is 4760 $ms^{-1}$[41]).

Previous models have been proposed, invoking hypersonic wave fronts to explain high spluttering rates in copper/argon collisions. In these models, due to Carter[42] and later Webb[43], the wavefront propagation is tracked by measuring ejection times and locations in simulations. By averaging over many cascades they can produce a wavefront from the data. The wave expands cylindrically around the ion track at a rate of 17.6 x $10^3$ $ms^{-1}$. This localised expanding cylindrical wave front could be the trigger of the more channelled phenomenon observed here. In their study the energy of the Ar is 10 times that of the present study and the surface plane is (001). The difference in velocities between the models is likely due to the change in crystallographic plane.

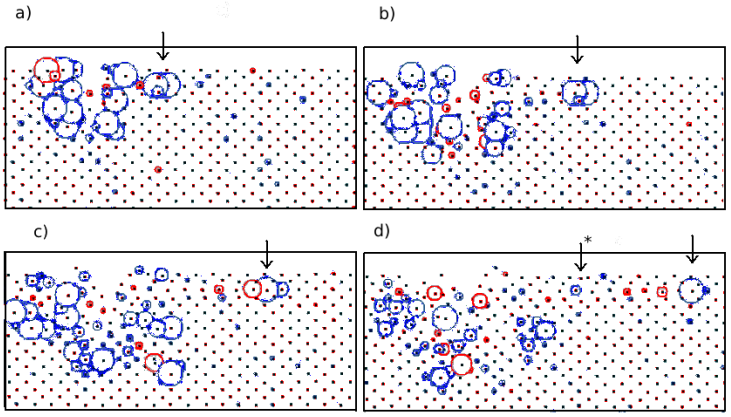


*Figure 3.6*: *Shown are four images of the stress in the lattice during a cascade. The system was a 0.5 keV Ar bombardment of a (110) copper surface. Blue circles show positive stresses, red circles show negative stresses. The size of the circle represents the trace of the stress matrix. The arrow marks the wavefront position. a) 60 fs: Stress wave is seen to start propagating. b) 90 fs: Wave continues along plane. There is no mass transport and atoms stay close to their original sites. c) 120 fs: A negative stress region can be seen just behind the wave front. d) 170 fs: Wave still propagating. The wave's disturbance has pushed a particle from the second row of atoms up to the surface level. Such events may be a mechanism for distant adatom formation and is marked with an arrow and asterisk(*) in the diagram.*

### 3.5.4 Comparison to Experiment

The final damage and distribution is carefully compared to experimental results. Experimental data was gathered and analysed by P. D. Lane and R. J. Cole[18] to quantify the surface defects and their distribution. They analysed 30 images of ion bombardment sites, taken from a scanning tunnelling microscopy (STM) experiment performed by their group. The present author was not directly involved in this part of the analysis.

On average there were 10.4(6) adatoms per event and 9.2(3) vacancies in the experimental data. This counts only defects directly on the surface as STM is limited to this region. The clustering of the defects can also be analysed from the images. Typically a centralised vacancy cluster was observed surrounded by islands of adatoms. Some typical STM images are shown in fig. 3.8. There is qualitative similarity between the STM images and simulation images (fig. 3.7), with both showing a centralised vacancy cluster surrounded by adatom clusters. The simulation data shows the conical shape of the crater, which is not apparent from the STM analysis.

Comparing the data to experiment must be done with care as the number of Frenkel pairs produced is not the same as the number of adatoms that will be observed. Differences arise because interstitials can be formed subsurface where the STM technique used will not detect them. Additionally the MD simulations showed that the impact could eject atoms from the system, a process known as sputtering. Another issue complicating the comparison is the sampling bias introduced by the image analysis technique used by the experimental group. The analysis technique used by the experimental group involved selecting individual impact images by hand, from the STM data. This will bias towards higher yield impacts: as small cascades that do not form clear craters and adatoms are less likely to be analysed. As can be seen from the STM images, fig. 3.8, the data is approaching the limits of resolution of the images. A better approach would have been to count all defects over as large a surface area as possible, and then divide by the number of ion impacts expected in that area for the given beam fluence.

The issues of evaporation and subsurface damage can be directly accounted for by

analysis of the defects produced in the MD. This is taken into account by filtering the defects formed by height, only allowing a small range of values relating to the top layer of the crystal, so that only surface damage is counted. Adjusting for the sample bias in the experiment requires a threshold to be picked for what size of cascades would be visible in the STM. The eventual threshold decided on, after discussion with the experimental group, was that at least one cluster of 3 adatoms would need to be present to ensure detection. The data with only surface defects included and adjusted for STM visibility, will be referred to as the filtered data.

Fig. 3.9 shows a comparison between the experimental and simulation data, split by frequency of different sizes of clusters. The full simulation data set, as well as the filtered data set, are compared. The experimental distribution shows a peak around 4-5 adatom cluster size. The simulation data sets show much more small clusters of size less than 3 than is seen in experiment. The filtered data has a slight reduction in small clusters, but still a large abundance as compared to experiment.

Fig 3.10 shows the cumulative yield of adatoms summed over the various cluster sizes. The full simulation data set has a total of 10.3(8) adatoms which is in good agreement with the experimental value of 10.4(6). However, this is not the correct data to compare with as it contains cascades that are too small to be reliably detected by the STM. The total sum of adatoms per cascade for the filtered data is 12.6(8), 2.2(10) adatoms higher than observed experimentally.

To summarise, the filtered simulation data, when compared to experiment, shows more small clusters and a higher yield of adatoms. The observational threshold is assumed to be correct as a higher threshold would give discrepancies in the total damage. The distribution discrepancy is most likely due to the different time scales. The simulations lasted several picoseconds, enough time for the energy of the cascade to dissipate. However, the experimental images were taken around 30 minutes after the bombardment, possibly allowing the atoms time to diffuse.

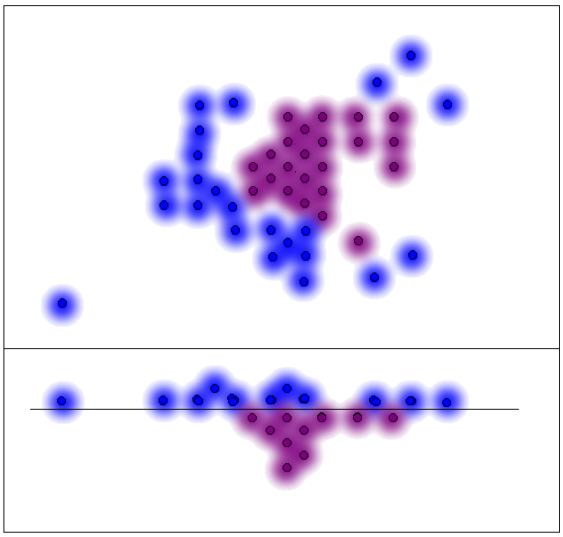

*Figure 3.7*: *Typical distribution of final defects, for a high-yield collision of 0.5 keV Ar ion with a copper (110) surface, viewed from above the (110) surface (top) and a perpendicular slice ($\bar{1}10$) (bottom); shown are vacancies (red squares) and interstitials (blue circles, with shaded halo). A background shading was added to highlight the six clusters of sizes 17, 2, 1, 1, 1, and 1.*

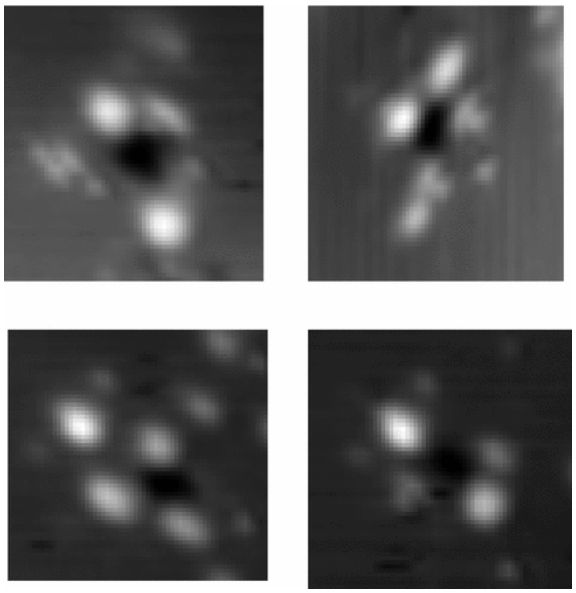

*Figure 3.8*: *STM images of craters above cascades (courtesy of P.Lane); all images are 44 nm. The vacancies (dark) lie in the center of the crater and the interstitials form a surrounding halo. The number of vacancies/adatoms are calculated by dividing the total area occupied by vacancies/adatoms around the impact site by the area of the unit cell.*

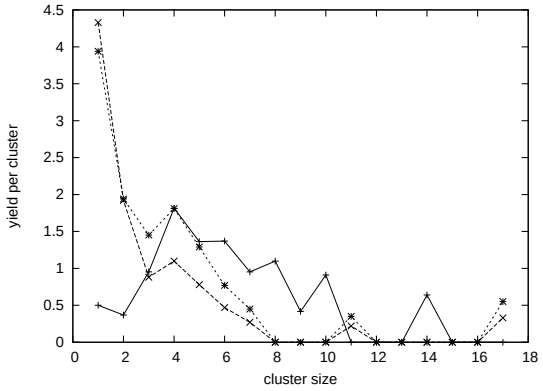


*Figure 3.9*: *Shown is the yield of adatoms per cascade, separated by cluster size, for a 0.5 keV Ar ion striking a (110) copper surface. Filtering is applied to remove data that would not be observed by the STM image analysis techniques used. The black solid line is the experimental values for adatom clusters per cascade. The dashed line with crosses is the unfiltered data. The dashed line with asterisks is the data filtered so that only cascades with at least one adatom cluster of 3 atoms are counted. The filter decreases the yield of smaller clusters and emphasises the larger cascades.*

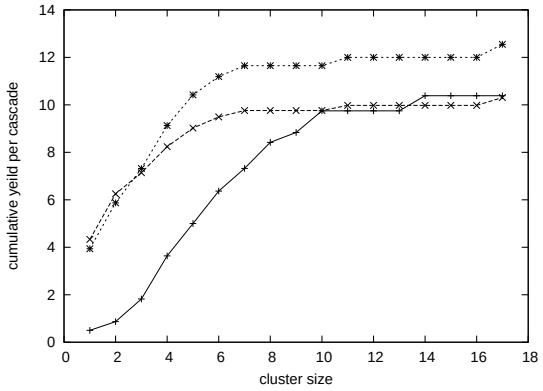


*Figure 3.10*: *The cumulative yield of interstitial clusters split by cluster size is shown. The cascades were a 0.5 keV Ar ion striking a (110) copper surface. The black solid line is the experimental values for adatom clusters per cascade. The dashed line with crosses is the unfiltered data. The dashed line with asterisks is the data filtered so that only cascades with at least one adatom cluster of 3 atoms are counted.*

## 3.6 KMC Surface Model

To explore the effects of diffusion on longer time scales, a KMC-based surface hopping model was written. This model uses a similar construction to the object kinetic Monte Carlo model described in ch. 4.7.1. The model accounted for nearest neighbour diffusion and binding, using the barrier data in fig. 3.2. Hops along and across channel were allowed, taking into account the neighbour binding effects at first nearest neighbour. The mechanism for diagonal cross channel diffusion (fig.3.1) by replacement of a lattice atom is also included in the model.

The simulations allow annihilation events between vacancies and adatoms. The adatom is bounded by 4 surface atoms; when one of these is a vacancy annihilation is assumed to occur. Since the crater had a conical shape it may be possible for an adatom to diffuse further into the crater and so re-open the surface site. That is, a vacancy site may be able to absorb more than one adatom. However, the crater tended to be shallow and rapidly tapered (fig. 3.7). Due to this the mechanism was not included in the model and each vacancy was completely annihilated by one adatom.

The defect configuration in the KMC model was initialised using final cluster distributions from the MD simulations. The system was evolved at 144 K for 30 minutes of simulation time to match the delay in measurement of the experimental data. After simulating the diffusion, the data was filtered to remove any cascades that did not produce at least one cluster of 3 adatoms as these would not be detected in the experimental analysis. The filtered distribution of clusters formed can be compared directly to the experimental distribution (fig. 3.11). It can be seen that there is no longer a large excess of single defects in the simulation data, as was the case with the previous distribution from the MD data (fig. 3.9). However, the distribution of the KMC data is still slightly skewed towards smaller clusters, as compared to experiment.

The cumulative distribution is shown in fig. 3.12. It can be seen that the total yield of adatoms is less than in experiment. After the KMC there are 8.5 adatoms and 7.4 vacancies per cascade. These are both lower that the experimental values of 10.4(6) adatoms and 9.2(3) vacancies. Both show an excess of adatoms by just

over one adatom per cascade.

The KMC seems to produce a much closer distribution of clusters, and a similar yield distribution up to around adatom clusters of size 8. There is a lack of larger adatom clusters in the KMC data, as well as a slightly decreased yield. A possible explanation for this could be the weak cross channel binding energy predicted by the MD barrier calculations and used in the KMC. If this binding is higher in reality, it would produce a greater yield of larger clusters. An increase in this binding would also increase yield as more defects would be bound in clusters, reducing the number of recombination events.

An alternative explanation is that there is more sample bias in the experimental technique than is accounted for by requiring a cluster size of 3. Varying this filter increases the yield of adatoms in the simulation data noticeably, as small clusters are removed from the data set.

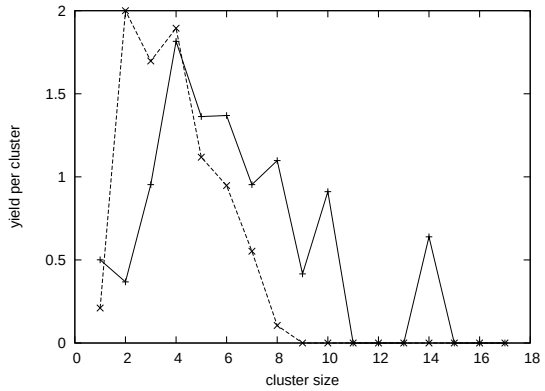


*Figure 3.11*: *The yield of adatoms per cascade, separated by cluster size, for a 0.5 keV Ar ion striking a (110) copper surface. The solid line is the experimental data. The dashed line is from the computational data, after running a KMC algorithm.*

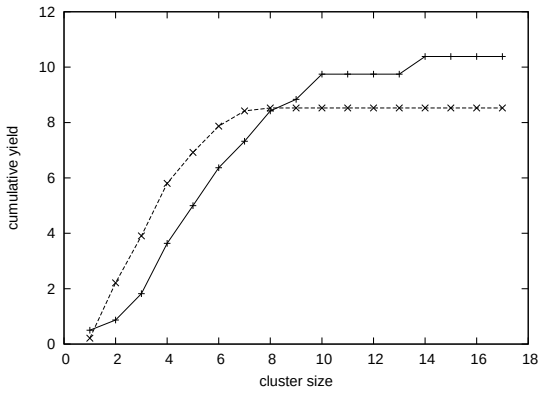


*Figure 3.12*: *The cumulative distribution of adatoms, summed over cluster sizes The solid line is the experimental data. The dashed line is from the computational, after running a KMC algorithm for bombardment of a (110) copper surface and the subsequent diffusion. The computational data is filtered to match what would be visible in the experimental analysis.*

## 3.7 Conclusions

The original MD data shows a small excess of adatoms and surface vacancies when compared to the STM data. The distribution of the surface clusters is heavily weighted towards much smaller clusters compared with the STM distribution. Running KMC simulations on the MD data affects both the yield and distribution of surface damage. The yield becomes slightly smaller than the experimental value, although retains a good ratio of adatoms to surface vacancies. The clustering of defects becomes much closer to the experimental distribution after the KMC simulations.

Sub-surface interstitials are rare, although interstitials are lost by high speed ejection from the surface. The vacancies formed tend to be close to the surface and clustered into a single crater. Since the cluster has a conical shape sub-surface, some vacancies are not observed by the STM imaging. The simulations seem to balance these different loss effects well, giving a similar difference between the number of visible interstitials and vacancies. The experimental observation of more adatoms than vacancies can therefore be explained by the combination of these factors: the number of adatoms ejected from the system is outweighed by the unobserved vacancies in the conical crater, giving an excess of adatoms overall.

Study of the argon atom's trajectory revealed a strong inverse correlation between penetration depth and damage to the lattice. When the cascade overlaps the surface, they interact strongly to cause craters and adatom clusters. The interaction appears more directed than may be obtained from a local melt region. Replacement-collisions chains orient preferentially towards the surface to alleviate the compression at the bottom of the crater, while taking advantage of the depletion region above this for easier motion.

Study of the atomic stress reveals stress waves propagating along sub-surface close packed planes. These transport heat from the cascade region to the surrounding lattice.

# Chapter 4

# Mobility of Bubbles and Voids Under Irradiation

## 4.1 Introduction

This chapter studies the interaction of radiation cascades with voids and bubbles in iron. Both molecular dynamics (MD) and object kinetic Monte Carlo (OKMC) techniques are used to study the phenomenon on different time scales. During the MD simulations a mechanism of interaction between voids and cascades is identified. The long term diffusion of clusters of defects is not on a compatible time scale with radiation cascade simulations for most reasonable temperatures. This exemplifies the need for a multi-scale simulation approach, in order to access time and distance scales comparable to experiment. To explore how this mechanism interacts with other processes in the system it is implemented in an OKMC model. This allows the time-scale gap to be resolved, so that cascades debris can be introduced into a sample that is running on diffusive time scales.

The formation of voids and bubbles is discussed below. Under neutron irradiation voids will form and grow in iron. Vacancies in iron are self-attractive[44] even for small clusters. They can migrate at high temperatures, allowing clusters to nucleate. Radiation cascades can also nucleate vacancy clusters at their cores. Although in the case of $\alpha$-Fe the nucleated clusters tend to be dispersed vacancies

at second neighbour distance or more[45], instead of voids or vacancy dislocation loops. Some simulations[46] of high energy bombardments show collapse to vacancy loops, although the effect is still uncommon.

Models show that compact voids can form from the subsequent migration of the loose vacancy clusters[47]. For larger clusters single vacancies can be absorbed with energetic gains equivalent to the formation energy of the vacancy as the surface area of the void is relatively unaffected[14]. The formation and growth of voids leads to radiation swelling of the material[2]. This effect is due to the bias sink absorption of interstitials loops by dislocations as compared to absorption of voids. This results in an overall flow of vacancies into neutral sinks such as voids, while interstitials are preferentially incorporated into the dislocation network, swelling the material[2].

Bubbles are voids filled with a gas such as helium. Helium is present in the lattice through implantation and transmutation events in the presence of radiation sources such as fusion reactors. Expected concentrations of helium in fusion shielding is 2000 appm[5]. Studies suggest a formation of helium in cascades at a rate of 10 appm/dpa[3] for fusion conditions. Helium is self-trapping, attractive to vacancies and has a high diffusion rate in $\alpha$-iron[44, 9, 48]. This leads to bubble formation as the helium clusters in the voids to reduce the repulsion effects in the lattice. Bubble formation has been observed experimentally, for example Edmondson[7] observes bubble formation by transmission electron microscopy(TEM) and atomic probe tomography (APT) in nanostructured ferritic alloys. They observe helium bubbles to occur in bulk as well as at grain boundaries and dislocations.

Both voids[8] and bubbles[9] can pin dislocations leading to hardening of the material. The growth and dynamics of voids and bubbles can have macroscopic effects on the material such as hardening and swelling. This makes their study of particular importance in determining the lifetime of the material under irradiation.

## 4.2 Literature Review

A study of very low energy cascades of just a few eV impacting on voids has been performed by Dubinko[49]. It showed that very low doses can lead to the dissolution of voids by focusons striking them. Focusons transfer energy along closed packed planes without interstitial transport. Upon striking a void the atom at the terminus of the focuson may be injected into the void, leaving a vacancy at the initial starting point of the focuson. This is consistent with experimental observation[50] that the voids can be reduced in size by irradiation under favourable conditions.

At higher energy Pu[51] et al. studied stability of helium bubbles of different densities struck by radiation cascades. They find that the stability of the bubble depends on its He/vac ratio. Clusters with significantly more He than vacancies tend to absorb vacancies from the cascade. Conversely, clusters with a low density of He tend to lose vacancies during the cascade, approaching the stable ratio of near 1:1.

Simulations by Parfitt and Grimes[52] study the behaviour of helium bubbles in uranium dioxide under radiation induced cascades. An atom close to the bubble is given 10 keV of energy, to simulate a radiation event, and the resulting cascade observed. They find that where the hot 'melt' region of the cascade overlaps the bubble, there is an increased chance of helium gas being emitted into the region. As the melt region cools the helium is trapped in the lattice. Their study concludes that this emission is mostly not ballistic, but rather is due to the disorder of the bubble walls allowing low energy diffusion paths into the lattice. Some ballistic emission of gas is also observed at shorter time scales, although most of the gas remains confined to the bubble. They expect the mechanism of increased surface diffusion, due to the melt region, to be dominant for larger bubbles.

Further properties of helium in iron during cascades (but not in the presence of voids or bubbles) have been obtained by Lucas[53] et al. They find that the presence of substitutional helium tends to reduce the number of Frenkel pairs produced. Interstitial He increases lattice stress and favours the formation of self interstitial atoms (SIA) as well as stabilising SIA clusters. They observe increased

diffusion of helium at high temperature, which aids bubble formation.

An interesting mechanism for interstitial cluster formation during cascades in pure $\alpha$-Fe has been observed by Calder[54] et al. They find that some cascades emit particles moving faster then the cascade wave front, which cause secondary cascades ahead of the main one. Collision of the high density primary wave with the core of the secondary cascades can lead to nucleation sites for interstitial clusters. This effect is attributed to atoms being forcefully pushed into the secondary cascade's low density core region.

Under irradiation voids in iron can form lattices[55]. This effect has been reproduced by Heinisch[56] et al. in KMC simulations. Their study uses clusters of crowdions formed by irradiation and moving mostly one dimensionally along close-packed planes to explain the alignment. Voids off the lattice are exposed to a greater flux of crowdions and so tend to shrink, whereas voids on-lattice are shielding each other along the close packed planes. The simulations do produce a void lattice successfully although the lattice does not show the same refinement as experimentally observed.

## 4.3 Juslin Fe-He Potential

To model bubbles and other behaviour of helium in iron, an appropriate potential is required. The commonly used Wilson[57] Fe-He potential has erroneous energies for both the substitutional and interstitial energies of helium in an iron lattice. It also predicts the most stable interstitial site to be octahedral, while DFT predicts tetrahedral. Juslin's[58] paper addresses the problems with the Wilson Fe-He potential by deriving a new pair-wise potential. Seletskaia[59] previously developed Fe-He potential with pair and many body terms fitted to the Finnis-Sinclair Fe-Fe potential[15] but Juslin argues this is an unnecessary use of calculation as the same results can be obtained using a pair potential.

One issue with cross-potentials is that when fitting a choice of Fe-Fe potential must be made and any flaws in the Fe-Fe potential may end up being compensated for in the cross-potential. Juslin develops a potential based on the screened coulomb potential compatible with the Ackland-Mendelev[60] Fe-Fe potential,

the Seletskaia paper used the older Finnis-Sinclair potential for Fe-Fe.

For short distances DFT data obtained by modelling a Fe-He dimer is used to fit the potential. This part of the potential is only sampled in the high-energy early phase of the cascade. The main part of the potential is a screened coulomb potential with a cubic spline to the short range potential. The potential is smoothly truncated at long distance; its full form is given below:

$$f(r) = \begin{cases} DMOL - potential & r \leq r_1 \\ p_3 r^3 + p_2 r^2 + p_1 r + p_0 & r_1 \leq r \leq r_2 \\ (a + \frac{b}{r}) e^{-cr} f_c(r) & r \geq r_2 \end{cases} \tag{4.1}$$

The function $f_c(r)$ smoothly cuts the function off around the cut-off radius. The parameters of the potential (available in Juslin's paper[58]) were fitted by comparing relaxed DFT data to relaxed MD simulation. The parameters were fitted largely numerically although were tweaked by hand to emphasise certain features. The exact details of the Fe-Fe potential effect their simulation results, especially the stiffness of the Fe. Since most Fe-Fe potentials are fitted to the elasticity of iron this should not be a major issue, and their potential should work with other Fe-Fe potentials.

They test the potential along with the Ackland-Mendalev Fe-Fe potential. The tetrahedral helium interstitial site energy, 4.39 eV, is found to be more stable than the octahedral site, 4.51 eV, using this potential. These numbers closely match the Willaime[44] DFT results of 4.39 eV and 4.57 eV respectively. The tetrahedral diffusion energies are well reproduced by the potential. A study of the vacancy diffusion energy is conducted and compared to the Willaime data using the $HeV_2$ complex diffusion method. The potential reproduces the diffusion well, with the differences being small compared to the barrier heights. The only discrepancy is a flattening of one of the migration peaks by 0.4 eV, which will increase the vacancy migration rates. The study is repeated using the Dudarev[61] Fe-Fe potential and the Finnis-Sinclair potential. Similar results are obtained in both cases with the main discrepancy being a dip in the tetrahedral helium diffusion when combined with the Finnis-Sinclair potential. The barrier drops below the starting energies at the centre of the diffusion making the tetrahedral site unstable.

The Juslin potential provides a fairly reliable way of incorporating helium into iron MD simulations, especially when coupled with the Ackland-Medelev potential. It only has pair wise terms and so is quick to calculate. The diffusion rates for interstitials as well as their stabilities in different sites are well reproduced. Vacancy diffusion shows some discrepancies but the overall shape and height of the energy barrier is comparable to DFT.

## 4.4 Method

A study of the interaction of radiation cascades with voids and bubbles present in the system was conducted. Either a void or a bubble was placed at the centre of the system. A cascade was then started in the vicinity of the defect cluster and the interaction observed.

### 4.4.1 Forming Voids and Bubbles

This section explains the method used to produce stable voids and bubbles in the lattice. Starting with a BCC quenched iron lattice at T = 0K, a single atom was removed near the centre of the system. The system was again quenched and the atom with the highest potential energy removed. Iterating this process produces a stable void with faceted sides aligned to stable lattice directions. Stability was confirmed by running MD, with the sample at 900 K for 20 ps.

Bubbles were produced by placing helium atoms on to the vacant sites in the void. The system is then quenched using low temperature MD with a high thermostat value to limit the velocity of the helium atoms. Once the helium has reached a stable configuration the system may be thermally equilibrated with standard thermostating.

### 4.4.2 Cascade Centre and Volume

The code described in sec. 3.4 was used to estimate the radiation-cascade's centre and volume. Initially a list of particles that have changed nearest neighbour is

generated. This list of particles will contain atoms involved in replacement-collision chains as well as the core "melted" region caused by the cascade. Filtering the changed neighbour list further to only include members that have at least 3 neighbours that have also changed neighbour, eliminates detection of replacement-collision chains. This allows a reasonable estimate of the cascade melt volume to be made. The centre of mass of this list is taken as the centre of the cascade and the radius is estimated by assuming the volume is spherical.

### 4.4.3 Cascade Set-up

The molecular dynamics study used a version of MOLDY [62] modified for variable time step cascade simulations, as detailed in ch 2.2. The Ackland-Mendelev[60] embedded atom potential was used for Fe-Fe interactions. The Juslin pair potential[58] was used for Fe-He and the Beck[63] pair potential for He-He. The Beck He-He potential as well as the iron potential was splined to the ZBL[36] universal potential at short range. The Juslin potential did not require a spline as it already incorporates a strong repulsion at short distance.

Cascades were initiated by giving an iron atom, the pka, near to the defect cluster substantial kinetic energy at the beginning of the simulations. Cascade energies of 1, 2.5 and 5 keV were considered. For 1 and 2.5 keV cascades a box dimension of 40 $a_0^3$ (128 000 atoms) was used, with 65 $a_0^3$ (549 250 atoms) for 5 keV. The box used periodic boundaries and constant volume, with dimensions initially set to the equilibrated spacing of the lattice. An an NVE ensemble was used.

Cascades were mostly started with direction close to the 111 direction at a range of distances from the defect cluster. Simulations were typically at close to 0K but some studies at different angles and temperatures were also produced. The final defects production and clustering is analysed by the method explained in sec. 3.4.

## 4.5 Results

Simulations of a void or bubble interacting with a cascade in a periodic cubic box of $\alpha$-Fe were performed under various conditions. Most cascades were created using a pka initiated in the $\langle 111 \rangle$ direction towards the defect cluster, with a slight deviation to avoid perfect replacement-collision chains. This high symmetry direction was chosen in order to localise the cascade and give easily comparable data across different simulations.

To explore if the effects observed are dependant on the crystal alignment some cascades were also performed in the $\langle 311 \rangle$ direction and in random directions. Simulations were performed at 1, 2.5 and 5 keV on voids/bubbles of size 30 and 100, with the bubbles at ratio 1:1 for vacancy:helium. One set of data is also performed at 300 K to explore temperature effects. The various simulations along with their damage yields are summarised in table 4.1. More indepth results split by angle of impact and temperature are shown in tables 4.2 and 4.3.

The results do not depend strongly on direction: the angle has little effect on the cascade radius or the Frenkel pair production. Results along the $\langle 311 \rangle$ direction were found to be consistent with similar studies of the $\langle 111 \rangle$ direction. The radii and damage production of the cascades was also consistent across randomly launched trajectories. For 300 K simulations little change was seen in the results apart from a slight reduction of Frenkel pairs, and so further temperature studies were not pursued, although higher temperatures may have more effect. The radius of the cascade was observed to be similar across all runs at the same energy. The radius is similar for a void or a bubble present in the vicinity.

The cascades tend to reduce the void size slightly when overlapping it. This effect becomes more pronounced for larger voids or higher energies. Bubbles are much less effected and overall show a slight growth during bombardment. Almost all the helium remains confined in the bubble for the energies studied. The presence of a bubble increase the yield of Frenkel pairs slightly as compared with cascades in the presence of a void.

*Table 4.1*: *The Frenkel pair count, $N_f$, and cascade radius, $r_c$, for various simulations of bulk cascades in iron with Finnis-Sinclair type potentials. E is the* PKA *energy.*

| E (keV) | $r_c$ (Å) | type | $N_f$ |
|---|---|---|---|
| 1 | 7.3 | void | 5.5 |
| 1 | 7.2 | bubble | 6.2 |
| 2.5 | 10.8 | void | 11.2 |
| 5 | 15.1 | void | 16.7 |
| 5 | 15.3 | bubble | 19.1 |

### 4.5.1 Movement

Interestingly, some of the simulations show that the void is moved by several angstroms, even although there are not many extra vacancies formed in the lattice. The cascade displaces atoms around itself creating a density "wave" moving spherically outwards, with a depleted region at its core. Normally in a perfect lattice this "wave" will collapse back as the energy dissipates, cancelling with the depleted region at its core.

However, when in a suitable geometry with a pre-existing void, a more complex mechanism may take place. The density "wave" injects atoms into the pre-existing void, where they find sites to occupy and so do not return as the wave collapses back. This results in the original void being filled, and a new void of equal size stabilising at the cascade core. This process is equivalent to the diffusion of a void by several lattice spacings. This behaviour was reproducible for voids under all conditions considered, providing the cascade overlaps the void. Figure 4.1 shows the diffusion process.

Figures 4.2 & 4.3 show the distance to the pka starting position from the centre of the void against the distance moved by the centre of the void. It can be seen that the mechanism has a minimum and maximum radius. The cascade will typically centre a few lattice spacings from the starting position of the pka. At very short distances the pka can pass directly through the void, which is why there is a minimum interaction threshold for PKA distance. The maximum interaction distance is set by the cascade radius, as the cascade must envelop the void to fully interact. Data suggests interaction thresholds of 12 Å and 25 Å with peak

*Table 4.2: Table of cascade results in the presence of a void for bulk cascades in iron with Finnis-Sinclair type potentials. "Simulations" is the number of simulations performed for each configuration. E (keV) is the initial energy of the pka and "defect-size" is the initial size of the void. $N_f$ is the number of Frenkel pairs formed. $V_{void}$ is the number of vacancies in the void after the cascade. $r_c$ is the radius of the cascade. Set up describes the initial trajectory of the pka, T = 0 K unless otherwise stated. The values presented are averaged over the simulations.*

| E (keV) | set up | simulations | defect-size | $N_f$ | $V_{void}$ | $r_c$ (Å) |
|---|---|---|---|---|---|---|
| 1 | ⟨111⟩ | 17 | 30 | 5.3 | 28.8 | 7.1 |
| 1 | random | 48 | 30 | 5.8 | 29.8 | 7.2 |
| 1 | ⟨311⟩ | 10 | 30 | 5.9 | 29.6 | 7.5 |
| 1 | ⟨111⟩, T=300 K | 14 | 30 | 4.6 | 28.1 | 7.6 |
| 2.5 | ⟨111⟩ | 12 | 30 | 14.2 | 30.8 | 11.0 |
| 2.5 | random | 16 | 30 | 9.9 | 26.8 | 10.6 |
| 2.5 | ⟨111⟩ | 9 | 100 | 9.4 | 89.6 | 10.9 |
| 5 | ⟨111⟩ | 12 | 30 | 18.8 | 27.9 | 15.2 |
| 5 | ⟨111⟩ | 16 | 100 | 14.6 | 84.3 | 15.1 |

interactions around 18 Å at 1 keV (Fig. 4.2). For 2.5 keV the interaction starts at 18 Å goes until 40 Å and has peak at 31 Å. For 5 keV the interaction starts around 12 Å ends at 38 Å and has peak interaction at 31 Å (Fig. 4.3). However, these figures also include the travelled distance of the pka, as the starting position of the pka is not the centre of the cascade.

For 1 keV cascades on bubbles of size 30 almost no motion of the cluster is observed even for high cascade overlap. The slight movement seen (Fig. 4.2) is due to the side of the bubble nearest the cascade absorbing a few vacancies, shifting the centre of the cluster. On average the bubble grew by around one vacancy and almost all the helium remained clustered in it.

Similar results were observed for a 5 keV cascade impacting a bubble of size 100. Fig. 4.5.b shows a typical bubble after impact. The helium reduces the mobility of the cluster (Fig. 4.3) and the helium remains clustered in the bubble. Cascade radius is unaffected, although the number of Frenkel pairs formed seems to increase slightly (table 4.1). Occasional shrinkage by up to 5 vacancies is observed at longer distance due to interstitial absorption from the cascade periphery.

For a void of size 100 impacted at 5 keV significant movement of the void towards the cascade was observed (Fig. 4.3). Void size tended to decrease slightly on

*Table 4.3: Table of cascade results in the presence of a bubble for bulk cascades in iron with Finnis-Sinclair type potentials. "Simulations" is the number of simulations performed for each configuration. $E$ $(keV)$ is the initial energy of the pka. "He:vac bubble" is the initial helium and vacancy content of the bubble, the vacancy content is simply the number of missing iron atoms. $N_f$ is the number of Frenkel pairs formed. The final location of the helium is categorised as follows: $He_{bub}$ is the helium remaining in the bubble, $He_{sub}$ is substitutional in the lattice, and $He_{int}$ is interstitial in the lattice. $r_c$ is the radius of the cascade. $V_{bub}$ is the number of vacancies in the bubble after the cascade. Set up describes the initial trajectory of the pka, $T = 0$ $K$ for all runs. The values presented are averaged over the simulations.*

| E (keV) | set up | simulations | He:vac bubble | $N_f$ | $V_{bub}$ | $He_{bub}$ | $He_{sub}$ | $He_{int}$ | $r_c$ (Å) |
|---|---|---|---|---|---|---|---|---|---|
| 1 | ⟨111⟩ | 14 | 29:30 | 6.5 | 31.1 | 28.3 | 0.6 | 0.1 | 7.4 |
| 1 | random | 46 | 29:30 | 6.1 | 30.2 | 28.9 | 0.1 | 0 | 7.1 |
| 5 | ⟨111⟩ | 12 | 100:100 | 19.1 | 102.2 | 100 | 0 | 0 | 15.3 |

average to 84 vacancies. This change is partly due to the void being split by partial interactions as shown in Fig. 4.5.a, which occurred in 3 simulations. Ignoring the split samples, void size tends to be around 88 after cascade interaction.

The data for the 5 keV bombardment of a void is also represented in figure 4.4. The motion of the void is plotted against the distance between the initial void and the cascades centre of mass. The vectors are projected along the ⟨111⟩ direction, which is the initial launch direction of the pka. The void is seen to move towards the cascade centre. The negative values on the x-axis are a result of the pka moving through the void and starting a cascade on its far side. When the cascade significantly overlaps the void, strong interaction can be seen.

## 4.6 Conclusion

The MD shows that the presence of a bubble slightly increases the yield of interstitials. Bubbles are not strongly effected by cascades, with most of the helium remaining inside the bubble. Voids interact more strongly and tend to shrink slightly when on the periphery of a cascade.

A mechanism has been observed that can move voids by several lattice spacings when overlapped by a cascade. This mechanism operates by ballistically injecting atoms into the void, leaving a depleted region at the cascade core. The mechanism

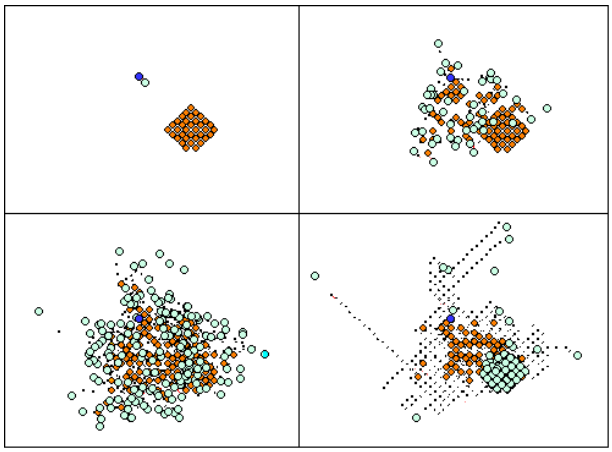

*Figure 4.1*: *The mechanism for cascade induced void movement is shown above for a 5 keV collision with a 100 vacancy void in iron with Finnis-Sinclair type potentials. The dark blue dot represents the starting positions of the cascades, orange dots are vacancies, light blue dots are interstitials or filled vacancies. Small black dots represent the atoms that have moved in the cascade. Non-defective atoms are omitted and the full box size is not shown. Top left: Void and* PKA *positions and* PKA *direction shown after 2 fs. Top right: Wave of displaced atoms starts to form and expand at 76 fs. Bottom left: Full extent of wave, encompasses the void, injecting atoms into its core at 260 fs. Bottom right: Wave collapses back, but atoms are trapped in void, leaving a depletion at cascade core by around 1 ps (image taken at 5 ps for clarity). Note that an initial vacancy filled with an atom is shown as interstitial here, when more conventionally it would be termed a normal site. This was done to clearly show the filling of the void with normal sites.*

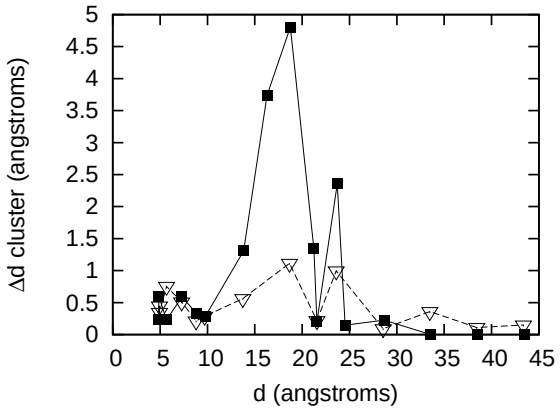


*Figure 4.2*: *Graph showing movement of void, $\Delta$ d cluster, (filled squares) and bubble (empty triangles) vs. distance to* PKA, *d, for a 30 defect cluster hit at 1 keV in iron with Finnis-Sinclair type potentials. It can be seen that the void can move significantly towards the* PKA *site for certain cascade distances. The presence of helium in the void greatly damps this effect.*

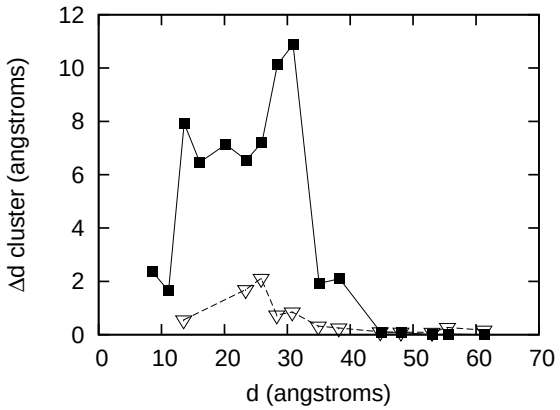


*Figure 4.3*: *Graph showing movement of void, $\Delta dcluster$, (filled squares) and bubble (empty triangles) vs. distance to* PKA, *d, for a 100 defect cluster hit at 5 keV in iron with Finnis-Sinclair type potentials. It can be seen that the void can move significantly towards the* PKA *site for certain cascade distances. The presence of helium in the void greatly damps this effect. The effect is much more pronounced than at 1 keV.*

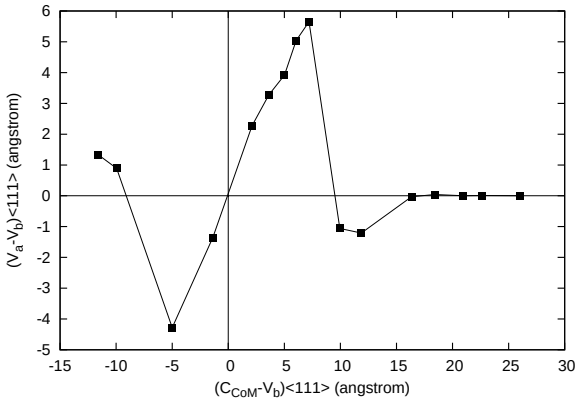


*Figure 4.4*: *Graph shows the movement of the void vs. the distance between the initial void and the cascade centre. The data is projected along the $\langle 111 \rangle$ vector, which is the initial vector of the pka. $v_a$ is the final void CoM, $v_b$ is the initial void CoM and, $C_{COM}$ is the cascade centre of mass. cascades are performed on a 100 vacancy-void using a 5 keV pka in iron with Finnis-Sinclair type potentials. All pka's start on the same side of the void, the negative values on the x-axis result from the pka travelling through the void and starting a cascade on the opposite side.*

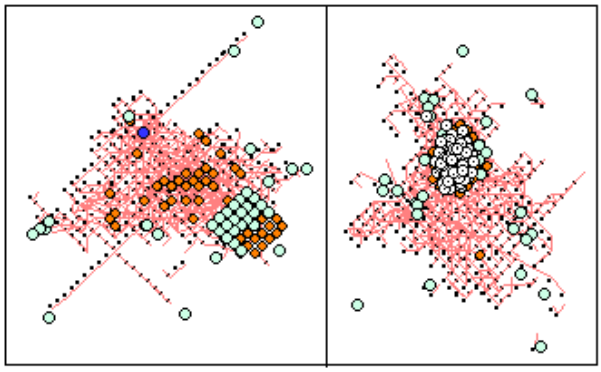

*Figure 4.5*: *a) (left): Cascade radius overlaps half the void leading to partial filling and splitting of the void. Half the void is unaffected, and now forms a smaller void. A second void is formed at the depleted cascade core, as several atoms from the cascade are now trapped in the near side of the old void, preventing their return. The shaded red region represents atoms that have been displaced by the cascade, and is related to the cascade radius. Other colours used are the same as in fig. 4.1. b) (right): Typical final state of a 5 keV cascade impacting 100 helium bubble in a 100 vacancy void in iron with Finnis-Sinclair type potentials. Helium remains clustered in the void.*

does not move bubbles as the gas prevents the injection of atoms. The interaction is thresholded by the cascade radius and so becomes more significant at higher energies. The initial direction of the pka does not effect the interaction. In the following section the motion of voids, due to the mechanism identified, is compared to the rate of cluster diffusion using an OKMC code.

## 4.7 OKMC Model

### 4.7.1 Overview of the Algorithm

An object kinetic Monte Carlo (OKMC) code was written to simulate the accumulation of radiation damage in iron, focusing on void mobility during the process. Such algorithms use probabilities of certain changes occurring in the system to evolve the system in time. Included in the simulation are radiation cascade events, point defects, and clusters of interstitials or vacancies. Defect clusters of opposite types can absorb or annihilate each other. Small clusters of both types are mobile during the simulation. Thermal dissociation events allow clusters to emit single defects. The code was implemented using object orientated Java programming, which fitted the structure of the simulation well. Although the code could have executed faster in Fortran or similar languages, Java was chosen for its readability and extendibility.

In standard kinetic Monte Carlo the system is modelled dynamically by looking at the transitions available in the system. The transitions may be assigned a probability of occurring at a certain temperature based on the Arrhenius' equation. An event is picked based on its relative probability to occur and is executed. Such a method is much faster than MD as the individual motion of atoms are (typically) not tracked, and only the defects are modelled. The transition in MD are linked to thermal oscillations overcoming potential barriers. In KMC it is equivalent to skipping all the failed attempts at barrier hopping and directly evolving the system to the next successful transition.

In object kinetic Monte Carlo conglomerates of defects are treated as single objects. These objects are treated similar to the single defects, but with their own transition rates. These rates represent the correlated motion of many defects,

which in some cases would not be possible to model with single defect transition rates. Additionally this method is far more efficient than standard KMC as fewer defects need to be considered.

The well known algorithm used for (object) kinetic Monte Carlo given below:

1) List all transitions available to the system, along with the rate for each. Rates are typically given as $r_i = e^{-\beta E_b}/\tau$, where $\tau$ is the oscillation period of the atoms. $\tau$ was set to 155 fs. $E_b$ is the energy barrier for the transition and $\beta = 1/kT$

2) Calculate the cumulative rates: $R_i = \sum_{j=1}^{i} r_j$ for i equals 1 to N. N is the number of possible events in the system and $R_N$ is the total cumulative rate.

3) Pick a transition to perform with probability equal to $r_i/R_N$. This can be achieved efficiently by picking a random number p = (0,1] and then finding the cumulative rate that satisfies $R_{i-1} < pR_N \leq R_i$.

4) perform event i.

5) update the time by $\Delta t$ where $\Delta t = R_N^{-1} \ln(s^{-1})$ where s is a random number s = (0,1]

6) repeat from step 1.

Boundary conditions for periodic systems, open systems and a system with a surface in one direction were implemented.

The various factors considered in this code are detailed in the following sections.

### 4.7.2 Barriers

The energetic barriers were taken from Bjorkas[64] and are listed in table 4.4. Most of the values used in table 4.4 come from Fu[47]. In this model vacancy/interstitial clusters larger than 4 defects are considered immobile. This assumption is partly validated in the Fu[47] paper as their simulations match experimental data, reproducing resistivity recovery measurements.

The barriers for interstitial cluster diffusion can be seen to increase with size. It

is also of note that $V_3$ has lower migration barrier than $V_2$ or $V_1$. The various pathways for such migrations are explored in Fu's paper.

*Table 4.4: Model parameters: Table of migration energy, $E_m$, and dissociation energy, $E_d$, of point defects from clusters. $E_d^n = E_m^1 + E_b^n$: the dissociation energy for cluster size n, is the point defect migration energy, $E_m^1$, plus the cluster binding energy for a cluster of size n, $E_b^n$. Binding energy is defined as the energy to remove one defect from the cluster. $E_{b2}$ is the binding energy of a cluster with two defects, $E_{b2}^V = 0.30$ and $E_{b2}^I = 0.80$ eV. Formation energies: $E_f^V = 2.07$ and $E_f^I = 3.77$ eV. All diffusion is 3D. $g(n) = \frac{n^{2/3}-(n-1)^{2/3}}{2^{2/3}-1}$ [64]*

| Type | $E_m$ (eV) | $E_d$ (eV) |
|---|---|---|
| $V$ | 0.67 | |
| $V_2$ | 0.62 | 0.97 |
| $V_3$ | 0.35 | 1.04 |
| $V_4$ | 0.48 | 1.29 |
| $V_n, n > 4$ | immobile | $E_m^{n=1} + E_f^V + (E_{b2}^V - E_f^V)g(n)$ |
| $I$ | 0.34 | |
| $I_2$ | 0.42 | 1.14 |
| $I_3$ | 0.43 | 1.26 |
| $I_4$ | 0.43 | 1.26 |
| $I_n, n > 4$ | immobile | $E_m^{n=1} + E_f^I + (E_{b2}^I - E_f^I)g(n)$ |

### 4.7.3 Dissociations

Dissociation of single point defects from clusters was allowed in the simulation. The rate of dissociation for a given cluster was multiplied by the size of the cluster to represent the multiple possible events. The rate of such diffusion can be estimated by[65]:

$$E_d = E_m + E_f + (E_{b2} - E_f)\frac{N^{2/3} - (N-1)^{2/3}}{N^{2/3} - 1}$$

Where $E_d$ is the energy barrier for a single point defect to dissociate from a cluster. $E_m$ is the migration energy of a single defect of the type considered. The dissociation energy is the point defect migration energy plus the cluster binding energy. $E_{b2}$ is the binding energy of a cluster of two defects. Binding energy is

defined as the energy to remove one defect from the cluster. $E_f$ is the formation energy of a point defect in a perfect lattice. N is the size of the cluster.

This formula was used for clusters of 5 or bigger, smaller clusters used pre-set values taken from Fu[47]. Dissociation events move the centre of mass of the cluster away from the new point defect. Dissociation is assumed to be isotropic.

The model approximates clusters as spherical when considering interaction distances and dissociation events. While this is a reasonable approximation for voids it would be more accurate to treat interstitial clusters as a disc. The dissociation rates go with the number of defects in the cluster. More realistic would be to only allow dissociation from surface vacancies on the spherical voids and circumference defects on the interstitial discs. The current approximation was made for simplicity of modelling.

### 4.7.4 Interactions

If a defect diffuses to within a certain distance of another, the defects are combined or annihilated based on their types and sizes. To be explicit, like clusters may absorb each other and opposing clusters (i.e. an interstitial cluster meeting a vacancy cluster) can annihilate each other. For absorption the size of the largest cluster is increased by the smaller cluster. The centre of mass of the coalesced cluster is updated to reflect that the matter will mostly connect to the side nearest to the point of coalescence. For incomplete annihilation events the remaining cluster is moved away from the point of collision, as defects will be predominantly annihilated on one side of the cluster.

In each case, the small cluster is moved along the vector connecting the centre of masses until its CoM rests on the surface of the large cluster. A size weighted average of the clusters positions is then taken, and the large cluster is moved towards/away from the impact site in the case of absorption/annihilation. The small cluster object is then removed from the simulation. The displacement vector for the large cluster is given by:

$$\Delta x = \hat{r}_{ab} r_a \frac{n_b}{n_a + n_b}$$

Where 'a' is the larger cluster, $\hat{r}_{ab}$ is the unit vector joining the centre of masses, r is the particle radius and n is the particle size. These update rules allow the clusters with $n > 4$ to still move in the simulation by absorbing or annihilating defects. The clusters are also moved by dissociation of point defects from the cluster.

The capture radii of clusters follows the model in the Ortiz[65] et. al. study:

$$r_{I_n,V_n} = Z_{I_n,V_n} \left( \left( \frac{3n\Omega}{4\pi} \right)^{1/3} + r_0 \right)$$

Where $r_{I_n,V_n}$ are the capture radius for interstitial and vacancy clusters respectively. n is the number of defects in the cluster. $Z_I = 1.15$ is the bias factor accounting for the increased strain field observed for interstitials. $\Omega$ is the atomic volume and $r_0 = 3.3$ Å.

### 4.7.5 Optimisations

A large efficiency gain on this algorithm can be made by only updating the event list (step 1 of algorithm in sec. 4.7.1) when needed. In general if a particle diffuses without interacting with a cluster, the event list is unchanged. Additionally, if a particle does interact only a small part of the event list and cumulative rates must be recalculated: those events to do with the current cluster and the cluster it interacts with.

After moving a particle it must be checked to find whether it is within a certain interaction distance of other clusters. This is an $\mathcal{O}(N^2)$ operation, where N is the number of objects in the system. This could be made more efficient by using a spatial link cell scheme. That is, breaking the system into spatial domains and assigning each object to the domain that it is currently in. Now to check for close objects you need only check your current domain and the surrounding domains instead of the whole system, an $\mathcal{O}(N)$ operation. However, the full check was not

deemed computationally expensive enough to justify implementing this approach. For larger system sizes this would start to become important. Distance squared was compared to the threshold values squared to save performing expensive square root operations when checking closeness to other clusters.

Dissociation events are treated as only one event per cluster, with the rate multiplied by the cluster size. When performing an event a random direction is picked for the particle to dissociate in. This is more efficient than generating an event per defect in the cluster.

### 4.7.6 Cascades

Cascades were introduced into the system with a rate calculated from the chosen dpa per second. This was calculated as:

$$cascades[s^{-1}\text{Å}^{-3}] = \frac{Ndpas^{-1}}{10EV}$$

That is, the number of cascades per second per cubic angstrom is related to N, the number of atoms, $dpas^{-1}$ the displacements per atom per second, E, the energy in keV, and V, the volume in angstroms. This follows from an estimate of the number of displacements per cascade in Was[66], estimated as 10E, where E is the cascade energy in keV.

Cascades are introduced into the system at the above rate, by picking a random point in space at which the cascades will occur. The radius of the cascade is estimated as a function of energy:

$$r = \sqrt{0.044E + 8.9}$$

where E is cascade energy in eV and r is in Å.

The yield per cascade is estimated from:

$$N = 5.67(E)^{0.779}$$

Where N is the number of Frenkel pairs formed and E is the cascade energy in

keV. These empirical formulas are based on the results of MD simulations at 1, 2.5 and 5 keV.

An even number of interstitial and vacancy point defects are introduced into the system inside of the cascade radius. Final MD defect configurations tend to have a vacancy rich core surrounded by interstitials. To represent this the vacancies were placed randomly in a region up to half the cascade radius. Interstitials were randomly placed in the outer region. Since several of the defects placed will be within interaction radius of each other, they rapidly interact, forming stable interstitial clusters and a void core.

### 4.7.7 Void-Cascade Interaction

A new mechanism was added to the model based on the results of the molecular dynamics study (sec. 4.5.1). If the cascade volume overlaps with a void, the void is moved to the centre of the cascade. The void is not changed in size and no new point defects are added to the system. This represents atoms being forced into the void and creating a new void at the cascade core as observed in MD. This allows ballistic motion of the voids, which when considered over long time scales and many interactions can be thought of as a diffusion mechanism.

### 4.7.8 Diffusion

From the average displacement of a cluster and time between displacements the diffusion can be estimated as:

$$D = \frac{1}{6} \left(\bar{x}\right)^2 \bar{\Gamma}$$

Where $\bar{x}$ is the average distance moved and $\bar{\Gamma}$ is the average number of jumps per unit time. Separate data can be kept for the displacements due to different types of event. This allows separate diffusion rates to be associated with the different factors that displace the clusters in the system.

## 4.8 OKMC Results

### 4.8.1 Input Parameters

The Simulation takes several input values: the dimensions of the sample, temperature, cascade energy, dpa rate, and the boundary conditions. Initial defect clusters may also be added.

Studies were performed with the following default values: Temperature of 500 K, dpa/s of $1x10^{-6}$, cubic cell of 100 Å and cascade energy of 10 keV on a void of 100 vacancies. Periodic boundaries were typically used.

### 4.8.2 Analysis

The standard set up for the simulations was a void of 100 vacancies at the centre of an initially clean sample with periodic boundaries. Cascades are introduced into the sample and the defects allowed to diffuse and interact. The diffusion of the central void due to various factors is tracked. The diffusion caused by the absorption and emission of defects will be referred to as standard diffusion. The other diffusion mechanism is due to the ballistic motion of the void during cascades.

Simulations were repeated with the void-cascade interaction mechanism enabled and disabled. Simulations are also repeated with either periodic boundaries or absorbing boundaries. Periodic boundaries represent an infinite lattice of voids. The absorbing boundaries could be thought of as representing the presence of other defect sinks at a certain radius from the void, such as grain boundaries or dislocations.

All results are averaged over ten runs. The effects of varying the input parameters are considered in the following sections.

### 4.8.3 Box Dimensions

Fig. 4.6 shows the effects of the system volume on the diffusion rate with absorbing boundaries in place. Fig. 4.6 [left] shows the diffusion, with no void-cascade interaction implemented, is strongly dependent on the system volume. For random walking point defects the capture area of the central void can be approximated as half the distance from the void surface to the edge of the system. Increasing the system size increases the capture volume of the void, and so the number of defects impacting it. Since interstitials are more mobile than vacancies, this leads to a shrinkage of the void by impacting point defects. Due to this, the mobility of the void increases as its centre of mass can be shifted more easily.

Fig. 4.6 [right] shows that the void-cascade induced diffusion also has a dependence on system size, although this effect saturates faster than for the standard case. Void shrinkage is observed as the volume is increased. Since the void-cascade interaction is geometrically based, a smaller void is more likely to be encompassed in the cascade and so interacts more, increasing the diffusion.

Fig. 4.7 is similar to fig. 4.6 but with periodic boundaries instead of absorbing boundaries. Fig. 4.7 [left] suggests a trend of increasing diffusion with system dimension. The effect is less pronounced than with the absorbing boundaries as the increase is 2 fold over the range considered instead of 18 fold. Changing the system size in a periodic lattice is equivalent to changing the spacing in the void lattice. This changes the amount of long and short range diffusing particles that impact the void. For the smallest system, almost all cascades make defects in close vicinity to the void. For larger systems long range diffusion takes place changing the dynamics of the system.

Fig. 4.7 [right] shows very little trend for the void-cascade induced diffusion. Any variance in points is well within error. The size of the void is much less affected by small system dimensions for periodic boundaries than for absorbing boundaries. The vacancy enrichment seen with the absorbing boundaries is no longer an issue.

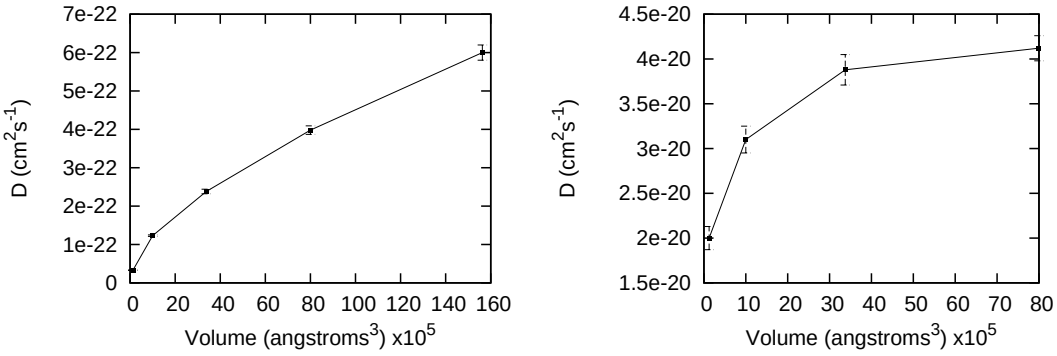


*Figure 4.6*: *Simulations with absorbing cell walls. [left] Diffusion constant vs. system volume with no void-cascade interaction. [right] Diffusion constant vs. system volume with void-cascade interaction*

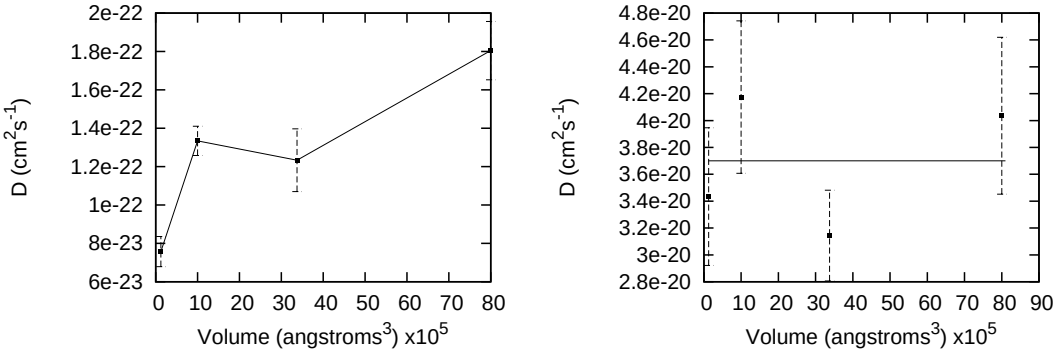


*Figure 4.7*: *Simulations with periodic boundaries. [left] Diffusion constant vs. system volume with no void-cascade interaction. [right] Diffusion constant vs. system volume with void-cascade interaction*

### 4.8.4 Cascade Energy

The effects of cascade energy on diffusion of the void is studied. Since the dpa rate is fixed, increasing the cascade energy results in a decrease in the frequency of the cascades. Fig. 4.8 shows the effects of energy with absorbing boundaries. Fig. 4.8 [left] shows that without the cascade-void interaction, increasing energy of cascade decreases the diffusion. Small cascades produce smaller clusters that are more likely to be mobile, when compared to the large clusters formed in higher energy cascades. Having several small cascades gives more free defects in the system than one large cascade, for an equivelent amount of dpa. This leads to more impacts of defects on the void, increasing diffusion for lower energies.

Fig. 4.8 [right] shows diffusion when the void-cascade interaction is allowed. Diffusion is increased by cascade energy. The two factors that affect diffusion here are the frequency of interaction with the central void and the distance moved when an interaction occurs. Increasing cascade energy increases the cascade radius, and so the average distance moved in an interaction is increased. It also increases the chance of interaction, as overlap with the void is more likely. These effects outweigh the decrease in frequency of cascades with energy.

Fig. 4.9 shows the effects of varying energy on a system with periodic boundaries. The trends are similar to the absorbing case, although the rate of standard diffusion is a bit higher due to there being more free defects in the system, as the walls do not absorb them.

### 4.8.5 Temperature

The effect of temperature on the diffusion of the void is studied. Fig. 4.10 shows the effects of temperature with absorbing boundaries. Fig. 4.10 [left] shows that without the cascade-void interaction, increasing temperature increases diffusion. This is due to greater mobility of small defect clusters, increasing the number of interactions with the void. Fig. 4.10 [right] shows that with cascade-void interaction accounted for, there is actually a decrease in diffusion at higher temperature. This decrease is due to growth of the void at higher temperature, as vacancy clusters in the vacancy-enriched sample become mobile.

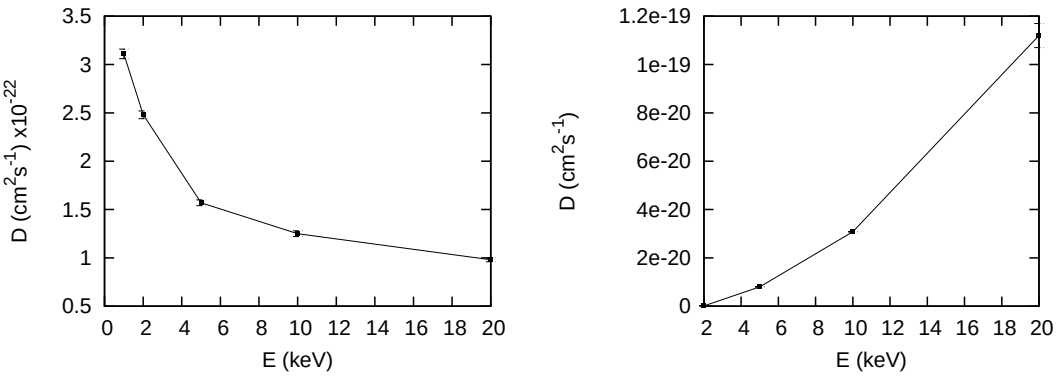


*Figure 4.8*: *Simulations with absorbing cell walls. [left] Diffusion constant vs. energy of pka with no void-cascade interaction. [right] Diffusion constant vs. energy of pka with void-cascade interaction*

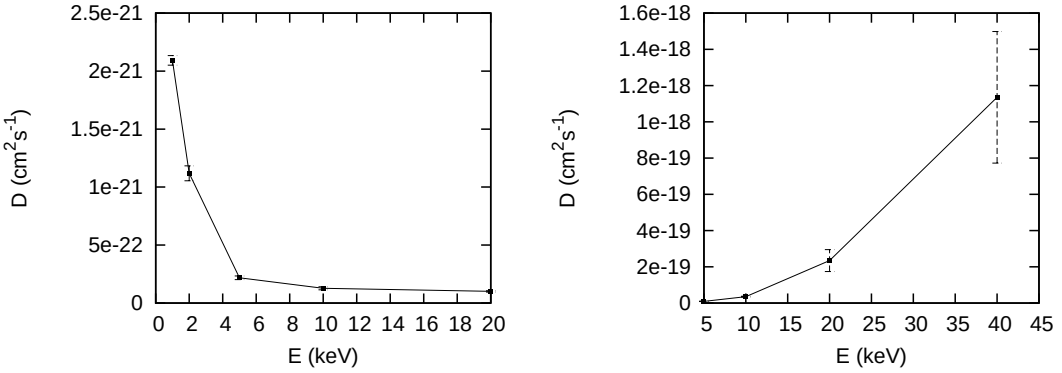


*Figure 4.9*: *Simulations with periodic boundaries. [left] Diffusion constant vs. energy of pka with no void-cascade interaction. [right] Diffusion constant vs. energy of pka with void-cascade interaction*

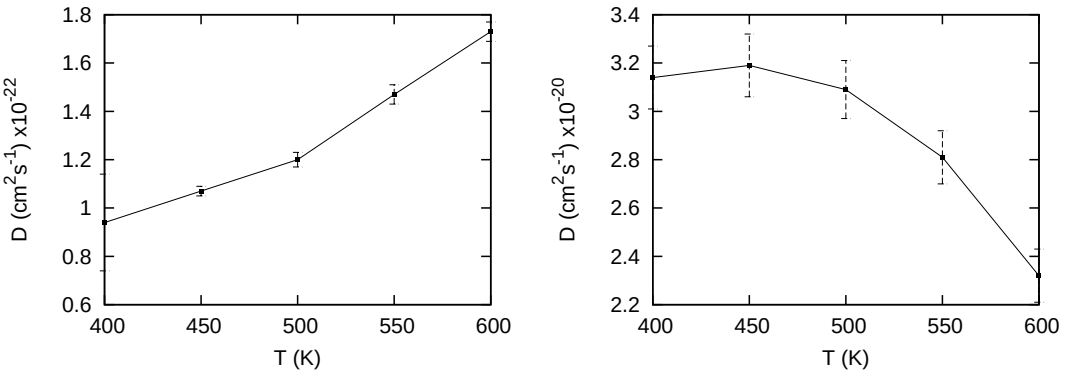


*Figure 4.10*: *Simulations with absorbing cell walls. [left] Diffusion constant vs. temperature with no void-cascade interaction. [right] Diffusion constant vs. temperature with void-cascade interaction*

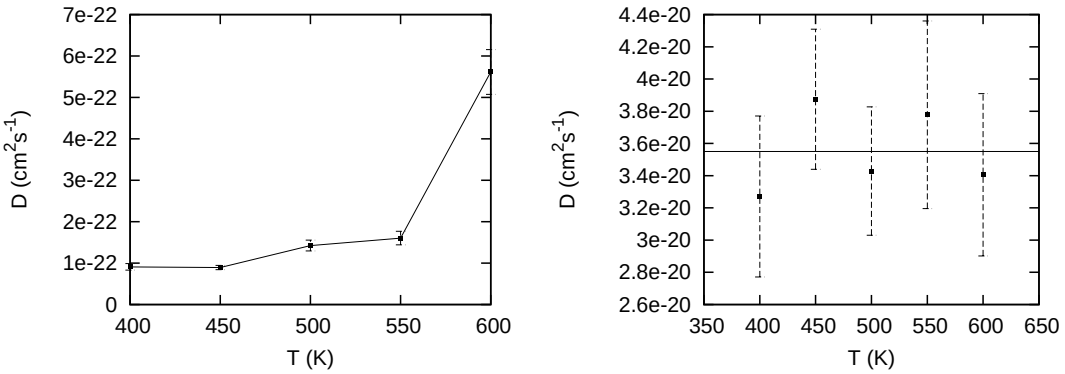


*Figure 4.11*: *Simulations with periodic boundaries. [left] Diffusion constant vs. temperature with no void-cascade interaction. [right] Diffusion constant vs. temperature with void-cascade interaction*

Fig. 4.11 shows the effects of temperature with periodic boundaries. Fig. 4.11 [left] shows that without the cascade-void interaction, increasing temperature increases diffusion as in the absorbing boundary case. Fig. 4.11 [right] shows that the cascade-void interaction is not temperature dependant when periodic boundaries are present.

### 4.8.6 DPA

Fig. 4.12 Shows the effects of varying dpa/s on the diffusion of the void, [left] is with absorbing boundaries, [right] is with periodic boundaries. The diffusion increases linearly with dpa/s. The increase is similar for both types of boundary conditions. Since dpa/s effects both the diffusion rates equally, it is not influential

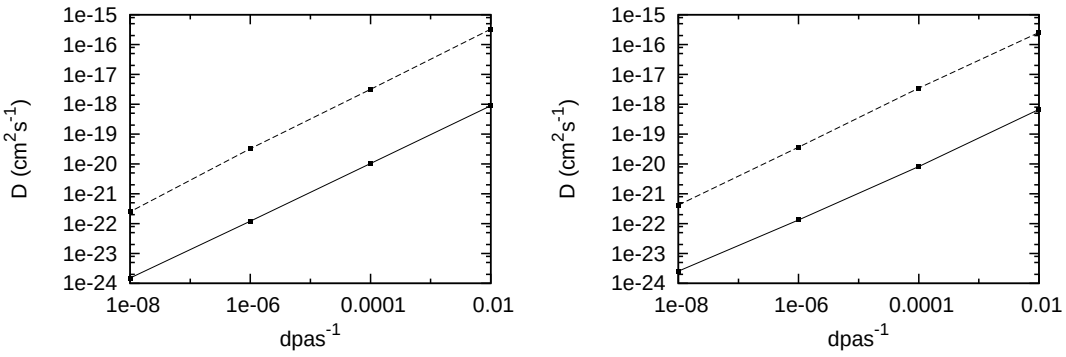


*Figure 4.12*: *Log-Log plot of Diffusion constant vs. dpa/s with void-cascade-interaction (dotted line) and without (solid line) [Left] With absorbing boundaries [Right] With periodic boundaries*

in defining which rate will dominate. The cascade debris has mostly equilibrated by the time the next cascade is introduced even for high dpa rates, and so rescaling dpa/s has no effect other than to linearly change the time between interactions.

## 4.9 Conclusions

The interaction of cascades with voids and bubbles has been studied in MD simulations. For overlap of the cascade with a void, the void is observed to be moved by a ballistic insertion of atoms into the original void. This leaves a new void at the cascade core. The presence of helium in the void is shown to suppress this mechanism by resisting the insertion of matter.

The mechanism was implemented in an OKMC code to compare it to diffusive rates in the system. The main mechanism compared to was the motion of voids due to absorption and emission of point defects or defect clusters. The ballistic motion of the void due to interaction with the cascade is shown to be greater than the other diffusive mechanism across most parameters. The exception to this is for energies below around 2.5 keV which is too low for significant cascade overlap with the voids, and the ballistic mechanism ceases to act.

# Chapter 5

# Alloy of Transition Metals in Iron

## 5.1 Introduction

This chapter studies a set of potentials for multi-component transition metal alloys with iron as the dominant element. Useful steels contain many elements, with the ratio of components strongly affecting the properties of the material. The structure of the material can undergo significant changes under irradiation, such as various precipitation behaviours which can lead to embrittlement[67, 1]. Fluxes of radiation induced defects in the system induce radiation induced segregation (RIS)[12], locally changing the concentration of elements in the alloy. Having a set of potentials that can model such complex behaviours is critical to progressing the simulation of multi-component steels. Although a set of potentials that models the exact properties of all the elements involved would be of great use, this is hard to achieve.

It is also of use to have a range of well understood potentials that are known to exhibit certain properties. This study focuses on a set of rescaled iron potentials[68] that has been fitted to the properties of transition metals. Although the potentials don't produce all the interaction of these elements correctly, there is still merit in studying the range of phenomena that can arise from such models. Such a set of potentials allows a wide range of phenomena to be explored.

This study focuses on identifying the properties of the potentials and their interaction with other elements in an iron lattice. Additionally studies of changing alloy concentrations are carried out, which can model changes in concentration due to diffusion or RIS. The interaction of multi-component alloys with voids in the system is also studied.

## 5.2 Literature Review

The modelling of transition metal alloys has been approached by many simulation methods using several different types of potentials. Some of these approaches are discussed below. DFT studies of transition metals produce results that compare favourably to experiment[69, 70, 71]. However, DFT is prohibitively expensive for large systems. This leads to a series of approximation schemes which attempt to capture the essential physics, while reducing the computational cost.

Tight binding models of transition metals have been developed as an attempt to improve on the run time of DFT calculations. McEniry et al.[72] develop a set of potentials for transition metal alloys of Fe, Cr and Mn. This method still explicitly treats the electrons in the system, unlike in empirical potentials. A reduced basis set is used for speed: only one basis function per angular momentum component is used. Although no ideal basis set is possible for all structures of an element, an optimal set can be found for a given structure. Using the minimal basis, it is possible to simulate the properties of the pure elements as well as their binary alloys. The technique, while more accurate, is significantly slower than using empirical potentials.

Marville et al.[73] applies Finnis-Sinclair type potentials to Mo, Ta and W in order to study metallic cluster properties. They successfully reproduce structural properties of bulk crystals, surface geometries, and the expected contraction of the surface layers, showing the effectiveness of Finnis-Sinclair type potentials on these systems.

Cox et al.[74] models surfaces of Cu, Ag and Au using Murrell-Mottram[75] potentials truncated at 3 body interactions. They focus on modelling the various plane surfaces of each crystal, successfully reproducing the changes in lattice

spacing. The type of potential used is slower than EAM as it scales with $N^3$, instead of $N^2$. However this potential can work well for Monte Carlo or Metropolis calculations, as only the energy of the moved atom must be recalculated. For EAM potentials the multi-atom density term means many atomic energies need to be recalculated every time an atom is moved.

Genetic algorithm[76] techniques have been used to locate the global structural minima for small clusters using Morse pair-potentials. The technique is based on generating candidate structures followed by combination and mutation of successful structures to find the minimum energy solution. This technique has also been successfully applied to the optimisation of Cu-Au clusters[77] using Gupta empirical potentials[78].

Cheng et al.[79] perform Monte Carlo simulations of Ag-Cu-Au clusters using using Gupta empirical potentials[78], which are based on the tight-binding model second-moment approximation (TB-SMA). They find segregation of the Cu to the core of the cluster, while Ag moves to the surface. Gupta potentials have been applied to other multi-component cluster simulations, such as a study[80] of Ag-Pd and Ag-Cu clusters.

## 5.3 Method

### 5.3.1 Rescaled Finnis-Sinclair Potentials

This section contains a brief description of the assumption that EAM is based on followed by an explanation of the rescaling algorithm used. The cohesion energy in metals is linked to the d-band density of states (DoS)[78]. Several properties of the system are only sensitive to the mean and width of the density of states, and not its exact details[81]. Based on this, cohesion models have been developed using the band width. The mean will tend to zero for pure systems. The bandwidth is related to the square root of the second moment of the DoS[82]. The band is approximated as rectangular, with centre $\mu_1$ and width $\sqrt{\mu_2}$, in both the Finnis-Sinclair and EAM type potentials, where $\mu$ are the moments of the DoS. The $k^{th}$ moment of the density of states is related to all possible closed

paths of k steps, which in turn is related to the hopping integrals of the tight binding model[83].

The embedded atom method (EAM) is often used as a basis for empirical potentials in MD simulations. A set of EAM potentials for modelling iron and its interaction with dilute transition metals is discussed below. Potential energy in the EAM model is given by[16]:

$$U(r_{ab}) = \sum_{a,a>b} V^{X_a,X_b}(r_{ab}) + \sum_a F^{X_a}(\rho_a)$$

$$\rho_a = \sum_{b \neq a} \phi^{X_a,X_b}(r_{ab})$$

where a and b are atoms, $X_i$ is the species of atom i, V is the species dependant pair potential, and F is the species dependent embedding function. $\rho$ represents the local electronic density and is the sum of a pair-wise function $\phi$, which is species dependant. The functional form of $F(\rho)$ is taken as $-\sqrt{(}\rho)$ in Finnis-Sinclair type models.

The iron interactions were modelled using the Ackland iron potential[84]. The other transition metals were modelled by the Hepburn[68] rescaled iron potentials. This set of potentials is designed for dilute concentration of transition metals in iron, and provides potentials for atomic numbers 22-29, 40-47 and 72-79, which gives 23 non-iron elements (listed in table 5.3.1). The non-iron transition metals will be referred to as the alloying element.

The rescaling is done as follows:

$$V^{Fe,X}(p_1^X r) = p_2^X V^{Fe,Fe}(r)$$

$$\phi^{Fe,X}(p_3^X r) = p_4^X \phi^{Fe,Fe}(r)$$

Where the various p's are species dependant empirical rescaling parameters.

Hepburn supplies potentials for Fe-X where X is an alloying element, as well as

potentials for X-X alloy-alloy interactions. For this study additional potentials for inter-alloy interaction were needed. The pair potential between alloy X and Y was estimated as:

$$V_{XY} = \frac{1}{2}\left(V_{XX} + V_{YY}\right)$$

and the density based term as:

$$\phi_{XY} = \sqrt{\phi_{XX}\phi_{YY}}$$

Which follows a common approximation scheme for cross-potentials used in the literature[85, 86, 87].

*Table 5.1: Elements studied with period and group numbered.*

| group | 4 | 5 | 6 | 7 | 8 | 9 | 10 | 11 |
|---|---|---|---|---|---|---|---|---|
| period 4 | $Ti^{22}$ | $V^{23}$ | $Cr^{24}$ | $Mn^{25}$ | $Fe^{26}$ | $Co^{27}$ | $Ni^{28}$ | $Cu^{29}$ |
| period 5 | $Zr^{40}$ | $Nb^{41}$ | $Mo^{42}$ | $Tc^{43}$ | $Ru^{44}$ | $Rh^{45}$ | $Pd^{46}$ | $Ag^{47}$ |
| period 6 | $Hf^{72}$ | $Ta^{73}$ | $W^{74}$ | $Re^{75}$ | $Os^{76}$ | $Ir^{77}$ | $Pt^{78}$ | $Au^{79}$ |

### 5.3.2 Standard Metropolis Algorithm

The Metropolis algorithm was implemented to find arrangement of atoms that minimises the Gibbs energy of the system. Below is the standard implementation of the metropolis Monte Carlo method with varying atomic types[88]. In this implementation the total number of particles, the temperature and pressure are fixed. The details of the standard algorithm are as follows:

i) Displacement of the atoms. Every atom is displaced by a small random vector, whose magnitude is less than a chosen threshold. For small displacement thresholds there is a greater probability to accept the new configuration, although the number of iterations needed to relax the system increases. The value of the displacement threshold must be picked carefully for efficiency of the algorithm. The configuration is accepted with probability:

$$P_{accept} = P_{new}/P_{old} = e^{-\beta\Delta U}$$

Where $\Delta U$ is the potential energy difference. If the probability ratio is greater than one (i.e. the energy decreases) then the transition is always accepted, as with all rates in this model.

ii) The type of a single atom in the box is changed with probability:

$$P_{accept} = P_{new}/P_{old} = e^{-\beta(\Delta U - \Delta\mu)}$$

where $\Delta\mu$ is the chemical potential difference between the two atomic types.

iii) Two atoms of different types are spatially switched. The acceptance criteria is identical to that in step i).

iv) The box dimensions are changed and accepted with probability:

$$P_{accept} = e^{-\beta(\Delta U + P\Delta V - NkT\Delta lnV)}$$

Iterating these steps will converge the system towards a local minima in the Gibbs energy. The global minima can be located by converging the systems energy from different starting configurations.

### 5.3.3 Metropolis-MD Algorithm

For this study a hybrid Metropolis-MD algorithm was used, with the equilibration process performed by MD. Details of the algorithm are given below. Initially the system is allowed to equilibrate for 40 ps to a given temperature using the Nosé-Hoover thermostat.

i) The system is relaxed using MD in the NPT ensemble for 100 fs. Atomic positions fluctuate locally and the box dimensions are allowed to relax to maintain the correct pressure (0 GPa).

ii) A pair of atoms, of different species, are randomly chosen and interchanged. If the energy decreases the change is kept. If the energy increases it is kept with

probability $e^{-\beta\Delta E}$, where $\Delta E$ is the potential energy difference between the final and initial states.

iii) (optional) An atom is chosen at random and its species is changed to another allowed species. The acceptance criteria is the same as step ii). In this step the energy after the change is adjusted, before comparing to the previous energy, to take into account the energy bias towards a certain species. The adjustment is by the difference in energy of an iron lattices containing one of the original element, $E_X$, subtracted from the energy of a pure iron lattice containing one of the new element, $E_Y$, with both systems equilibrated at 0 K. This removes bias towards any particular atomic type for isolated defects at equilibrium, leaving only the desired elemental bias that arises from stresses or interactions between different impurities. The energy can then be further adjusted by a chemical potential $\mu$ in order to favour a certain element.

$$\Delta E \rightarrow \Delta E - E_Y + E_X$$

iv) The cycle is repeated from stage i.

Equilibration was detected in terms of the slope of the averaged energy graph. The energy was recorded every 1000 MD steps and then averaged every 40 samples. Equilibrium required that the last 3 points output were within a temperature dependent threshold (calculated from the fluctuations in potential energy at equilibrium). This graph will flatten when the transitions are between near-equal energy states, or when the transition rate becomes very slow.

For runs at 0 K an extra equilibration step is added before measuring the energy in step ii. After the switch the atoms may relax for 100 fs before the energy is measured. This helps reduce the lattice stress from the switch, leading to a higher accept rate.

To verify compatibility of this equilibration approach with the standard metropolis algorithm the fluctuations in system energy are explored. A relaxed system of atoms is equilibrated to a given temperature using MD. The distribution of potential energies as the system fluctuates is recorded, using either standard MD or metropolis events (stage ii of standard metropolis algorithm) to evolve the system. Fig. 5.1 Shows the energy distribution of both methods to be similar

Gaussian distributions.

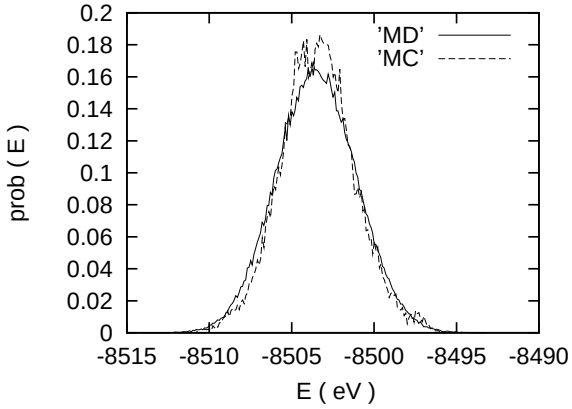


*Figure 5.1*: *Comparison of energies explored by Monte Carlo and molecular dynamics techniques at equilibrium, for an iron system with Finnis-Sinclair potentials. The distributions are similar.*

### 5.3.4 Clustering

The final configurations of the iron lattice containing various alloying elements was primarily analysed in terms of clustering. Clustering was defined by the abundance of like alloy atoms at a certain neighbour separation from each other. Cross-alloy attractions were calculated by the abundance of element X at a given neighbour separation from Y. When normalised by the number of atoms of a given type in the system this gives a number, f, between 0 and 1 that represents the self or cross-correlation of the alloy. For alloys types X and Y, the correlation at c nearest neighbour distance is defined by:

$$f_c^{XY} = \frac{1}{N_X N_c} \left( \sum_{i=\{X\}} \sum_{j=\{nc\}} \delta(X, T_j) \right)$$

Where T is the type of atom j, nc represents the set of neighbours to an atom at a given neighbour distance c, and $\delta$ is the Kronecker delta function. $N_X$ is the number of atoms of type X and $N_c$ is the number of neighbours an atom has at nearest neighbour distance c. Even for a perfect cluster, f can not reach the value of 1 due to surface area effects.

### 5.3.5 Simulation Set-up

A small sample cell of 2000 atoms is initiated in the $\alpha$-iron configuration. A random selection of the atoms is then replaced with a different element until a certain percentage of foreign element is reached. The general procedure used was to take the random alloy and thermally equilibrate it for 10 ps using MD, with periodic constant pressure boundary conditions. The configuration of the alloy was then allowed to evolve under the Metropolis-MD algorithm (explained in sec. 5.3.3). This algorithm changes the configuration of the atoms to minimise the Gibbs energy.

The distribution of the alloy as well as any change to the box dimensions was then analysed. This procedure can be repeated at various concentrations of alloy and temperature to explore the clustering properties of the alloy. The interaction of the alloy with a void was also studied. A void of 200 vacancies was created in the centre of the simulation box by the same procedure described in sec. 4.4.1. The metropolis-MD algorithm was then used to explore the attraction of elements to the voids surface.

## 5.4 Results: Binary Alloys

### 5.4.1 Nearest Neighbour Distance

Initially the properties of a single substitutional alloying atom in a perfect BCC iron lattice were explored. The nearest neighbour spacing as compared to that in pure iron is shown in fig. 5.2. Each row (period) has a similar trend in size mismatch. There is a larger spacing towards the edge of the group with the minima occurring in the same column (group) as iron in the higher periods. Only $Cr^{24}$, $Mn^{25}$ and $Co^{27}$ show a contraction of the distance by 0.005, 0.002 and 0.006 Å respectively. Periods 5 and 6 show similar spacing trends, and are all oversized compared with period 4 elements.

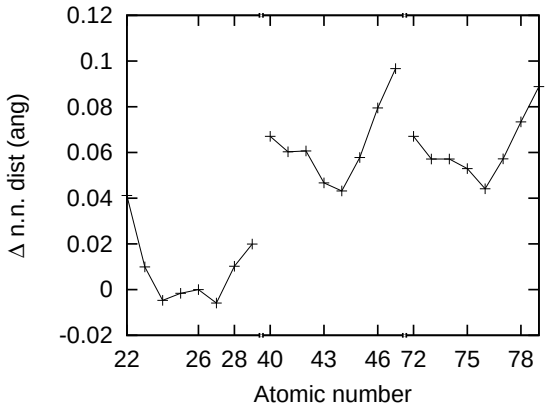


*Figure 5.2: A single alloying element, modelled by the rescaled iron potentials, is embedded in a perfect BCC lattice and quenched at 0 K and 0 GPa. The alloying elements first nearest neighbour distance is plotted relative to the equilibrium iron spacing. The value is negative if the bond is shorter than in pure iron.*

### 5.4.2 Bonding Energy

For Finnis-Sinclair potentials the bonding energy can not be directly defined in a pair wise manner, due to the density based terms that involve summing over all neighbours. However, the cohesion energy can be re-written as:

$$E_{coh} = -\sum_i \sqrt{\rho_i} \qquad \rho_i = \sum_j \phi_{ij}$$

$$E_{coh} = -\sum_i \frac{\sum_j \phi_{ij}}{\sqrt{\rho_i}}$$

$$E_{coh} = \frac{1}{2}\sum_i \sum_j \phi_{ij} \left[ \frac{1}{-\sqrt{\rho_i}} + \frac{1}{-\sqrt{\rho_j}} \right]$$

Where j may not equal i. $\phi_{ij}$ is the pair-wise embedding term and $\rho_x$ is the density around atom x, calculated from the sum of $\phi_{ij}$ for atoms surrounding x. This allows a bonding energy to be expressed:

$$E_{ij} = v_{ij} + \phi_{ij} \left[ \frac{1}{-\sqrt{\rho_i}} + \frac{1}{-\sqrt{\rho_j}} \right]$$

Where $v_{ij}$ is the pair potential contribution. The cohesion term can be made truly pair-wise if $\rho_i$ and $\rho_j$ are approximated by their equilibrium value $\rho_0$. In the present work the correct values of $\rho_i$ and $\rho_j$ are used.

Figure 5.3 shows the bonding energy between an iron atom and the various transition metals. It can be seen that the iron-alloy bonds are stronger than the iron-iron bonds for all elements, apart from Mn which is +0.27 eV less bound. The bonding is tighter in the higher period groups. There is a decrease in bond strength towards the edge of period 5 and 6. This is perhaps correlated with the size mismatch trends, which tend to have greater mismatch at the edges of the period group.

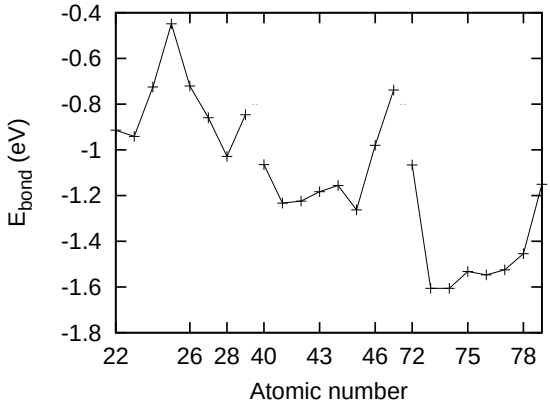


*Figure 5.3*: *Graph showing the 1 n.n. bonding energy between an alloying atom and an iron atom, using the rescaled iron potentials. The graph is split by period of the transition metals.*

### 5.4.3 Binary Alloy

The equilibrium distribution of a single alloying element at concentration 2.5% and temperature of 0 K is studied. The Metropolis-MD algorithm is run until equilibrium is reached. The clustering behaviour was studied by looking at the neighbour correlation at various distances and the results are shown in table 5.2. 15 of the 23 elements studied show repulsive or neutral self-attraction across first, second and third n.n. distances. 5 elements (Mn, Cu, Ag, Os, Au) show strong attraction at 1 n.n. leading to clustering, which is reflected at first second and third neighbour distance. The remaining three (Co, Ni and Pd) show strong

attraction at 2 n.n.

Of the 5 elements that form tight clusters, only 4 of them have attractive alloy-alloy dimers. The clustering of Mn is driven by gains in the embedding energy, while the other 3 (all group 11) are driven to cluster by the pair potential. Counter-intuitively Os does not have attraction for dimers, yet still clusters.

To further explore the clustering of Os, the trimer formation energy was measured. This was defined as the energy to add a single atom at 1 n.n. to a dimer. The trimer formation energy is attractive (-0.05 eV). However, the dimer formation energy is repulsive (0.06 eV) and clustering occurs even at 0 K. The dimer formation is also repulsive at 2 n.n. (0.04 eV) and strongly repulsive (0.19 eV) at 3 n.n. distance. This high value allows dimers to be formed in the system by metropolis jumps from the 3 n.n. state to the 1 or 2 n.n. state, which lowers the energy. Therefore, Os 1 n.n. dimers can form in the system if the initial random distribution contains any 1 n.n. or 3 n.n. pairs of alloying atoms. Once there are dimers, trimer formation becomes favourable, and clusters can grow on these nucleation sites.

### 5.4.4 Vacancy Binding

The binding of alloying elements to both single vacancies and to voids was considered. The binding energy is defined as the system energy for the atom at 1 n.n. to a vacancy, with the energy for a system with well separated atom and vacancy subtracted. Negative energy is attraction to the vacancy in this definition. The binding energies for an alloying element at 1 n.n. to a vacancy are displayed in fig. 5.4. Almost all the elements show attraction to a vacancy at 1 n.n. except V and Co. This is likely due to most of the elements being oversized in iron, and so they may release part of the strain field by approaching a vacancy.

Figure 5.5 explores how the bonding energetics are related to the vacancy binding energies. When the alloying element, X, is moved next to the vacancy, one 1 n.n. Fe-X bond is destroyed, while one 1 n.n. Fe-Fe bond is created. The figure compares the energetics due to the formed and annihilated bond, to the actual binding energy of the vacancy. It can be seen that the change in 1 n.n. bonding

is not the dominant effect in the vacancy binding. In terms of 1 n.n. bonding, it would be beneficial to have the alloy and vacancy separated (except Mn which is attractive). The stress relieved by moving the defect to the vacancy is the dominant factor in the attractive vacancy-binding energy.

The interaction of the alloy with a void was also studied. A stable faceted-void of 200 vacancies was created by iteratively removing the highest energy atom in a quenched lattice (as explained in sec. 4.4.1). Alloy atoms are then randomly placed on the remaining lattice sites before equilibrating to a given temperature. Sites on the surface of the void and close to it can be identified by examining the potential energy of the atoms. Distinct jumps in the energy landscape as number of nearest neighbour change allow identification of such sites, as shown in fig. 5.6. After using this method to generate a list of first nearest neighbours to the void, second nearest neighbours can be obtained by finding the closest atoms to the first nearest neighbours.

The Metropolis-MD algorithm was run in the presence of the void, with 2.5% alloying element at 0 K. The Void-alloy attraction was measured by counting the number of alloying atoms present at $1^{st}$ and $2^{nd}$ nearest neighbour distance from the voids surface. This number was normalised by the total number of alloy atoms in the system. All of the alloying elements show strong interaction at either first or second nearest neighbour to the void, as can be seen in table 5.2.

For periods 5 and 6 the preference for first or second neighbour site is correlated with the lattice size mismatch of the element (fig. 5.2). The elements at the edge of each period prefer 1 n.n., where as those in the centre prefer 2 n.n. sites to the void. For these groups the lattice mismatch seems to be the main driving factor. Larger lattice mismatch corresponds to greater lattice strain which can be relieved by vicinity to the void. For lesser lattice mismatch the alloy balances the loss of binding next to the void against the gains from reduced stress by occupying 2 n.n. sites. The attraction for period 4 elements seems to follow a different trend, not correlated to the lattice mismatch. There is strong attraction at 1 n.n. to the void across the group with the exception of Ti and V.

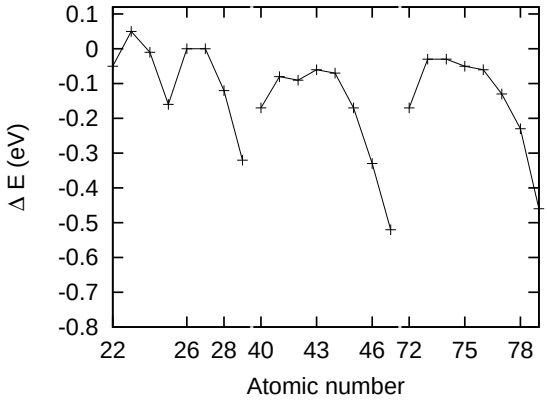


*Figure 5.4*: *Graph showing the binding energy of a single transition metal atom to a vacancy in pure iron, as modelled by the rescaled iron potentials. The energy is defined as the system energy for the atom at 1 n.n. to a vacancy with the energy for a well separated atom and vacancy subtracted.*

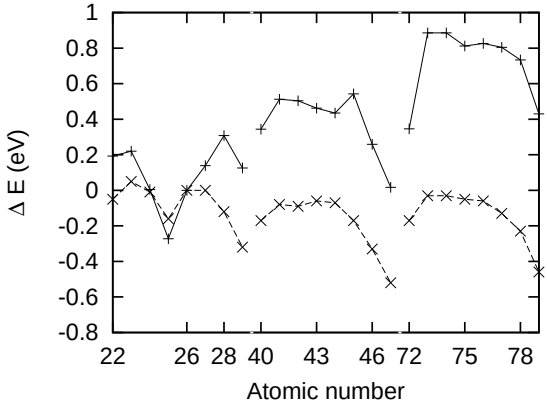


*Figure 5.5*: *graph shows: [solid line] the bonding strength of Fe-X subtracted from the bonding strength of Fe-Fe, as modelled by the rescaled iron potentials. Where both bonds are at 1 n.n. and X is one of the alloying transition metals. [dotted line] shows the vacancy binding energy data from fig. 5.4 for comparison.*

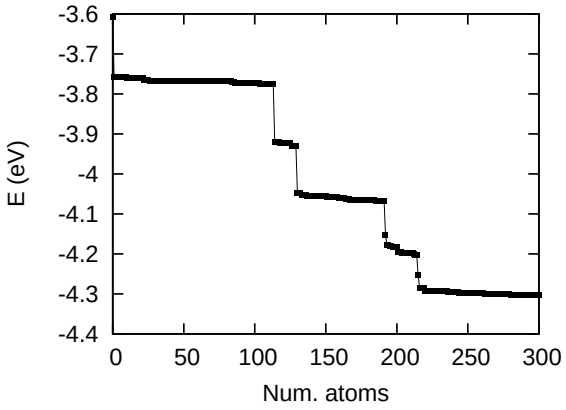


*Figure 5.6*: *Shows the energy distribution of atoms in a quenched sample containing a void in iron. The plateau (approx. 1 - 120) is related to atoms on the voids surface The next long plateau (approx. 130 - 190) is related to atoms along the edges of the voids faceted faces. The two small regions are various anomalies including corner atoms.*

*Table 5.2: Table detailing the properties of 2.5% of a single alloying element in α-iron, equilibrated at 0 K. "n.n. Dist" is the nearest neighbour distance around a single substitutional alloy atom as compared to the equilibrium iron spacing. The formation energy for a dimer of each element in pure iron is shown for $1^{st}$ and $2^{nd}$ neighbour distance. Energetically favourable dimers have negative energy and are coloured blue. Correlation (see sec. 5.3.4) refers to the percentage chance of finding an alloying atom at $1^{st}$, $2^{nd}$ and $3^{rd}$ nearest neighbour distance from another. Due to finite size surface effects, these number can not be 100%. Attraction or the alloy to a void of 200 vacancies is also measured. The percentages of the alloy found at $1^{st}$ and $2^{nd}$ nearest neighbour distance to the void is displayed. For both the clustering and void study, a result of 2.5% represents a neutral system where the alloying element is neither attracted or repelled. A result of less than 2.5% represents a repulsion and is coloured green, greater than this represents attraction and is coloured blue.*

| | **Dimer Formation** | | **Correlations** | | | **Void Attraction** | |
|---|---|---|---|---|---|---|---|
| Atm. Num. | 1 n.n. | 2 n.n. | corr 1 n.n. | corr 2 n.n. | corr 3 n.n. | 1 n.n. | 2 n.n. |
| **$^{22}$Ti** | 0.29 | 0.07 | 0 | 0 | 3 | 16 | 81 |
| **$^{23}$V** | 0.28 | 0.08 | 0 | 0 | 0 | 0 | 98 |
| **$^{24}$Cr** | 0.24 | 0.12 | 0 | 0 | 3 | 98 | 0 |
| **$^{25}$Mn** | -0.07 | -0.07 | 45 | 38 | 18 | 95 | 2 |
| **$^{27}$Co** | 0.05 | -0.02 | 0 | 49 | 24 | 79 | 20 |
| **$^{28}$Ni** | 0.01 | -0.07 | 26 | 32 | 18 | 99 | 1 |
| **$^{29}$Cu** | -0.21 | -0.18 | 68 | 49 | 42 | 90 | 9 |
| **$^{40}$Zr** | 0.41 | 0.06 | 0 | 1 | 2 | 84 | 16 |
| **$^{41}$Nb** | 0.45 | 0.11 | 0 | 0 | 1 | 21 | 73 |
| **$^{42}$Mo** | 0.32 | 0.09 | 0 | 1 | 3 | 18 | 77 |
| **$^{43}$Tc** | 0.08 | 0.03 | 0 | 2 | 0 | 15 | 84 |
| **$^{44}$Ru** | 0.06 | -0.01 | 0 | 5 | 0 | 12 | 86 |
| **$^{45}$Rh** | 0.14 | 0.01 | 0 | 2 | 0 | 90 | 8 |
| **$^{46}$Pd** | 0.01 | -0.11 | 10 | 26 | 4 | 99 | 0 |
| **$^{47}$Ag** | -0.29 | -0.27 | 56 | 49 | 30 | 99 | 0 |
| **$^{72}$Hf** | 0.48 | 0.08 | 0 | 2 | 2 | 85 | 13 |
| **$^{73}$Ta** | 0.50 | 0.08 | 0 | 1 | 3 | 4 | 93 |
| **$^{74}$W** | 0.39 | 0.10 | 0 | 0 | 2 | 6 | 92 |
| **$^{75}$Re** | 0.20 | 0.13 | 0 | 0 | 2 | 16 | 81 |
| **$^{76}$Os** | 0.06 | 0.04 | 56 | 49 | 31 | 7 | 40 |
| **$^{77}$Ir** | 0.23 | 0.10 | 0 | 1 | 0 | 58 | 27 |
| **$^{78}$Pt** | 0.25 | 0.06 | 0 | 1 | 0 | 93 | 4 |
| **$^{79}$Au** | -0.02 | -0.11 | 57 | 59 | 32 | 98 | 0 |

### 5.4.5 Phase diagrams

The properties of the system with one alloying element was studied by running the Metropolis-MD algorithm on samples of varying temperature and concentration. A temperature ranges of 0 to 1500 K was considered and a concentration range of 1 to 20%. Initially 16 even spaced samples were taken in this phase space, in a 4 by 4 grid. Based on the results of these, further samples were taken to define any trends seen in the data. The samples produced under various conditions were studied for phase transitions by measuring: ordering of the alloy at $1^{st}$, $2^{nd}$ and $3^{rd}$ nearest neighbour and changes or asymmetries in the box dimensions. The types of behaviours present are summarised in table 5.4.5 and discussed below.

Of the 23 diagrams produced (one for each alloying element) 13 of the diagrams show no significant change over the phase-space. Ti, V, Cr, Zr, Nb, Mo, Tc, and Hf show no correlation of the alloy across the range. Cu, Ag, Os and Au (mostly group 11 elements) show tight clustering across the range. Although Co shows 2 n.n. ordering at 0 K this order is destroyed by even low temperatures so the diagram was explored no further.

The remaining 10 alloying elements were studied in more detail. These samples were studied for sharp changes in correlation or box dimensions. Boundary lines were placed by finding the steepest gradient between sample points. If the change was within what would be expected from background fluctuations it was ignored.

Figures 5.7 to 5.18 show diagrams for the 11 elements that exhibit transitions. Table 5.4 gives more information on the regions present.

Broadly, there are two types of transitions in the diagrams: concentration driven and temperature driven. Concentration driven transitions tend to be a sharp change in a system property across all temperature ranges at a certain concentration. This behaviour is exhibited by Rh (fig. 5.11), Ta (fig. 5.14), W (fig. 5.15), Re (fig. 5.16), Ir (fig. 5.17), and Pt (fig. 5.18). In all of these concentration driven transition, apart from Ta, the transition is from disordered to tight cluster formation with increasing concentration. Ta showed a transition to 2 n.n. ordering.

The remaining 4 elements show temperature driven phase transitions: Mn (fig. 5.7),

Ni (fig. 5.8 & 5.9), Ru (fig. 5.10), and Pd (fig. 5.12 & 5.13). Mn and Ru show the simplest transitions. Clustering behaviours is destroyed with increasing temperature. Denser concentrations require higher temperatures to become disordered.

Ni and Pd initially show similar transition trends to that of Mn and Pd. However at higher concentrations the transition temperature begins to decrease again. In the case of Ni this effect is linked to a change in the underlying box dimensions (fig. 5.9) which favours growth of an elongated 111 precipitate. beyond a concentration of around 10% the box becomes elongated along a single axis, deviating from its initial cubic dimensions. Beyond this change the transition temperature for the disordered phase decreases. Pd also shows a skewing of the box dimensions beyond certain concentrations and temperatures (fig. 5.13) favouring a precipitate orientated in the 100 direction.

*Table 5.3*: *Elements marked by phase transition type, for a range of concentrations up to 20% and temperatures up to 1500 K. T is temperature driven, C is concentration driven, and A is always clustered. Uncoloured elements are always disordered.*

| group | 4 | 5 | 6 | 7 | 8 | 9 | 10 | 11 |
|---|---|---|---|---|---|---|---|---|
| period 4 | $Ti^{22}$ | $V^{23}$ | $Cr^{24}$ | T $Mn^{25}$ | $Fe^{26}$ | $Co^{27}$ | T $Ni^{28}$ | A $Cu^{29}$ |
| period 5 | $Zr^{40}$ | $Nb^{41}$ | $Mo^{42}$ | $Tc^{43}$ | T $Ru^{44}$ | C $Rh^{45}$ | T $Pd^{46}$ | A $Ag^{47}$ |
| period 6 | $Hf^{72}$ | C $Ta^{73}$ | C $W^{74}$ | C $Re^{75}$ | A $Os^{76}$ | C $Ir^{77}$ | C $Pt^{78}$ | A $Au^{79}$ |

*Table 5.4: Summary of phase diagrams for concentrations up to 20% and temperatures up to 1500 K. interactions are categorised at first second and third nearest neighbour (n.n.) as repulsive (R), Neutral (N), slightly attractive (SA), and attractive (A).*

| Atomic Num. | 1 n.n. | 2 n.n. | 3 n.n. | comments |
|---|---|---|---|---|
| 22 | R | R | N | Disordered apart from small correlation at 3 n.n. at high concentration |
| 23 | R | R | N/A | Disordered, apart 3 n.n. attraction at high concentration and low temp. |
| 24 | R | R | N/A | Disordered, apart from 3 n.n. attraction at high concentration and low temp. |
| 25.i | A | A | A | Clustered phase at low temperature |
| 25.ii | SA | SA | N | Entropy driven phase transition to smaller clusters, sharp at low concentrations |
| 27 | R | SA | N | Disordered |
| 28.i | N | SA | R | Disordered |
| 28.ii | A | A | A | Clusters are extended along the 111 direction, break up at low c by entropy, high c by box distortion |
| 29 | A | A | A | Always clustered , cell elongates |
| 40 | R | N/SA | N | Mostly disordered, slight 2 n.n. correlation at high concentration |
| 41 | R | R/N | N | Mostly disordered, slight 2 n.n. correlation at high concentration |
| 42 | R | R/SA | N | Mostly disordered, slight 2 n.n. correlation at high concentration |
| 43 | N/A | N/A | N | Disordered |
| 44.i | N | N | N | Clusters broken by temperature |
| 44.ii | A | A | A | Clusters present, entropically destroyed |
| 45.i | R | SA | R | Mostly disordered at for concentrations below 10% |
| 45.ii | A | A | R | Concentration driven change to small clusters |
| 46.i | N | SA | R | Mostly disordered |
| 46.ii | A | A | A | Clusters elongated in 100 direction, favouring 2 n.n attraction |
| 47 | A | A | A | Plates form in 100 plane elongating the cell, 1 and 2 n.n. correlation is strongest |
| 72 | R | N/SA | N | Mostly disordered |
| 73.i | R | R/N | N | Disordered |
| 73.ii | R | A | A | Concentration driven clustering favouring 2 and 3 n.n. correlation |
| 74.i | R | R | A | Mostly disordered |
| 74.ii | A | A | A | Spherical cluster form, box elongates |
| 75.i | R | R | N | Disordered |
| 75.ii | A | A | A | Spherical clusters, sharp onset in 1, 2 and 3 n.n. correlation |
| 76 | SA | SA | N | Clusters across the range |
| 77.i | R | SA | R | Mostly disordered, some slight 2 n.n. correlations |
| 77.ii | A | A | A | Several small compact clusters form |
| 78.i | R | N | R | Disordered |
| 78.ii | A | A | A | Tight clusters elongated in 100 direction, box also elongates |
| 79 | A | A | A | Tight clusters |

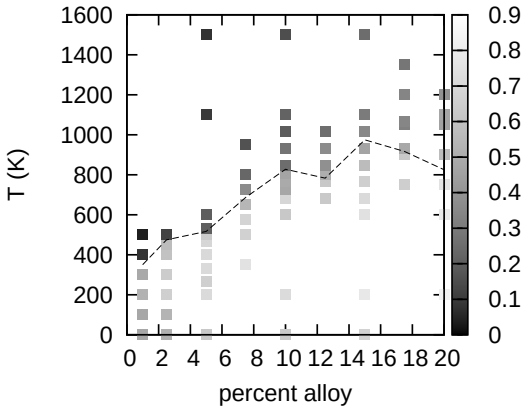


*Figure 5.7*: *Mn: phase diagram for* 1 *n.n. self-attraction in Mn. A value of 1, indicated by light squares, represents strong self-attraction (clustering). A value of 0, indicated by dark squares, represents repulsion of the alloying element from itself. The line marks the position of phase change. Numbers in brackets refer to the phases marked in table 5.4.5. A single cluster (25.i) (below line on graph), is broken into several smaller clusters (25.ii) (above line on graph) with increasing temperature.*

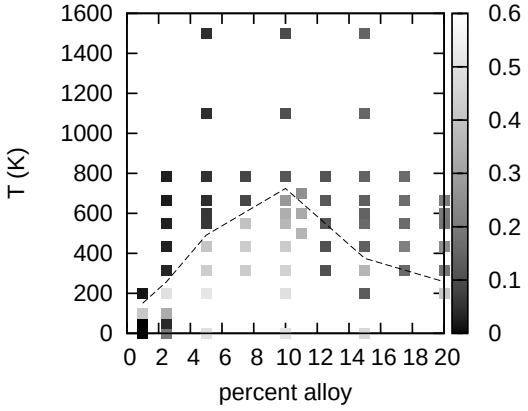


*Figure 5.8*: *Ni: format the same as fig. 5.7. Shows the first nearest neighbour correlation for Ni. Clustering present at low temperature and medium concentration (28.ii).*

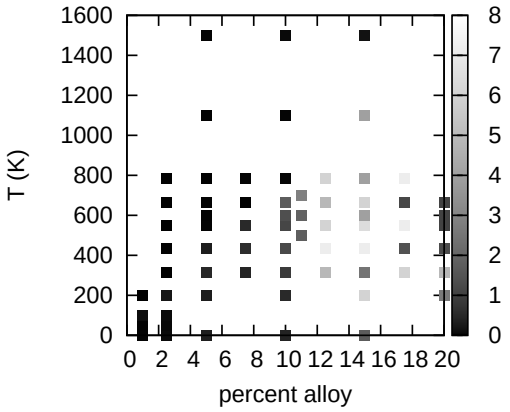


*Figure 5.9*: *Ni: format the same as fig. 5.7. Shows the elongation of the box along one axis by plotting the longest axis of the box minus the shortest, in angstroms. This onset of box elongation is linked to the phase transition.*

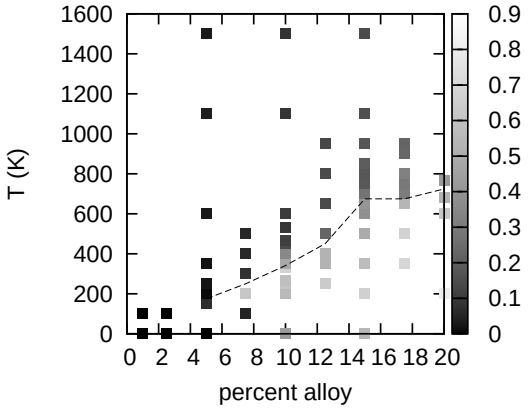


*Figure 5.10*: *Ru: format the same as fig. 5.7. Shows the first nearest neighbour correlation for Ru. Clustered phase at low temperature (44.i), entropically destroyed (44.ii).*

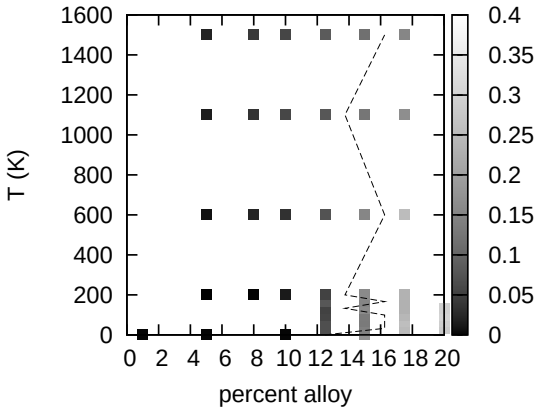


*Figure 5.11*: *Rh: format the same as fig. 5.7. Shows the first nearest neighbour correlation for Rh. Concentration driven phases transition from solute (45.i) to small precipitate clustering (45.ii).*

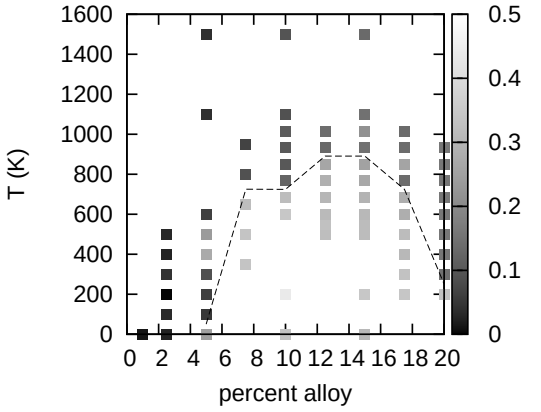


*Figure 5.12*: *Pd: format the same as fig. 5.7. Shows the first nearest neighbour correlation for Pd. Region of low temperature and medium concentration shows clustering (Pd.ii).*

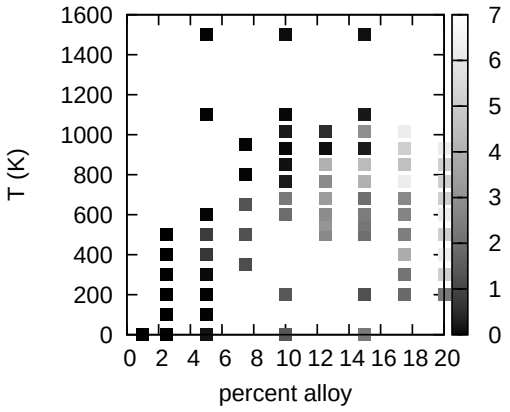


*Figure 5.13*: *Pd: format the same as fig. 5.7. Shows the elongation of the box along one axis by plotting the longest axis of the box minus the shortest, in angstroms. This onset of box elongation is linked to the phase transition.*

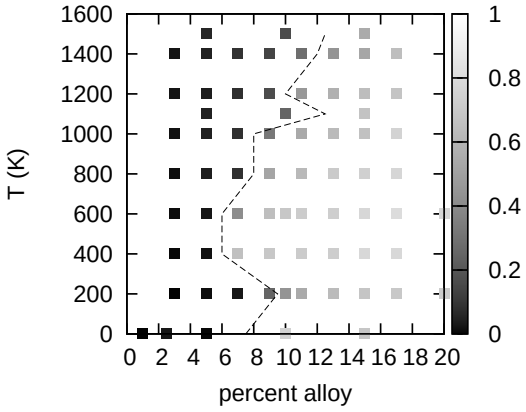


*Figure 5.14*: *Ta: format the same as fig. 5.7. Shows the second nearest neighbour correlation for Ta. The alloy is disordered at low concentration. At higher concentration correlation in the second and third nearest neighbours becomes apparent. Signifying the onset of second nearest neighbour clustering (73.ii).*

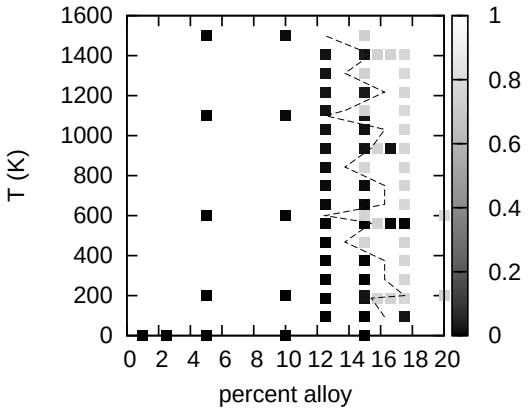


*Figure 5.15*: *W: format the same as fig. 5.7. Shows the first nearest neighbour correlation for W. Undergoes a concentration driven phase transition from disordered at low concentration (black dots, 74.i) , to clustering at higher concentration (white dots, 74.ii)*

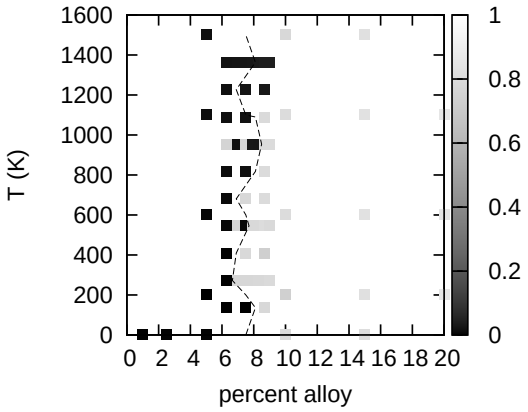


*Figure 5.16*: *Re: format the same as fig. 5.7. Shows the first nearest neighbour correlation for Re. Undergoes a concentration driven phase transition from disordered at low concentration (black dots, 75.i) , to clustering at higher concentration (white dots, 75.ii)*

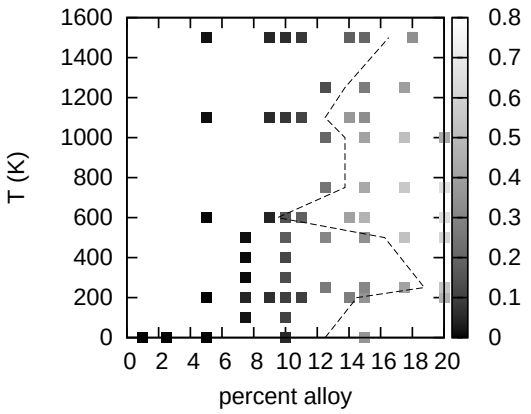


*Figure 5.17*: *Ir: format the same as fig. 5.7. Shows the first nearest neighbour correlation for Ir. undergoes a phase concentration driven phase transition from disordered (black dots, 77.i) , to several small clusters (white dots, 77.ii) at higher concentration.*

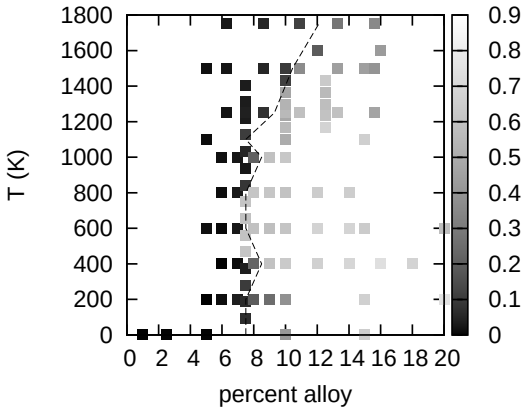


*Figure 5.18*: *Pt: format the same as fig. 5.7. Shows the first nearest neighbour correlation for Pt. undergoes a concentration driven phase transition from disordered at low concentration (black dots, 78.i) , to clustering at higher concentration (white dots, 78.ii)*

## 5.5 Results: Tertiary Alloys

2.5% of two different alloying elements (5% alloy total) were randomly added to a BCC iron lattice at 0 K. The Metropolis-MD algorithm was then run to minimise the Gibbs energy of the system, for the given configuration. The interaction of the elements can be categorised by the change in their self-attraction along with the cross-elemental attraction. There are 253 ways to add two elements to the system, all of which were simulated. There are too many cases to talk about individually and so only the alloys with interesting properties will be discussed.

The data was analysed by studying changes in self-attraction at up to 3 n.n. as compared to the correlation in the binary alloys. That is, the percentage correlation of a given element as measured in the binary samples (shown table 5.2) is subtracted from the correlation of the same element in the tertiary samples. A change of less than $1 + \sqrt{corr}$ was ignored, where corr is the percentage self-correlation at a particular neighbour distance in the binary alloy. Additionally cross-correlation of less than 5% was considered insignificant.

With these filters, 83 of the samples can be said not to interact significantly: each element retains its original self-attraction properties, with little cross-interaction. This predominately arose from mixing two elements that were not self-attractive (64 cases). Mixing two self attractive alloys always produced some form of change.

In some cases even when there was no significant cross-interaction, the properties of the individual elements are still changed (88 cases). Of these cases, the most likely event is for one element to increase its self-attraction while the other is unaffected (59 cases).

The strongest changes seen were mostly from mixing a repulsive alloy with an attractive one, resulting in the complete dissolution of the attractive clusters. This could happen with or without a cross-attraction between the alloys. That is, the clusters can absorb the new element, or be destroyed by it leaving no clustering of any type. The largest changes are observed in samples containing Au which strongly clusters in the single component case.

Tables 5.5 and 5.6 show the effects of the alloying components. Table 5.5 shows

the self-correlation of each element in the presence of each of the other elements. Changes in the correlation down the columns show how that particular element is influenced by the element in the relevant row. It can be seen that six elements (Mn, Ni, Cu, Ag, Os, and Au) strongly cluster at 1 n.n. in the presence of most other elements. Exceptions to this can be seen, such as V strongly destroying Ni clusters.

It can also be seen from the rows of the table, that the presence of a strongly clustering element often induced clustering in the secondary element. For example, when Ag is present in the system, several elements that normally prefer not to cluster start to show correlations. Typically this is associated with cross-correlations between the elements (see table 5.6). Cross-correlations only occur when one of the six strongly clustering elements is present in the system. These six elements tend to react strongly with each other.

*Table 5.5: Self-correlation: table is for a system of bcc iron at 0 K with 2.5% of two different transition metals in it (5% total). The values show the percentage correlation of the element in a given column, when in the presence of the element in a given row. Green indicates the element is self-repelling, blue indicates the element is self-attracting. Correlations are at 1 n.n. distance.*

| | Ti | V | Cr | Mn | Fe | Co | Ni | Cu | Zr | Nb | Mo | Tc | Ru | Rh | Pd | Ag | Hf | Ta | W | Re | Os | Ir | Pt | Au |
|---|---|---|---|---|---|---|---|---|---|---|---|---|---|---|---|---|---|---|---|---|---|---|---|---|
| **$^{22}$Ti** | | 0 | 0 | 51 | | 0 | 46 | 63 | 0 | 0 | 0 | 0 | 0 | 0 | 0 | 56 | 0 | 0 | 0 | 0 | 62 | 0 | 0 | 54 |
| **$^{23}$V** | 0 | | 0 | 31 | | 0 | 4 | 65 | 0 | 0 | 0 | 0 | 0 | 0 | 5 | 58 | 0 | 0 | 0 | 0 | 62 | 0 | 0 | 46 |
| **$^{24}$Cr** | 0 | 0 | | 47 | | 0 | 47 | 62 | 0 | 0 | 0 | 0 | 0 | 0 | 0 | 50 | 0 | 0 | 0 | 0 | 62 | 0 | 0 | 56 |
| **$^{25}$Mn** | 0 | 0 | 0 | | | 0 | 8 | 52 | 0 | 0 | 0 | 1 | 3 | 0 | 3 | 49 | 0 | 2 | 0 | 5 | 52 | 0 | 0 | 49 |
| **$^{26}$Fe** | | | | | | | | | | | | | | | | | | | | | | | | |
| **$^{27}$Co** | 0 | 0 | 0 | 38 | | | 44 | 56 | 0 | 0 | 0 | 0 | 0 | 0 | 20 | 58 | 0 | 0 | 0 | 0 | 50 | 0 | 0 | 60 |
| **$^{28}$Ni** | 0 | 0 | 0 | 23 | | 0 | | 57 | 0 | 0 | 0 | 0 | 0 | 0 | 7 | 63 | 0 | 0 | 0 | 0 | 61 | 0 | 0 | 48 |
| **$^{29}$Cu** | 0 | 0 | 0 | 19 | | 11 | 20 | | 0 | 0 | 0 | 6 | 15 | 9 | 16 | 40 | 0 | 0 | 0 | 4 | 8 | 3 | 1 | 48 |
| **$^{40}$Zr** | 0 | 0 | 0 | 32 | | 0 | 7 | 63 | | 0 | 0 | 0 | 0 | 0 | 3 | 61 | 0 | 0 | 0 | 0 | 55 | 0 | 0 | 58 |
| **$^{41}$Nb** | 0 | 0 | 0 | 48 | | 0 | 48 | 58 | 0 | | 0 | 0 | 1 | 0 | 9 | 50 | 0 | 0 | 0 | 0 | 62 | 0 | 0 | 57 |
| **$^{42}$Mo** | 0 | 0 | 0 | 48 | | 0 | 44 | 60 | 0 | 0 | | 0 | 0 | 0 | 3 | 51 | 0 | 0 | 0 | 0 | 62 | 0 | 0 | 54 |
| **$^{43}$Tc** | 0 | 0 | 1 | 33 | | 0 | 46 | 53 | 0 | 0 | 0 | | 1 | 0 | 1 | 59 | 0 | 0 | 0 | 0 | 59 | 0 | 0 | 56 |
| **$^{44}$Ru** | 0 | 0 | 0 | 41 | | 2 | 15 | 54 | 0 | 0 | 0 | 0 | | 0 | 3 | 43 | 0 | 0 | 1 | 0 | 49 | 0 | 0 | 56 |
| **$^{45}$Rh** | 0 | 0 | 0 | 12 | | 0 | 42 | 63 | 0 | 0 | 0 | 0 | 0 | | 3 | 50 | 0 | 0 | 0 | 0 | 57 | 0 | 0 | 57 |
| **$^{46}$Pd** | 0 | 0 | 0 | 42 | | 0 | 45 | 64 | 0 | 0 | 0 | 0 | 4 | 0 | | 54 | 0 | 0 | 0 | 0 | 56 | 0 | 0 | 63 |
| **$^{47}$Ag** | 0 | 0 | 0 | 25 | | 4 | 37 | 46 | 0 | 0 | 0 | 7 | 13 | 11 | 16 | | 0 | 0 | 0 | 7 | 27 | 2 | 15 | 53 |
| **$^{72}$Hf** | 0 | 0 | 0 | 49 | | 0 | 34 | 75 | 0 | 0 | 0 | 0 | 0 | 0 | 5 | 54 | | 0 | 0 | 0 | 58 | 0 | 0 | 50 |
| **$^{73}$Ta** | 0 | 0 | 0 | 0 | | 0 | 49 | 74 | 0 | 0 | 0 | 0 | 0 | 0 | 5 | 55 | 0 | | 0 | 0 | 57 | 0 | 0 | 51 |
| **$^{74}$W** | 0 | 0 | 0 | 1 | | 0 | 41 | 63 | 0 | 0 | 0 | 0 | 0 | 0 | 9 | 59 | 0 | 0 | | 0 | 56 | 0 | 0 | 55 |
| **$^{75}$Re** | 0 | 1 | 0 | 29 | | 0 | 28 | 38 | 0 | 0 | 0 | 0 | 1 | 0 | 17 | 45 | 0 | 0 | 0 | | 38 | 0 | 0 | 51 |
| **$^{76}$Os** | 0 | 0 | 1 | 20 | | 10 | 36 | 28 | 0 | 0 | 0 | 20 | 14 | 14 | 7 | 48 | 0 | 0 | 0 | 31 | | 0 | 0 | 47 |
| **$^{77}$Ir** | 0 | 0 | 0 | 16 | | 0 | 37 | 47 | 0 | 0 | 0 | 0 | 2 | 0 | 9 | 56 | 0 | 0 | 0 | 0 | 48 | | 0 | 60 |
| **$^{78}$Pt** | 0 | 0 | 0 | 6 | | 1 | 34 | 64 | 0 | 0 | 0 | 0 | 0 | 0 | 14 | 55 | 0 | 0 | 0 | 0 | 50 | 0 | | 47 |
| **$^{79}$Au** | 0 | 0 | 0 | 19 | | 1 | 35 | 70 | 0 | 0 | 0 | 5 | 22 | 10 | 18 | 50 | 0 | 0 | 0 | 0 | 56 | 4 | 13 | |

*Table 5.6: Cross-correlation: table is for a system of bcc iron at 0 K with 2.5% of two different transition metals in it (5% total). The table shows the first nearest neighbour percentage cross-correlation for the elements in the relevant row and column. Green indicates repulsive cross-correlation, while blue indicates attractive cross-correlation.*

| | V | Cr | Mn | Fe | Co | Ni | Cu | Zr | Nb | Mo | Tc | Ru | Rh | Pd | Ag | Hf | Ta | W | Re | Os | Ir | Pt | Au |
|---|---|---|---|---|---|---|---|---|---|---|---|---|---|---|---|---|---|---|---|---|---|---|---|
| **$^{22}$Ti** | 0 | 0 | 0 | | 0 | 0 | 1 | 0 | 0 | 0 | 0 | 0 | 0 | 0 | 0 | 0 | 0 | 0 | 0 | 4 | 0 | 0 | 7 |
| **$^{23}$V** | | 0 | 0 | | 0 | 0 | 0 | 0 | 0 | 0 | 0 | 0 | 0 | 0 | 0 | 0 | 0 | 0 | 0 | 10 | 0 | 0 | 6 |
| **$^{24}$Cr** | | | 0 | | 1 | 0 | 1 | 0 | 0 | 0 | 0 | 0 | 0 | 0 | 7 | 0 | 0 | 0 | 0 | 12 | 0 | 0 | 5 |
| **$^{25}$Mn** | | | | | 7 | 25 | 22 | 0 | 0 | 1 | 16 | 19 | 8 | 17 | 23 | 0 | 1 | 1 | 30 | 31 | 8 | 2 | 15 |
| **$^{26}$Fe** | | | | | | | | | | | | | | | | | | | | | | | |
| **$^{27}$Co** | | | | | | 0 | 25 | 0 | 0 | 0 | 0 | 0 | 0 | 0 | 15 | 0 | 0 | 0 | 1 | 31 | 0 | 0 | 9 |
| **$^{28}$Ni** | | | | | | | 23 | 0 | 0 | 0 | 0 | 0 | 0 | 0 | 6 | 0 | 0 | 0 | 0 | 10 | 0 | 0 | 1 |
| **$^{29}$Cu** | | | | | | | | 0 | 0 | 2 | 23 | 28 | 19 | 15 | 19 | 0 | 1 | 10 | 34 | 37 | 19 | 8 | 8 |
| **$^{40}$Zr** | | | | | | | | | 0 | 0 | 0 | 0 | 0 | 0 | 0 | 0 | 0 | 0 | 0 | 0 | 0 | 0 | 3 |
| **$^{41}$Nb** | | | | | | | | | | 0 | 0 | 0 | 0 | 0 | 0 | 0 | 0 | 0 | 0 | 0 | 0 | 0 | 0 |
| **$^{42}$Mo** | | | | | | | | | | | 0 | 0 | 0 | 0 | 0 | 0 | 0 | 0 | 0 | 0 | 0 | 0 | 0 |
| **$^{43}$Tc** | | | | | | | | | | | | 0 | 0 | 0 | 19 | 0 | 0 | 0 | 0 | 23 | 0 | 0 | 11 |
| **$^{44}$Ru** | | | | | | | | | | | | | 0 | 0 | 27 | 0 | 0 | 0 | 0 | 28 | 0 | 0 | 25 |
| **$^{45}$Rh** | | | | | | | | | | | | | | 0 | 23 | 0 | 0 | 0 | 0 | 21 | 0 | 0 | 19 |
| **$^{46}$Pd** | | | | | | | | | | | | | | | 22 | 0 | 0 | 0 | 0 | 2 | 0 | 0 | 16 |
| **$^{47}$Ag** | | | | | | | | | | | | | | | | 0 | 0 | 2 | 30 | 11 | 17 | 24 | 10 |
| **$^{72}$Hf** | | | | | | | | | | | | | | | | | 0 | 0 | 0 | 0 | 0 | 0 | 1 |
| **$^{73}$Ta** | | | | | | | | | | | | | | | | | | 0 | 0 | 1 | 0 | 0 | 0 |
| **$^{74}$W** | | | | | | | | | | | | | | | | | | | 0 | 1 | 0 | 0 | 2 |
| **$^{75}$Re** | | | | | | | | | | | | | | | | | | | | 30 | 0 | 0 | 2 |
| **$^{76}$Os** | | | | | | | | | | | | | | | | | | | | | 3 | 2 | 7 |
| **$^{77}$Ir** | | | | | | | | | | | | | | | | | | | | | | 0 | 9 |
| **$^{78}$Pt** | | | | | | | | | | | | | | | | | | | | | | | 25 |

### 5.5.1 Tertiary Alloy with Void

For the sample containing the void as well as two alloying elements, the competition of attraction to the void as well as cross-interaction of the elements is studied. The 1 n.n. and 2 n.n. attraction to the void is shown in tables 5.7 and 5.8 respectively.

The cases of two elements that prefer 1 n.n. void sites being mixed is studied, 78 cases in total. Most of the time (64 cases) one of the elements will be reduced at 1 n.n. to the void, but will show some increased preference for 2 n.n. to the void. The second element will typically show some reduction at 1 n.n. distance as well.

The results for two elements that both prefer 1 n.n. sites to the void are further analysed in fig. 5.19. Two distinct areas are seen in the figure, due to the size difference between period 4 elements and period 5 or 6 elements. The size difference does not seem to be a major factor, with the strongest trend being the difference in vacancy attraction. This shows that interactions between the competing alloying elements is not the main driving force, as the vacancy attraction is the dominant factor. The samples in general show an overall decrease in coating of the void compared to what might be expected from the combination of the single samples. This is due to the cross-interaction not being strong between the elements (see table 5.9), and so one element will bind to the void, repelling the other. There is enough sites for both elements to be present on the voids surface, 50 atoms of each alloy with 190 sites at 1 n.n. to the void, but this is rarely seen.

Cases where two elements both prefer to be at 2 n.n. to the void were also studied, 45 cases in total. In general, both show a decrease in occupation at 2 n.n. to the void despite there being sufficient room for both alloys. There is almost no 1 n.n. cross correlation between the alloys and the atoms never increase their concentration at 1 n.n. to the void.

Lastly samples where one element prefers 1 n.n. to the void and another prefers 2 n.n. to the void are studied, 130 cases in total. Typically the element that prefers 2 n.n. is repelled into the bulk, while the element that prefers 1 n.n. remains, with a slight reduction in concentration.

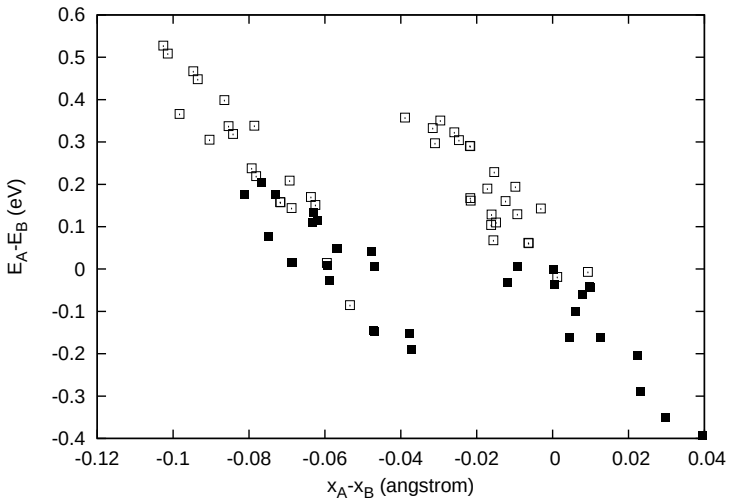


*Figure 5.19*: *The graph shows the competition between alloying elements in iron that both prefer to be at 1 n.n. to the void in a mixed sample. The difference (A-B) in vacancy binding energy of the two elements is plotted against the difference (A-B) in 1 n.n. distance in the lattice. The data points are colour coded according to which element showed a relative increase in void coverage at 1 n.n. to the void. Taking (%A-%AS)-(%B-%BS) where %A and %B refer to the percentage of alloy next to the void in the mixed sample, %AS and %AS referring to the alloy next to the void in the unmixed samples. If the quantity is positive, signifying an increase in element A at the void, the data point is coloured black. Otherwise the point is white, signifying an increase in element B at the void.*

*Table 5.7: 1 n.n. Void attraction: table shows results for a 200 vacancy-void in iron at 0 K with two other transition metals present (2.5% of each). The values are the percentage of the alloy in the relevant column found at 1 n.n. to the void, when the element in the relevant row is present. Green indicates concentrations below the equilibrium concentration (2.5%), and blue indicates concentrations above this value.*

| | Ti | V | Cr | Mn | Fe | Co | Ni | Cu | Zr | Nb | Mo | Tc | Ru | Rh | Pd | Ag | Hf | Ta | W | Re | Os | Ir | Pt | Au |
|---|---|---|---|---|---|---|---|---|---|---|---|---|---|---|---|---|---|---|---|---|---|---|---|---|
| **$^{22}$Ti** | | 0 | 82 | 100 | | 80 | 100 | 98 | 69 | 18 | 33 | 24 | 16 | 76 | 98 | 100 | 76 | 18 | 13 | 24 | 4 | 44 | 80 | 100 |
| **$^{23}$V** | 7 | | 58 | 98 | | 76 | 98 | 80 | 67 | 13 | 16 | 18 | 18 | 80 | 98 | 98 | 62 | 4 | 4 | 18 | 13 | 42 | 78 | 100 |
| **$^{24}$Cr** | 11 | 0 | | 100 | | 56 | 98 | 96 | 73 | 16 | 9 | 16 | 13 | 76 | 100 | 98 | 76 | 9 | 4 | 9 | 0 | 47 | 76 | 96 |
| **$^{25}$Mn** | 13 | 0 | 78 | | | 78 | 93 | 80 | 51 | 13 | 18 | 27 | 33 | 80 | 93 | 100 | 49 | 13 | 13 | 33 | 18 | 53 | 67 | 100 |
| **$^{26}$Fe** | | | | | | | | | | | | | | | | | | | | | | | | |
| **$^{27}$Co** | 7 | 0 | 56 | 98 | | | 98 | 96 | 38 | 13 | 13 | 9 | 11 | 67 | 100 | 98 | 47 | 2 | 0 | 16 | 2 | 36 | 73 | 98 |
| **$^{28}$Ni** | 7 | 0 | 22 | 100 | | 24 | | 80 | 31 | 13 | 11 | 7 | 11 | 36 | 93 | 100 | 27 | 4 | 4 | 7 | 4 | 22 | 47 | 100 |
| **$^{29}$Cu** | 9 | 0 | 73 | 69 | | 49 | 78 | | 49 | 13 | 16 | 16 | 16 | 69 | 93 | 96 | 51 | 4 | 16 | 20 | 16 | 42 | 76 | 98 |
| **$^{40}$Zr** | 0 | 0 | 31 | 100 | | 60 | 96 | 93 | | 0 | 4 | 2 | 0 | 71 | 98 | 100 | 18 | 0 | 0 | 2 | 9 | 22 | 96 | 98 |
| **$^{41}$Nb** | 2 | 0 | 73 | 96 | | 84 | 98 | 98 | 80 | | 22 | 16 | 20 | 76 | 100 | 100 | 67 | 9 | 0 | 9 | 9 | 53 | 82 | 98 |
| **$^{42}$Mo** | 0 | 0 | 80 | 98 | | 78 | 98 | 98 | 76 | 0 | | 2 | 18 | 89 | 98 | 100 | 71 | 7 | 7 | 24 | 7 | 56 | 87 | 100 |
| **$^{43}$Tc** | 2 | 0 | 80 | 98 | | 73 | 100 | 89 | 67 | 22 | 36 | | 31 | 76 | 96 | 98 | 71 | 9 | 13 | 20 | 2 | 36 | 80 | 98 |
| **$^{44}$Ru** | 4 | 0 | 84 | 98 | | 76 | 98 | 93 | 76 | 11 | 13 | 2 | | 80 | 98 | 98 | 60 | 11 | 4 | 11 | 0 | 44 | 71 | 100 |
| **$^{45}$Rh** | 0 | 0 | 44 | 96 | | 38 | 91 | 87 | 18 | 0 | 0 | 0 | 0 | | 100 | 98 | 7 | 0 | 0 | 2 | 0 | 0 | 91 | 100 |
| **$^{46}$Pd** | 0 | 0 | 22 | 100 | | 40 | 78 | 93 | 18 | 0 | 2 | 0 | 0 | 24 | | 98 | 16 | 4 | 0 | 2 | 0 | 11 | 31 | 98 |
| **$^{47}$Ag** | 2 | 0 | 31 | 89 | | 29 | 78 | 98 | 36 | 4 | 4 | 0 | 18 | 60 | 89 | | 29 | 2 | 0 | 20 | 16 | 42 | 67 | 89 |
| **$^{72}$Hf** | 0 | 0 | 24 | 98 | | 51 | 91 | 96 | 80 | 2 | 0 | 2 | 0 | 80 | 100 | 100 | | 0 | 0 | 0 | 0 | 29 | 87 | 100 |
| **$^{73}$Ta** | 4 | 0 | 73 | 82 | | 62 | 89 | 96 | 62 | 22 | 22 | 9 | 27 | 80 | 98 | 100 | 58 | | 2 | 31 | 16 | 42 | 87 | 98 |
| **$^{74}$W** | 7 | 0 | 69 | 93 | | 62 | 96 | 96 | 67 | 13 | 20 | 13 | 20 | 73 | 96 | 98 | 69 | 7 | | 27 | 9 | 42 | 73 | 98 |
| **$^{75}$Re** | 4 | 0 | 84 | 76 | | 71 | 98 | 82 | 76 | 16 | 9 | 9 | 20 | 84 | 96 | 91 | 67 | 2 | 7 | | 2 | 49 | 80 | 100 |
| **$^{76}$Os** | 9 | 0 | 82 | 71 | | 36 | 100 | 87 | 78 | 18 | 13 | 9 | 9 | 73 | 98 | 100 | 78 | 0 | 4 | 9 | | 44 | 82 | 96 |
| **$^{77}$Ir** | 0 | 0 | 71 | 80 | | 60 | 96 | 96 | 56 | 0 | 0 | 0 | 2 | 89 | 100 | 98 | 42 | 2 | 0 | 2 | 7 | | 93 | 98 |
| **$^{78}$Pt** | 0 | 0 | 27 | 82 | | 22 | 93 | 76 | 0 | 2 | 0 | 0 | 0 | 4 | 98 | 100 | 4 | 2 | 0 | 0 | 0 | 2 | | 98 |
| **$^{79}$Au** | 0 | 2 | 27 | 78 | | 9 | 80 | 93 | 18 | 0 | 0 | 0 | 7 | 31 | 84 | 100 | 20 | 0 | 0 | 2 | 7 | 11 | 51 | |

*Table 5.8: 2 n.n. Void attraction: table shows results for a 200 vacancy-void in iron at 0 K with two other transition metals present (2.5% of each). The values are the percentage of the alloy in the relevant column found at 2 n.n. to the void, when the element in the relevant row is present. Green indicates concentrations below the equilibrium concentration (2.5%), and blue indicates concentrations above this value.*

| | Ti | V | Cr | Mn | Fe | Co | Ni | Cu | Zr | Nb | Mo | Tc | Ru | Rh | Pd | Ag | Hf | Ta | W | Re | Os | Ir | Pt | Au |
|---|---|---|---|---|---|---|---|---|---|---|---|---|---|---|---|---|---|---|---|---|---|---|---|---|
| **$^{22}$Ti** | | 87 | 13 | 0 | | 20 | 0 | 2 | 24 | 62 | 49 | 58 | 78 | 20 | 0 | 0 | 16 | 82 | 76 | 60 | 42 | 27 | 7 | 0 |
| **$^{23}$V** | 27 | | 13 | 2 | | 24 | 2 | 18 | 16 | 47 | 44 | 51 | 60 | 9 | 2 | 2 | 13 | 42 | 84 | 51 | 60 | 22 | 11 | 0 |
| **$^{24}$Cr** | 29 | 98 | | 0 | | 36 | 0 | 4 | 9 | 22 | 24 | 31 | 49 | 11 | 0 | 2 | 13 | 67 | 53 | 42 | 29 | 13 | 11 | 2 |
| **$^{25}$Mn** | 38 | 93 | 16 | | | 22 | 4 | 18 | 16 | 40 | 56 | 73 | 62 | 20 | 4 | 0 | 11 | 69 | 80 | 53 | 73 | 22 | 13 | 0 |
| **$^{26}$Fe** | | | | | | | | | | | | | | | | | | | | | | | | |
| **$^{27}$Co** | 36 | 69 | 29 | 0 | | | 0 | 4 | 18 | 13 | 18 | 33 | 56 | 13 | 0 | 0 | 4 | 60 | 60 | 49 | 40 | 13 | 7 | 0 |
| **$^{28}$Ni** | 24 | 58 | 38 | 0 | | 67 | | 20 | 11 | 16 | 20 | 33 | 31 | 18 | 4 | 0 | 16 | 36 | 29 | 24 | 22 | 18 | 7 | 0 |
| **$^{29}$Cu** | 33 | 91 | 20 | 24 | | 51 | 18 | | 20 | 29 | 36 | 73 | 80 | 29 | 7 | 2 | 13 | 76 | 62 | 62 | 78 | 47 | 18 | 2 |
| **$^{40}$Zr** | 13 | 40 | 11 | 0 | | 38 | 4 | 4 | | 38 | 36 | 33 | 42 | 18 | 2 | 0 | 11 | 67 | 58 | 38 | 33 | 31 | 2 | 0 |
| **$^{41}$Nb** | 2 | 47 | 11 | 2 | | 13 | 0 | 2 | 7 | | 33 | 18 | 36 | 22 | 0 | 0 | 7 | 71 | 78 | 67 | 38 | 29 | 13 | 0 |
| **$^{42}$Mo** | 9 | 49 | 9 | 0 | | 22 | 0 | 2 | 9 | 44 | | 38 | 38 | 9 | 0 | 0 | 9 | 84 | 69 | 58 | 44 | 22 | 11 | 0 |
| **$^{43}$Tc** | 13 | 49 | 4 | 0 | | 27 | 0 | 11 | 11 | 47 | 27 | | 53 | 24 | 4 | 0 | 4 | 73 | 42 | 60 | 31 | 40 | 11 | 2 |
| **$^{44}$Ru** | 13 | 49 | 4 | 2 | | 24 | 0 | 7 | 2 | 38 | 36 | 33 | | 16 | 0 | 2 | 9 | 69 | 56 | 53 | 31 | 27 | 18 | 0 |
| **$^{45}$Rh** | 11 | 27 | 7 | 2 | | 58 | 9 | 13 | 18 | 11 | 16 | 24 | 31 | | 0 | 0 | 9 | 20 | 22 | 22 | 11 | 24 | 7 | 0 |
| **$^{46}$Pd** | 16 | 20 | 20 | 0 | | 40 | 18 | 4 | 16 | 20 | 24 | 31 | 38 | 18 | | 2 | 7 | 18 | 29 | 22 | 29 | 20 | 11 | 0 |
| **$^{47}$Ag** | 51 | 69 | 60 | 9 | | 67 | 22 | 2 | 38 | 42 | 51 | 87 | 82 | 40 | 11 | | 36 | 62 | 56 | 56 | 71 | 40 | 29 | 9 |
| **$^{72}$Hf** | 18 | 44 | 7 | 2 | | 33 | 4 | 2 | 9 | 36 | 40 | 42 | 58 | 16 | 0 | 0 | | 49 | 42 | 40 | 44 | 24 | 9 | 0 |
| **$^{73}$Ta** | 31 | 49 | 4 | 13 | | 31 | 7 | 2 | 2 | 9 | 9 | 16 | 16 | 11 | 0 | 0 | 9 | | 36 | 16 | 38 | 24 | 9 | 0 |
| **$^{74}$W** | 24 | 36 | 13 | 7 | | 38 | 2 | 4 | 7 | 9 | 4 | 16 | 27 | 11 | 2 | 0 | 9 | 84 | | 22 | 27 | 29 | 16 | 0 |
| **$^{75}$Re** | 22 | 44 | 4 | 16 | | 29 | 0 | 16 | 7 | 2 | 22 | 20 | 24 | 11 | 2 | 9 | 2 | 76 | 71 | | 36 | 27 | 9 | 0 |
| **$^{76}$Os** | 47 | 69 | 2 | 11 | | 13 | 0 | 11 | 4 | 47 | 53 | 47 | 33 | 16 | 0 | 0 | 2 | 64 | 78 | 62 | | 24 | 4 | 4 |
| **$^{77}$Ir** | 36 | 47 | 9 | 9 | | 40 | 4 | 4 | 9 | 13 | 20 | 22 | 40 | 4 | 0 | 2 | 11 | 29 | 29 | 18 | 33 | | 2 | 2 |
| **$^{78}$Pt** | 27 | 42 | 24 | 11 | | 40 | 7 | 22 | 11 | 9 | 9 | 20 | 29 | 16 | 0 | 0 | 11 | 13 | 16 | 16 | 13 | 11 | | 0 |
| **$^{79}$Au** | 69 | 62 | 62 | 22 | | 82 | 16 | 7 | 36 | 29 | 31 | 58 | 87 | 58 | 16 | 0 | 27 | 38 | 49 | 33 | 47 | 44 | 44 | |

*Table 5.9: Cross-correlation: table shows results for a 200 vacancy void in iron at 0 K with two other transition metals present (2.5% of each). The values are the percentage cross-correlation of the elements in the relevant row and column. Green indicates repulsive cross-correlation, while blue indicates attractive cross-correlation.*

| | V | Cr | Mn | Fe | Co | Ni | Cu | Zr | Nb | Mo | Tc | Ru | Rh | Pd | Ag | Hf | Ta | W | Re | Os | Ir | Pt | Au |
|---|---|---|---|---|---|---|---|---|---|---|---|---|---|---|---|---|---|---|---|---|---|---|---|
| **$^{22}$Ti** | 0 | 7 | 9 | | 9 | 9 | 13 | 16 | 9 | 22 | 18 | 11 | 18 | 2 | 0 | 16 | 16 | 13 | 20 | 4 | 7 | 11 | 0 |
| **$^{23}$V** | | 16 | 16 | | 4 | 20 | 9 | 11 | 2 | 2 | 7 | 4 | 11 | 0 | 0 | 16 | 2 | 2 | 9 | 9 | 11 | 18 | 0 |
| **$^{24}$Cr** | | | 13 | | 13 | 22 | 9 | 4 | 2 | 0 | 7 | 7 | 13 | 4 | 0 | 11 | 9 | 2 | 4 | 0 | 11 | 9 | 7 |
| **$^{25}$Mn** | | | | | 22 | 11 | 13 | 7 | 7 | 11 | 24 | 27 | 27 | 4 | 2 | 9 | 11 | 13 | 22 | 16 | 13 | 11 | 4 |
| **$^{26}$Fe** | | | | | | | | | | | | | | | | | | | | | | | |
| **$^{27}$Co** | | | | | | 0 | 18 | 7 | 2 | 4 | 4 | 4 | 13 | 4 | 0 | 4 | 2 | 0 | 11 | 2 | 7 | 11 | 2 |
| **$^{28}$Ni** | | | | | | | 9 | 4 | 11 | 7 | 4 | 4 | 2 | 2 | 2 | 4 | 2 | 4 | 4 | 4 | 11 | 2 | 4 |
| **$^{29}$Cu** | | | | | | | | 7 | 4 | 7 | 16 | 13 | 36 | 7 | 2 | 7 | 4 | 16 | 20 | 16 | 18 | 9 | 4 |
| **$^{40}$Zr** | | | | | | | | | 0 | 2 | 2 | 0 | 9 | 0 | 0 | 13 | 0 | 0 | 2 | 7 | 13 | 16 | 0 |
| **$^{41}$Nb** | | | | | | | | | | 13 | 11 | 11 | 20 | 2 | 2 | 11 | 9 | 0 | 9 | 4 | 16 | 16 | 0 |
| **$^{42}$Mo** | | | | | | | | | | | 2 | 13 | 20 | 0 | 0 | 9 | 7 | 7 | 24 | 4 | 11 | 7 | 0 |
| **$^{43}$Tc** | | | | | | | | | | | | 18 | 20 | 2 | 0 | 18 | 9 | 13 | 13 | 2 | 2 | 11 | 0 |
| **$^{44}$Ru** | | | | | | | | | | | | | 13 | 0 | 9 | 11 | 11 | 4 | 9 | 0 | 13 | 11 | 4 |
| **$^{45}$Rh** | | | | | | | | | | | | | | 0 | 2 | 2 | 0 | 0 | 2 | 0 | 0 | 16 | 2 |
| **$^{46}$Pd** | | | | | | | | | | | | | | | 0 | 7 | 4 | 0 | 2 | 0 | 9 | 13 | 7 |
| **$^{47}$Ag** | | | | | | | | | | | | | | | | 7 | 2 | 0 | 20 | 13 | 16 | 16 | 9 |
| **$^{72}$Hf** | | | | | | | | | | | | | | | | | 0 | 0 | 0 | 0 | 9 | 20 | 0 |
| **$^{73}$Ta** | | | | | | | | | | | | | | | | | | 2 | 27 | 11 | 22 | 16 | 0 |
| **$^{74}$W** | | | | | | | | | | | | | | | | | | | 22 | 7 | 16 | 11 | 7 |
| **$^{75}$Re** | | | | | | | | | | | | | | | | | | | | 2 | 18 | 13 | 0 |
| **$^{76}$Os** | | | | | | | | | | | | | | | | | | | | | 9 | 11 | 2 |
| **$^{77}$Ir** | | | | | | | | | | | | | | | | | | | | | | 13 | 0 |
| **$^{78}$Pt** | | | | | | | | | | | | | | | | | | | | | | | 0 |

## 5.6 Changing Composition

A system containing 2.5% of a single alloy element is prepared by running metropolis and thermal equilibration routines. A second element is then slowly added to the first until 2.5% of the second element is present. On each addition of an new alloy atom the metropolis algorithm is allowed to re-equilibrate the system for a sufficient amount of time. The rate of adding atoms is ensured to be low enough by re-running at half the rate and showing results to be consistent. This model could be thought of as a model for a secondary alloy slowly diffusing into a region and changing its composition. The simulations were performed thermostated to 600 K at 0 GPa.

The self correlation of the original element and the added element is calculated for each composition, as well as the cross-correlation. The correlation results from the second half of each metropolis run are averaged over, to give better statistics at each composition. Five iron based tertiary alloys were considered, with alloying elements: Os-Cu, Re-Cu, Ru-Cu, Ta-Mn, and Os-Re. The systems were picked for their strong cross-interactions. The results are discussed below.

### 5.6.1 Strukturbericht Classifications

The following analysis refers to two strukturbericht lattices: B1 and B2 (shown in fig. 5.20). Both structures are binary mixtures of an equal ratio of two species of atom. B1 is equivalent to fcc with a secondary element place on each side and centrally. B2 is equivalent to bcc with the central atom replaced by a different species.

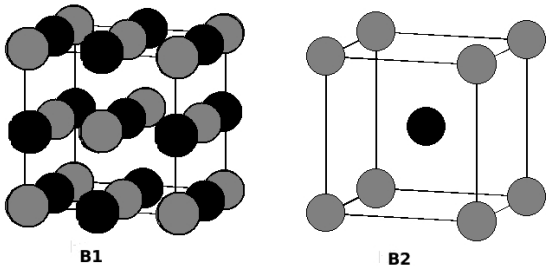


*Figure 5.20*: *Diagram of strukturbericht lattices B1 and B2.*

### 5.6.2 Results

Os was slowly added to a sample already containing Cu. The changes to the correlations of the elements is shown in fig. 5.21. Cu clusters are gradually destroyed by the addition of Os. A single precipitate of Cu and Os with B2 structure is eventually formed.

The results for Re being added to a system already containing 2.5% Cu are shown in fig. 5.22. The Cu clusters 1st n.n. correlation is reduced as Re is slowly absorbed by the clusters. Eventually forming a single precipitate of Cu and Re with B2 structure. The results are similar to those for Os-Cu.

The results for Ru being added to a system already containing 2.5% Cu are shown in fig. 5.23. The Cu remains tightly clustered, with no mixing of the Ru. The Ru is attracted to the surface of the cluster, but does not entirely plate it due to its self-repulsion. 60% of the Ru is on the surface of the Cu cluster, while the rest is unclustered in the lattice.

The results for Ta being added to a system containing 2.5% Mn are shown at 1 n.n. in fig. 5.24 and 2 n.n. in fig. 5.25. The Mn clusters slowly absorbs the Ta creating a B1 lattice at 2 n.n. distance (first neighbours to the alloy being iron). The deconstruction of the initial Mn clusters is rapid and almost complete with only 1% Ta added to the system.

The results for Os being added to a system containing 2.5% Re are shown in fig. 5.26. Initially the Re is spread through the sample with no clustering. As Os is added neither element shows self or cross-correlations. After about 0.9% Os is added the system exhibits a sudden transition to a mixed cluster of Re and Os. The cluster contains small plates of each element and is compact.

It can be seen that introducing secondary elements into the system can strongly affect the clustering properties of the original system in various manners.

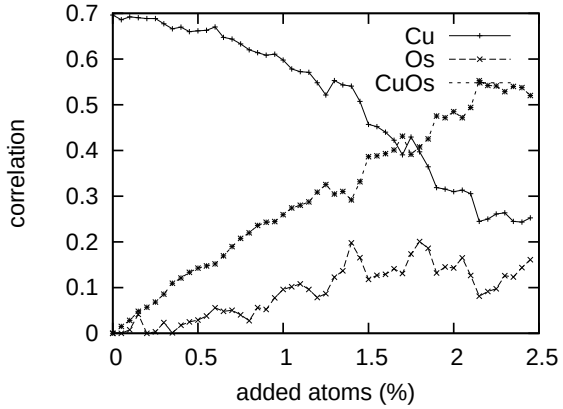


*Figure 5.21*: *Shows first nearest neighbour correlation for a sample of iron containing 2.5% Cu while Os is slowly added. Maximum correlation is denoted as 1 on this scale. The copper clusters 1st n.n. correlation is reduced as Os is slowly absorbed by the clusters, eventually forming a single precipitate of Cu and Os with B2 structure.*

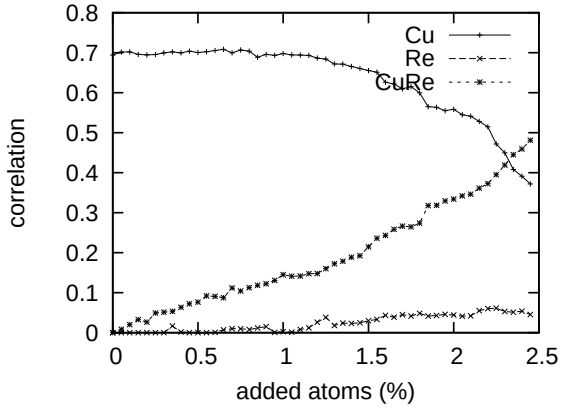


*Figure 5.22*: *Shows first nearest neighbour correlation for a sample of iron containing 2.5% Cu while Re is slowly added. Maximum correlation is denoted as 1 on this scale. The copper clusters 1st n.n. correlation is reduced as Re is slowly absorbed by the clusters, eventually forming a single precipitate of Cu and Re with B2 structure.*

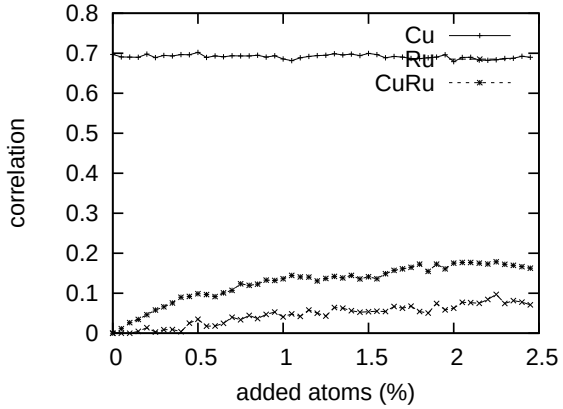


*Figure 5.23*: *Shows first nearest neighbour correlation for a sample of iron containing 2.5% Cu while Ru is slowly added. The copper remains tightly clustered, with Ru being attracted to the clusters surface. Maximum correlation is denoted as 1 on this scale.*

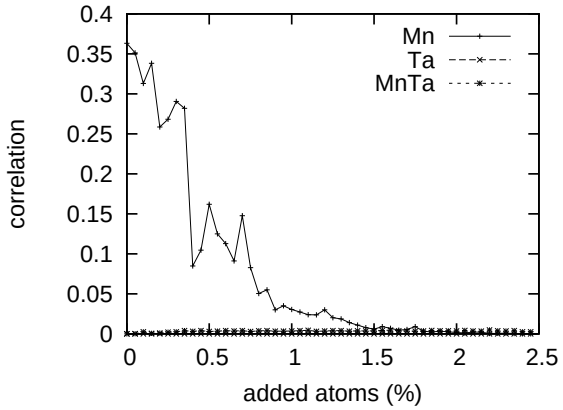


*Figure 5.24*: *Shows first nearest neighbour correlation for a sample of iron containing 2.5% Mn while Ta is slowly added. Maximum correlation is denoted as 1 on this scale.*

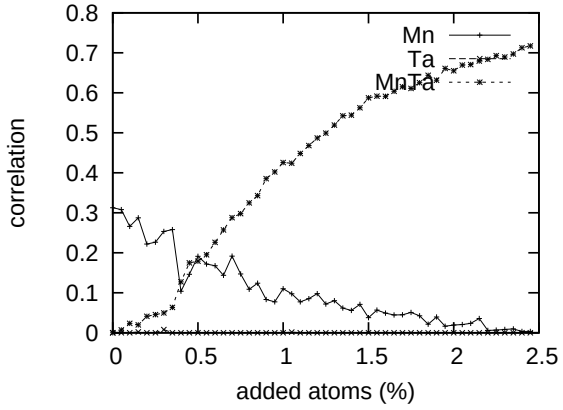


*Figure 5.25*: *Shows second nearest neighbour correlation for a sample of iron containing 2.5% Mn while Ta is slowly added. Maximum correlation is denoted as 1 on this scale. The second neighbour self correlation is destroyed, while the second nearest neighbour cross-correlation increases. This is indicative of a second nearest neighbour cubic lattice forming, with alternating element types (2 n.n. B1 lattice in the strukturbericht classification).*

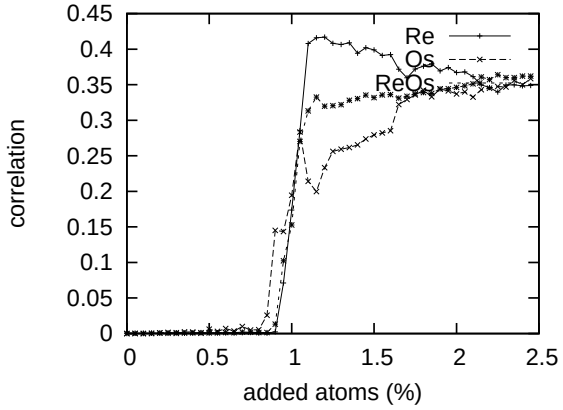


*Figure 5.26*: *Shows first nearest neighbour correlation for a sample of iron containing 2.5% Re while Os is slowly added. Maximum correlation is denoted as 1 on this scale. Initially the Re is spread through the sample with no clustering. After about 0.9% Os is added the system exhibits mixed clusters of Re and Os.*

## 5.7 Radiation Induced Precipitation

### 5.7.1 Introduction

Often alloys exist in out-of-equilibrium configurations achieved by rapid quenching of the molten alloy. For a phase transition to occur it must be energetically favourable as well as having sufficient kinetic energy in the system to make the change probable. Rapid quenching limits the time in which both conditions are met, making the transition unlikely. Alloys that would otherwise exist as precipitates in the metallic lattice can be forced into a mixed state, with varying properties by careful manufacturing techniques[89, 90]. This current study looks at how radiation cascades affects out-of-equilibrium alloys and if cascades can directly cause radiation-induced segregation(RIS) or if this effect is only due to the subsequent diffusion of defects.

Radiation induced segregation is linked to the coupling of defect fluxes to specific alloying elements, inducing changes in local elemental concentrations[12]. This effect was first observed as solute segregation to voids in electron irradiated samples[10] and has more recently been studied by atomic probe tomography (APT) techniques[11]. Segregation can enrich or deplete certain elements at grain boundaries[91], dislocation[92], and voids[10] under both electron and neutron irradiation. These effects are explained by the defect fluxes in the system having preferential attraction to a certain alloy component[12]. Fluxes of vacancies and voids will occur around absorbing sinks such as grain boundaries etc. Coupling of these fluxes to specific elements gives the behaviours observed. TEM study of electron irradiated samples reveal that precipitate can also form without correlation to sinks for point defects[93]. As the precipitating element must be self-attractive, small clusters act as sinks for further precipitation.

This present study looks at additional effects of preferential motion of defect atoms during the cascade phase, to study any segregation effects that are not directly due to diffusion.

### 5.7.2 Method

The effects of repeated radiation cascades on a 2-component alloy are studied. 5% of an alloying element is placed randomly into the $\alpha$-iron lattice consisting of $30^3$ unit cells of 54 000 atoms. The system was then thermally equilibrated to 500 K using constant pressure boundary conditions. After equilibration 10 keV cascades were introduced into the system consecutively. Constant volume boundary conditions were used for the bombardment phase as cascades cause large fluctuations in pressure. The system was thermostated back to 500 K after each cascade had dissipated. Cascades were introduced by picking an atom in the system at random and giving it additional velocity equivalent to 10 keV of kinetic energy in a random direction. For efficiency the spatially varying time-step model is used to simulate the cascades (see sec. 2.3).

The number of Frenkel pairs is calculated after each cascade has dissipated. These are measured with the technique described in sec. 3.4. The clustering is tracked by measuring the correlation of alloying elemental at $1^{st}$, $2^{nd}$ and $3^{rd}$ nearest neighbour distance, as described in sec. 5.3.4.

### 5.7.3 Results

The three group 11 transition metals, Cu, Ag, and Au, were studied due to their tendency to self-cluster. All three elements exhibit nucleation of small clusters during repeated bombardment. Graphs of this tendency are shown: Cu (fig. 5.27), Ag (fig. 5.28), Au (fig. 5.29). Cu nucleates dimers at 1 n.n., Ag at $1^{st}$ and $2^{nd}$ n.n. and Au at 2 n.n.

This clustering occurs on the pico-second scale, and is not a long term diffusion effect, but rather due to rearrangements in the melt region of the cascade. These results show that precipitation of alloying elements to small cluster nucleation sites can be aided by bombardment melt regions. The clusters do not become large over the times studied, but could act as nucleation points for further cluster growth. The increase in 1 n.n. correlation per cascade for Cu and Ag is 0.07% and 0.05% respectively. The Au sample shows enhancement at 2 n.n. at a rate of 0.06% per cascade.

The cumulative damage is also studied in these simulations, as shown in fig. 5.30. The damage formation rate per cascade, falls off as point-defect density increases. This is due to faster re-combination rates, especially in the cascade melt region. Fluctuations are large, and the overall effect of the later cascades can be to create or annihilate up to ∼20 new defect pairs (fig. 5.31). The fraction of interstitials that are of the alloying element is tracked. There is a depletion of alloy interstitials from the 5% that may be expected. Cu has 4.7% alloying interstitials, with 1.0% for Ag and 1.4% for Au. This is likely a size effect, with the smaller particles being more likely to be repelled to interstitial sites during the recrystallization of the melt region.

Os was also studied as it is a self-clustering element in iron. However it did not achieve any significant correlation, due to the barriers to nucleation of this element (discussed in sec. 5.4.3). Additionally 3 samples that undergo concentration induced phase transitions to self-clustering behaviour were studied; Rh, Re, and Ta. The 5% alloy concentration is below the transition threshold for all 3 alloys. They were studied to see if disruption in the crystal, such as strain from point defects, may provide an alternative root to self clustering under bombardment. Of the three samples studied there was no significant clustering.

### 5.7.4 Conclusions: Radiation Induced Precipitation

Three out-of-equilibrium alloys that have a preference for precipitation at equilibrium were studied. The alloying element increases its self-correlation under bombardment. These enriched regions could act as initial sites for further precipitate growth. Alloys that only prefer equilibrium precipitation behaviour at higher concentrations were also studied. They were not observed to strongly change in correlation.

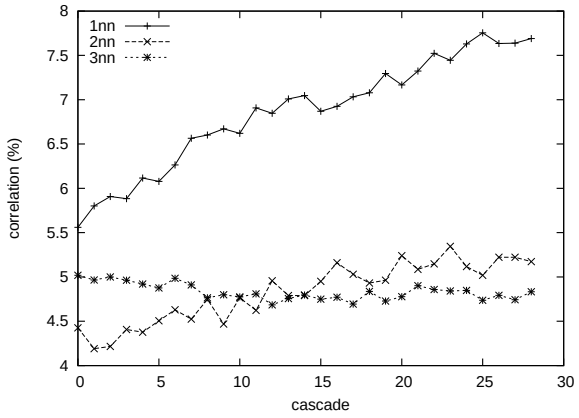


*Figure 5.27*: *Graph of* $1^{st}$, $2^{nd}$ *and* $3^{rd}$ *nearest neighbour self correlation for 5% Cu in iron under repeated 10 keV bombardment at 500 K. Values above or below 5% represent enhanced and depleted interactions respectively. A tendency towards forming small 1 n.n. clusters is observed under heavy bombardment.*

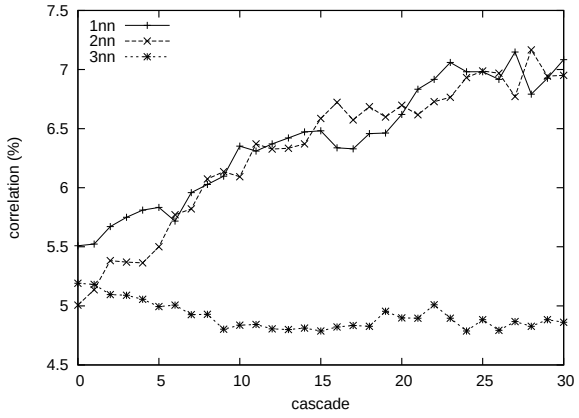


*Figure 5.28*: *Graph of* $1^{st}$, $2^{nd}$ *and* $3^{rd}$ *nearest neighbour self correlation for 5% Ag in iron under repeated 10 keV bombardment at 500 K. Values above or below 5% represent enhanced and depleted interactions respectively. The sample shows clusters form with both* $1^{st}$ *and* $2^{nd}$ *n.n. interaction under heavy bombardment.*

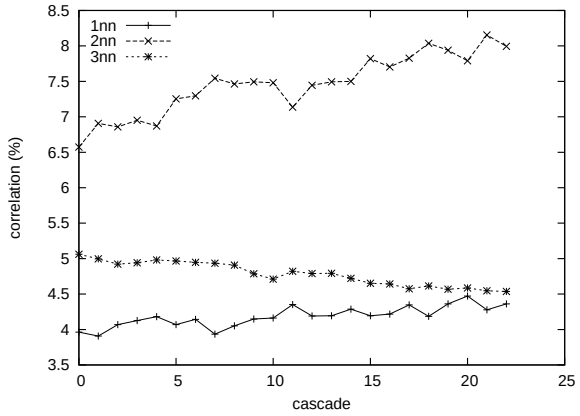


*Figure 5.29*: *Graph of* $1^{st}$, $2^{nd}$ *and* $3^{rd}$ *nearest neighbour self correlation for 5% Au in iron under repeated 10 keV bombardment at 500 K Values above or below 5% represent enhanced and depleted interactions respectively. A tendency towards forming small 2 n.n. clusters is observed under heavy bombardment.*

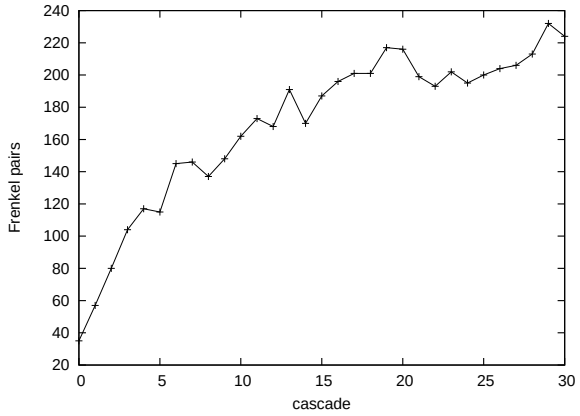


*Figure 5.30*: *Graph of the number of Frenkel pairs in the system against number of cascades. The system tends to an equilibrium number of defects as high densities of free interstitials and vacancies lead to higher recombination rates, especially in the melt region of cascades. This graph is for 5% Ag although is typical of the Frenkel pair trends in the Cu and Au studies.*

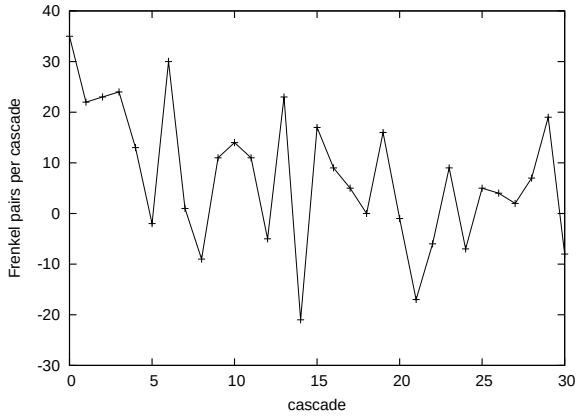


*Figure 5.31*: *Graph of the number of Frenkel pairs per cascade in the system against number of cascades. This graph is for 5% Ag although is typical of the Frenkel pair trends in the Cu and Au studies.*

## 5.8 Conclusions

The properties of binary and tertiary alloys have been explored. The alloy clustering, as temperature and concentration are varied, is explored for the binary alloys. Both concentration and temperature driven transitions between clustered and disordered phases are identified. The attraction of alloying elements to a void was also explored, showing that all alloying elements preferred vicinity to the void. Attraction at 1 n.n. or 2 n.n. to the void is preferred based mainly on size mismatch of the element in the lattice: reduction of lattice strain by being close to the void is balanced against the loss of bonding energy.

Clustering in tertiary alloys was measured. The behaviour was shown to centre around the 6 strongly clustering elements and their interactions. Mixing two elements that prefer disordered state in the binary alloy, never produced a non-disordered tertiary alloy. Mixing an alloy that prefers to be disordered in the binary system with one that prefers to be clustered, can yield complex behaviour: either destroying the clusters present or being absorbed into them.

The competition of the elements to sit close to the void is studied in tertiary alloys. The results can be analysed simply in terms of vacancy binding energies, with other interactions being of secondary consideration. When two elements that prefer 1 n.n. sites to the void are present, the one with strongest vacancy binding energy tends to bind preferentially to the void. The second element

typically shows a decrease in 1 n.n. void attraction and is forced to 2 n.n distance. Elements that prefer 1 n.n. sites will typically remain there, repelling elements that prefer 2 n.n.

Several studies were performed of the changes to precipitates in iron, due to the introduction of a third element. The introduction is done slowly so as to study the nature of the the transitions. The absorption of the third element into the clusters was a common trend. Also observed was the plating of the cluster by the new element. In one case a non-precipitating binary alloy is induced to precipitate to mixed clusters by the introduction of a third element. The transitions were fairly gradual apart from in the case of inducing clustering, which had a sharp concentration based onset.

Out-of-equilibrium alloys that have a preference for precipitation at equilibrium were studied. The alloying element increases its self-correlation under bombardment. This mechanism could be related to the initial nucleation of precipitates.

Due to the complexities of modelling transition metals, a simple rescaling method is unlikely to capture all the intricacies of the alloys behaviour. To quantify how well the potentials act it would be necessary to compare to experiment or to DFT. DFT typically has far less assumptions and so greatly improved accuracy over empirical-rescaled potentials. Although DFT is too computationally expensive to perform large scale studies with, small samples could be compared for effects such as atomic volume and defect stabilities as predicted in the mixed alloys by both methods. Future work on this would be beneficial to quantifying which features the rescaled method is most likely to reproduce correctly. Such data would be of use in refining and improving the re-scaling approach.

# Chapter 6

# Conclusion

A variant on the Verlet algorithm was developed in chapter 2, which allows two different time steps to be used simultaneously during a simulation. The development of more efficient algorithms such as this, is essential to allowing larger simulations to be performed, or more data to be gained quickly. This type of algorithm is of use for cascade simulations, where the kinetic energy is not evenly distributed in the simulation cell. The algorithm is demonstrated to accelerate cascades by around a factor of 3 or more, depending on the exact system set-up.

In chapter 3, the surface bombardment of copper with argon ions was studied. As well as providing insight into the mechanisms involved in the damage formation, the study also helps to validate the MD and KMC techniques used, by directly comparing the results to experimental data. This is important in ensuring the reliability of the assumptions made in the simulation models. Combining KMC and MD approaches allows both the damage formation and subsequent diffusion of defects to be studied. The distribution and yield of clusters compares favourably to experiment.

When a cascade overlaps the surface it strongly interacts, forming craters and adatom clusters. The interaction appears more directed than may be obtained from a local melt region model. Replacement-collisions chains orient preferentially towards the surface to alleviate the compression at the bottom of the crater, while taking advantage of the depletion region above this for easier motion.

In chapter 4 the interaction of cascades with voids and bubbles has been studied, also using a multi-scale approach of MD and OKMC models. The MD simulations reveals a ballistic motion of voids when overlapped by the cascade. The presence of helium in the void is shown to suppress this mechanism by resisting the insertion of matter.

The void movement mechanism was implemented in an OKMC code to compare to diffusive rates in the system. The main mechanism compared to was the motion of voids due to absorption and emission of point defects or defect clusters. The ballistic motion of the void due to interaction with the cascade is shown to be greater than the other diffusive mechanism across most parameters (for cascade energies greater than 2.5 keV).

In chapter 5, a Metropolis method is used to explore the properties of binary and tertiary alloys. Exploration of a potential set that gives transition metal like behaviour, can be of use in understanding the possible mechanisms that can occur on the nano-scale in complex alloys. The alloy clustering, as temperature and concentration are varied, is explored for the binary alloys. The general trends of clustering and void interaction are detailed for binary and tertiary alloys, focusing on precipitation and void surface coating behaviours.

Several studies were performed of the changes to precipitates in iron, due to the gradual introduction of a third element. The exact dynamic pathways are not followed, instead using metropolis techniques. These simulations give information on the tendencies of various alloys to undergo precipitation changes as the local concentrations are changed by various effects.

Out-of-equilibrium alloys that have a preference for precipitation at equilibrium were studied under radiation bombardment using MD. The alloying element increases its self-correlation under bombardment, possibly forming nucleation sites for further precipitation. There seems to be a tendency of the alloy to try to approach its equilibrium state under bombardment.

## 6.1 Future Work

Radiation damage is triggered by cascade phenomena which are on the nanometre and femto-second scale. However, the properties of the material are required on macroscopic scales and over time frames of years. Bridging this gap requires the use of several different simulation methods, each on different length and time-scales. Approximating between scales requires careful assumptions that will not lose important data. Of interest would be the development of more coupled models of radiation damage, perhaps allowing automatic coarsening of the system in uninteresting areas. Equally of interest would be methods to approximate coarsened objects as atomic entities for when objects approach within interaction range of each other.

Further development of hybrid MD-continuum models would be one approach to this. Regions far from strong interactions are modelled as elastic displacement waves instead of individual atoms. This technique has already been used to implement boundary conditions for simulations, although the interface was not dynamic[94, 95]. Development of a model with dynamic shifting of the atomic regime to only capture the necessary regions would be of use in increasing simulation efficiency.

# Bibliography


[1] G. Odette and G. Lucas, "Recent progress in understanding reactor pressure vessel steel embrittlement," *Radiation Effects and Defects in Solids*, vol. 144, pp. 189–231, 1997.

[2] E. A. Little, "Void-swelling in irons and ferritic steels .1. mechanisms of swelling suppression," *Journal of Nuclear Materials*, vol. 87, no. 1, pp. 11–24, 1979.

[3] L. Mansur, "Mechanisms and kinetics of radiation effects in metals and alloys.," *Kinetics of Nonhomogenous Processes*, p. pp. 377463., 1987.

[4] M. Gilbert, S. Dudarev, D. Nguyen-Manh, S. Zheng, L. Packer, and J. Sublet, "Neutron-induced dpa, transmutations, gas production, and helium embrittlement of fusion materials," *Journal of Nuclear Materials*, vol. 442, pp. S755–S760, 2013.

[5] G. R. Odette, M. J. Alinger, and B. D. Wirth, *Recent developments in irradiation-resistant steels*, vol. 38 of *Annual Review of Materials Research*, pp. 471–503. Palo Alto: Annual Reviews, 2008.

[6] M. R. Gilbert, S. L. Dudarev, S. Zheng, L. W. Packer, and S. J.-Ch., "An integrated model for materials in a fusion power plant: transmutation, gas production, and helium embrittlement under neutron irradiation," *Nucl. Fusion*, vol. 52, pp. 1–12, 2012.

[7] P. D. Edmondson, C. M. Parish, Y. Zhang, A. Hallen, and M. K. Miller, "Helium bubble distributions in a nanostructured ferritic alloy," *Journal of Nuclear Materials*, vol. 434, no. 1-3, pp. 210–216, 2013.

[8] Y. N. Osetsky and D. J. Bacon, "Atomic-level interaction of an edge dislocation with localized obstacles in fcc and bcc metals," *Iutam Symposium on Mesoscopic Dynamics of Fracture Process and Materials Strength*, vol. 115, pp. 193–202, 2004.

[9] R. Schaublin and N. Balue, "Radiation damage in ferritic/martensitic steels for fusion reactors: a simulation point of view," *Nuclear Fusion*, vol. 47, no. 12, pp. 1690–1695, 2007.

[10] P. R. Okamoto, S. D. Harkness, and J. J. Laidler, "Solute segregation to voids during electron-irradiation," *Transactions of the American Nuclear Society*, vol. 16, no. JUN, pp. 70–70, 1973.

[11] Z. Jiao and G. S. Was, "Atom probe tomography of radiation-induced precipitation in reactor cladding and structural steels," *Microscopy and Microanalysis*, vol. 16, pp. pp 1598–1599, 2010.

[12] G. S. Was, *Fundamentals of Radiation Materials Science, ch. 6.* Springer, 2007.

[13] C. Kohler, P. Kizler, and S. Schmauder, "Atomistic simulation of precipitation hardening in alpha-iron: influence of precipitate shape and chemical composition," *Modelling and Simulation in Materials Science and Engineering*, vol. 13, p. 3545, 2005.

[14] S. L. Dudarev, "Density functional theory models for radiation damage," *Annual Review of Materials Research, Vol 43*, vol. 43, pp. 35–61, 2013.

[15] M. W. Finnis and J. E. Sinclair, "A simple empirical n-body potential for transition-metals," *Philosophical Magazine a-Physics of Condensed Matter Structure Defects and Mechanical Properties*, vol. 50, no. 1, pp. 45–55, 1984.

[16] M. Daw and M. Baskes, "Embedded-atom method: Derivation and application to impurities, surfaces, and other defects in metals," *Physical Review B*, vol. 29, pp. 6443–6453, 1984.

[17] K. Lavrentiev, M Yu andMergia, M. Gjoka, D. Nguyen-Manh, G. Apostolopoulos, and S. L. Dudarev *Journal of Physics-Condensed Matter*, vol. 24, pp. 1–5, 2012.

[18] P. D. Lane, G. E. Isted, and R. J. Cole, "Effect of surface defects and adsorbates on the optical anisotropy of cu(110)," *Physical Review B*, vol. 82, no. 7, p. 8, 2010.

[19] R. S. Averback and P. Bellon, *Fundamental Concepts of Ion-Beam Processing*, vol. 116 of *Topics in Applied Physics*, pp. 1–28. Berlin: Springer-Verlag Berlin, 2010.

[20] T. Michely and C. Teichert, "Adatom yields, sputtering yields, and damage patterns of single-ion impacts on pt(111)," *Physical Review B*, vol. 50, no. 15, pp. 11156–11166, 1994.

[21] I. H. Wilson, Y. J. Chen, and J. B. Xu, "Single ion impacts on an in0.22ga0.78as/gaas(100) surface observed by atomic force microscopy," *Nuclear Instruments & Methods in Physics Research Section B-Beam Interactions with Materials and Atoms*, vol. 124, no. 4, pp. 500–505, 1997.

[22] I. H. Wilson, N. J. Zheng, U. Knipping, and I. S. T. Tsong, "Effects of isolated atomic collision cascades on sio2/si interfaces studied by scanning tunneling microscopy," *Physical Review B*, vol. 38, no. 12, pp. 8444–8449, 1988.

[23] X. P. Zhu, M. K. Lei, Z. H. Dong, S. M. Miao, and T. C. Ma, "Crater formation on the surface of titanium irradiated by a high-intensity pulsed ion beam," *Surface & Coatings Technology*, vol. 173, no. 1, pp. 105–110, 2003.

[24] V. A. Shulov and N. A. Nochovnaya, "Crater formation on the surface of metals and alloys during high power ion beam processing," *Nuclear Instruments & Methods in Physics Research Section B-Beam Interactions with Materials and Atoms*, vol. 148, no. 1-4, pp. 154–158, 1999.

[25] E. M. Bringa, E. Hall, R. E. Johnson, and R. M. Papaleo, "Crater formation by ion bombardment as a function of incident angle," *Nuclear Instruments & Methods in Physics Research Section B-Beam Interactions with Materials and Atoms*, vol. 193, pp. 734–738, 2002.

[26] M. T. E. Ercolessi, F. Parrinello, "Simulation of gold in the glue model," *Phil. Mag. A*, vol. 58, pp. 213–226, 1988.

[27] C. Reimann *Nucl. Instr. and Meth. B*, vol. 95, p. 181, 1994.

[28] R. S. Averback and M. Ghaly, "A model for surface damage in ion-irradiated solids," *Journal of Applied Physics*, vol. 76, no. 6, pp. 3908–3910, 1994.

[29] V. M. Glazov and O. D. Shchelikov, "Volume changes during melting and heating of silicon and germanium melts," *High Temperature*, vol. 38, no. 3, pp. 405–412, 2000.

[30] M. Ghaly, K. Nordlund, and R. S. Averback, "Molecular dynamics investigations of surface damage produced by kiloelectronvolt self-bombardment of solids," *Philosophical Magazine a-Physics of Condensed Matter Structure Defects and Mechanical Properties*, vol. 79, no. 4, pp. 795–820, 1999.

[31] M. Morgenstern, T. Michely, and G. Comsa, "Collective effects in the adatom production by 4.5 kev rare-gas impacts on pt(111): a low-temperature scanning tunnelling microscopy analysis," *Philosophical Magazine a-Physics of Condensed Matter Structure Defects and Mechanical Properties*, vol. 79, no. 4, pp. 775–794, 1999.

[32] G. J. Ackland, G. Tichy, V. Vitek, and M. W. Finnis, "Simple n-body potentials for the noble-metals and nickel," *Philosophical Magazine a-Physics of Condensed Matter Structure Defects and Mechanical Properties*, vol. 56, no. 6, pp. 735–756, 1987.

[33] W. E. Wallace and G. J. Ackland, "Calculated energies and relaxations of the low-index planes of ordered cu3au," *Surface Science*, vol. 275, no. 1-2, pp. L685–L690, 1992.

[34] A. J. E. Foreman, W. J. Phythian, and C. A. English, "The molecular-dynamics simulation of irradiation damage cascades in copper using a many-body potential," *Philosophical Magazine a-Physics of Condensed Matter Structure Defects and Mechanical Properties*, vol. 66, no. 5, pp. 671–695, 1992.

[35] Y. Bandurin, V. A. Esaulov, L. Guillemot, and R. C. Monreal, "Surface miller index dependence of auger neutralization of ions on surfaces," *Physical Review Letters*, vol. 92, no. 1, 2004.

[36] J. P. Biersack and J. F. Ziegler, "Refined universal potentials in atomic-collisions," *Nuclear Instruments & Methods in Physics Research*, vol. 194, no. 1-3, pp. 93–100, 1982.

[37] W. G. Hoover, "Canonical dynamics: Equilibrium phase-space distributions," *Phys. Rev. A*, vol. 31, p. 16951697, 1985.

[38] E. A. Kenik and T. E. Mitchell, "Orientation dependence of the threshold displacement energy in copper and vanadium," *Philosophical Magazine*, vol. Vol. 32 Iss. 4, 1975.

[39] G. Mills, G. Jonsson H. Schenter, "Reversible work transition-state theory - application to dissociative adsorption of hydrogen," *Surface Science*, vol. 324, pp. 305–337, 1995.

[40] D. T. Kulp, G. J. Ackland, M. Sob, V. Vitek, and T. Egami, "Many-body potentials for cu-ti intermetallic alloys and a molecular-dynamics study of vitrification and amorphization," *Modelling and Simulation in Materials Science and Engineering*, vol. 1, no. 3, pp. 315–333, 1993.

[41] D. R. Lide, *CRC Handbook of Chemistry and Physics, 88th edition. (p. 1439).* Taylor & Francis Group, 2008.

[42] G. Carter, "Spike and shock processes in high-energy deposition density atomic collision events in solids," *Radiation Effects and Defects in Solids*, vol. 43, pp. 193–199, 1979.

[43] R. P. Webb and D. E. Harrison, "Evidence for ion-induced hypersonic shock-waves for computer-simulations of argon ion-bombardment of copper," *Applied Physics Letters*, vol. 39, no. 4, pp. 311–312, 1981.

[44] C. C. Fu and F. Willaime, "Ab initio study of helium in alpha-fe: Dissolution, migration, and clustering with vacancies," *Physical Review B*, vol. 72, no. 6, 2005.

[45] D. J. Bacon and Y. N. Osetsky, "Multiscale modelling of radiation damage in metals: from defect generation to material properties," *Materials Science and Engineering a-Structural Materials Properties Microstructure and Processing*, vol. 365, no. 1-2, pp. 46–56, 2004.

[46] N. Soneda, S. Ishino, and T. D. de la Rubia, "Vacancy loop formation by 'cascade collapse' in alpha-fe: a molecular dynamics study of 50 kev cascades," *Philosophical Magazine Letters*, vol. 81, no. 9, pp. 649–659, 2001.

[47] C. C. Fu, J. Dalla Torre, F. Willaime, J. L. Bocquet, and A. Barbu, "Multiscale modelling of defect kinetics in irradiated iron," *Nature Materials*, vol. 4, no. 1, pp. 68–74, 2005.

[48] K. Morishita, B. D. Wirth, T. D. de la Rubia, and A. Kimura, "Effects of helium on radiation damage processes in iron," *Pricm 4: Forth Pacific Rim International Conference on Advanced Materials and Processing, Vols I and Ii*, pp. 1383–1386, 2001.

[49] V. I. Dubinko and N. P. Lazarev, "Effect of the radiation-induced vacancy emission from voids on the void evolution," *Nuclear Instruments & Methods in Physics Research Section B-Beam Interactions with Materials and Atoms*, vol. 228, pp. 187–192, 2005.

[50] J. K. Steele and D. I. Potter, "The disappearance of voids during 180-kev ni+ bombardment of nickel," *Journal of Nuclear Materials*, vol. 218, no. 2, pp. 95–107, 1995.

[51] J. Pu, L. Yang, F. Gao, H. L. Heinisch, R. J. Kurtz, and X. T. Zu, "Interaction of displacement cascade with helium bubbles in alpha-iron: Computer simulation," *Nuclear Instruments & Methods in Physics Research Section B-Beam Interactions with Materials and Atoms*, vol. 266, no. 18, pp. 3993–3999, 2008.

[52] D. C. Parfitt and R. W. Grimes, "Predicted mechanisms for radiation enhanced helium resolution in uranium dioxide," *Journal of Nuclear Materials*, vol. 381, no. 3, pp. 216–222, 2008.

[53] G. Lucas and R. Schaublin, "Helium effects on displacement cascades in alpha-iron," *Journal of Physics-Condensed Matter*, vol. 20, no. 41, p. 12, 2008.

[54] A. F. Calder, D. J. Bacon, A. V. Barashev, and Y. N. Osetsky, "On the origin of large interstitial clusters in displacement cascades," *Philosophical Magazine*, vol. 90, no. 7-8, pp. 863–884, 2010.

[55] W. Jager and H. Trinkaus, "Defect ordering in metals under irradiation," *J. Nucl. Matt.*, vol. bf 205, pp. 394–410, 1993.

[56] H. L. Heinisch and B. N. Singh *Phil. Mag.*, vol. 83, pp. 3661–3676, 2003.

[57] W. Wilson and R. Johnson, "Rare gases in metals interatomic potentials and simulation of lattice defects," *Plenum*, p. 375, 1972.

[58] N. Juslin and K. Nordlund, "Pair potential for fe-he," *Journal of Nuclear Materials*, vol. 382, no. 2-3, pp. 143–146, 2008.

[59] T. Seletskaia, Y. N. Osetsky, R. E. Stoller, and G. M. Stocks, "Calculation of helium defect clustering properties in iron using a multi-scale approach," *Journal of Nuclear Materials*, vol. 351, no. 1-3, pp. 109–118, 2006.

[60] G. J. Ackland, M. I. Mendelev, D. J. Srolovitz, S. Han, and A. V. Barashev, "Development of an interatomic potential for phosphorus impurities in alpha-iron," *Journal of Physics-Condensed Matter*, vol. 16, no. 27, pp. S2629–S2642, 2004.

[61] S. L. Dudarev and P. M. Derlet, "A 'magnetic' interatomic potential for molecular dynamics simulations," *Journal of Physics-Condensed Matter*, vol. 17, no. 44, pp. 7097–7118, 2005.

[62] G. J. Ackland, K. D'Mellow, S. L. Daraszewicz, D. J. Hepburn, M. Uhrin, and K. Stratford, "The moldy short-range molecular dynamics package," *Computer Physics Communications*, vol. 182, no. 12, pp. 2587–2604, 2011.

[63] D. E. Beck *Mol. phys*, vol. 14, p. 311, 1968.

[64] C. Bjorkas, K. Nordlund, and M. J. Caturla, "Influence of the picosecond defect distribution on damage accumulation in irradiated alpha-fe," *Physical Review B*, vol. 85, no. 2, p. 8, 2012.

[65] C. J. Ortiz and M. J. Caturla, "Cascade damage evolution: rate theory versus kinetic monte carlo simulations," *Journal of Computer-Aided Materials Design*, vol. 14, pp. 171–181, 2007.

[66] G. S. Was, *Fundamentals of Radiation Materials Science, ch. 2.2.3.* Springer, 2007.

[67] M. Miller, K. Powers, R. Nanstad, and P. Efsing, "Atom probe tomography characterizations of high nickel, low copper surveillance rpv welds irradiated to high uences," *Journ al of Nucle ar Materials*, vol. 437, pp. 107–115, 2013.

[68] D. J. Hepburn, G. J. Ackland, and P. Olsson, "Rescaled potentials for transition metal solutes in -iron," *Philosophical Magazine*, vol. 89, no. 34-36, pp. 3393–3411, 2009.

[69] C. J. Cramer and D. G. Truhlar, "Density functional theory for transition metals and transition metal chemistry," *Physical Chemistry Chemical Physics*, vol. 11, no. 46, pp. 10757–10816, 2009.

[70] C. Diedrich, A. Luchow, and S. Grimme, "Performance of diffusion monte carlo for the first dissociation energies of transition metal carbonyls," *Journal of Chemical Physics*, vol. 122, no. 2, p. 4, 2005.

[71] S. G. Li and D. A. Dixon, "Benchmark calculations on the electron detachment energies of mo3- and m2o6- (m = cr, mo, w)," *Journal of Physical Chemistry A*, vol. 111, no. 46, pp. 11908–11921, 2007.

[72] E. J. McEniry, G. K. H. Madsen, J. F. Drain, and R. Drautz, "Tight-binding simulation of transition-metal alloys," *Journal of Physics-Condensed Matter*, vol. 23, no. 27, p. 8, 2011.

[73] L. Marville and W. Andreoni, "Size dependence of the structural properties of transitlon-metal aggregates from an empirical interatomic potential scheme," *J. Phys. Chem*, vol. 91, pp. 2645–2649, 1987.

[74] X. Cox, H. Liu and J. Murrell, "Modelling cu, ag and au surfaces using empirical potentials," *Mol. Phys.*, vol. 93, pp. 921–924, 1998.

[75] J. N. Murrell and R. E. Mottram, "Potential-energy functions for atomic solids," *Molec. Phys.*, vol. 62, p. 571, 1990.

[76] R. Roberts, C. Johnston and N. Wilson, "A genetic algorithm for the structural optimization of morse clusters," *Theor Chem Acc*, vol. 104, pp. 123–130, 2000.

[77] V. J. R. Darby, S. Mortimer-Jones and C. Roberts, "Theoretical study of cuau nanoalloy clusters using a genetic algorithm," *JOURNAL OF CHEMICAL PHYSICS*, vol. 116, pp. 1536–1551, 2001.

[78] F. Cleri and V. Rosato, "Tight-binding potentials for transition metals and alloys," *Physical Review B*, vol. 48, 1993.

[79] X. C. D. W. W. Cheng, D. Liu and S. Huang, "Surface segregation of agcuau trimetallic clusters," *Nanotechnology*, vol. 18, pp. 1–6, 2007.

[80] C. Baletto, F. Mottet and R. Ferrando, "Growth simulations of silver shells on copper and palladium nanoclusters," *Physical Review B*, vol. 66, 2002.

[81] F. Ducastelle, "Elastic moduli of transition metals," *J.Phys.*, vol. 31, p. 1055, 1970.

[82] G. Allan and M. Lannoo, "rends in the cohesive properties of sp bonded elements," *Journal de Physique*, vol. 44, pp. 1255–1363, 1983.

[83] F. Ducastel, "Moments developments and their application to electronic charge distribution of d-bands," *Journal of physics and chemistry of solids*, vol. 31, p. 1295, 1970.

[84] G. J. Ackland, D. J. Bacon, A. F. Calder, and T. Harry, "Computer simulation of point defect properties in dilute fe-cu alloy using a many-body interatomic potential," *Philosophical Magazine a-Physics of Condensed Matter Structure Defects and Mechanical Properties*, vol. 75, no. 3, pp. 713–732, 1997.

[85] G. Ackland and V. Vitek, "Many-body potentials anti atomic-scale relaxations in noble-metal alloys," *Physical Review B*, vol. 41, pp. 10324–10333, 1990.

[86] D. J. Deng, H-F. Bacon, "Simulation of point defects and threshold displacements in pure cu and a dilute cu-au alloy," *Physical Review B*, vol. 48, pp. 10022–10030, 1993.

[87] H. Gades and M. Urbassek, "Surface binding energies of alloys: a many-body approach," *Nuclear Instruments and Methods in Physics Research B*, vol. 88, pp. 218–228, 1994.

[88] E. E. Zhurkin and M. Hou, "Structural and thermodynamic properties of elemental and bimetallic nanoclusters: an atomic scale study," *Journal of Physics-Condensed Matter*, vol. 12, no. 30, pp. 6735–6754, 2000.

[89] R. Miernik, K. Bogucki and S. Pytel, "Effect of quenching techniques on the mechanical properties of low carbon structural steel," *Archives of foundry engineering*, vol. 10, pp. 91–96, 2010.

[90] S. P. Belyaev, V. V. Istomin-Kastrovskiy, V. V. Koledov, D. S. Kuchina, P. V. Lega, N. N. Resnina, V. G. Shavrov, and A. V. Shelyakov, "The structure and functional properties of ni-ti-cu alloy rapidly quenched ribbons with different parts of crystalline phase," *ESOMAT*, vol. 02016, pp. 1–5, 2009.

[91] G. S. Was, J. P. Wharry, B. Frisbie, B. D. Wirth, D. Morgan, J. D. Tucker, and T. R. Allen, "Assessment of radiation-induced segregation mechanisms in austenitic and ferritic-martensitic alloys," *Journal of Nuclear Materials*, vol. 411, no. 1-3, pp. 41–50, 2011.

[92] M. Hatakeyama, S. Tamura, and I. Yamagata, "Direct observation of solute-dislocation interaction on screw dislocation in a neutron irradiated modified 316 stainless steel," *Materials Letters*, vol. 122, pp. 301–305, 2014.

[93] R. Cauvin and G. Martin, "Radiation-induced homogeneous precipitation in undersaturated solid-solutions," *Journal of Nuclear Materials*, vol. 83, no. 1, pp. 67–78, 1979.

[94] W. A. Curtin and R. E. Miller, "Atomistic/continuum coupling in computational materials science," *Modelling Simul. Mater. Sci. Eng.*, vol. 11, pp. R33–R68, 2003.

[95] B. d. Celis, A. S. Argon, and S. Yip, "Molecular dynamics simulation of crack tip processes in alpha-iron and copper," *J. Appl. Phys.*, vol. 54, pp. 4864–4878, 1983.

# Publications

G. J. Galloway and G. J. Ackland *"Molecular dynamics and object kinetic Monte Carlo study of radiation-induced motion of voids and He bubbles in bcc iron"* **Phys.Rev.B 87**, 104106 (2013)

P. D. Lane, G. J. Galloway, R. J. Cole, M. Caffio, R. Schaub, and G. J. Ackland *"Validating molecular dynamics with direct imaging of radiation damage debris"* **Phys. Rev. B 85**, 094111 (2012)